UNIVERSIDADE DA BEIRA INTERIOR
Engenharia

Aero-Structural Wing Analysis using a Vortex Lattice Method Coupled with an Equivalent Plate Model

Pedro Daniel da Rocha Santos

Dissertação para obtenção do Grau de Mestre em
Engenharia Aeronáutica
(2º ciclo de estudos)

Orientador: Prof. Doutor Pedro V. Gamboa

Covilhã, Outubro de 2011

Acknowledgments

First and foremost I would like to acknowledge my supervisor, Professor Doutor Pedro Gamboa, for their support and patience and, most of all, for sharing his expertise and knowledge with me.
I would like to thank all my professors and colleagues for their guidance and understanding, since the beginning of my journey.
I would like to thank all my true friends, those who have been with me in the good moments and especially in the difficult moments of my life.
I want to thank my parents, Ermelinda e Agostinho, my brother João and also my grandmother Alexandrina, for their strength and support in this chapter of my life. Without them, none of this would have been possible.
To my love, Patrícia, for her infinite support. Without her, this work would have been much tougher!

Resumo

O presente trabalho descreve a integração de uma ferramenta de análise aerodinâmica baseada no Método da Folha de Vórtices (VLM) e uma ferramenta de análise estrutural baseada no modelo de Placa Equivalente (EPM), culminando numa ferramenta Aero-Estrutural, capaz de analisar asas. As ferramentas de análise aerodinâmica e estrutural são descritas e validadas, utilizando dados experimentais e numéricos. O modelo aerodinâmico é ampliado, de modo a permitir o cálculo das características não-lineares da asa. Esta ferramenta de análise mostrou boa concordância com dados experimentais, tanto em análises lineares como não-linear. A ferramenta estrutural revelou boa concordância com análises em elementos finitos, tanto no caso de deformação com aplicação de carga estática, como numa análise modal. Após descrever e validar as duas disciplinas, o acoplamento entre estas é descrito. Uma asa rectangular, composta por uma casca, longarinas e nervuras, é analisada recorrendo à ferramenta Aero-Estrutural desenvolvida. Para além desta análise, uma validação experimental do programa foi levada a cabo. Para atingir este fim, uma asa rectangular feita em alumínio e espuma de PVC é construída e testada em túnel de vento. Com vista a medir as deformações impostas pelo carregamento aerodinâmico da asa, um sistema de medição totalmente automatizado foi desenvolvido, usando um sensor de medição laser e guias lineares accionadas por motores de passo. Os resultados mostraram uma boa concordância entre a deformação calculada com o modelo numérico e os dados recolhidos a partir de testes de túnel de vento. Algumas fontes de erros experimentais são identificadas e alguns melhoramentos são propostos.

Palavras-chave

Teoria da Folha de Vórtices, Teoria da Placa Equivalente, Análise Aero-Estrutural

Abstract

The present work describes the integration of a non-linear Vortex Lattice Method (VLM) aerodynamic solver and an Equivalent Plate Model (EPM) structural solver, culminating in an Aero-Structural tool capable of analyzing wings. The aerodynamic and structural tools used in the Aero-Structural solver are described and validated, using experimental and numerical data. The aerodynamic model is expanded with the decambering approach, in order to allow for non-linear wing characteristics to be computed. This solver showed good agreement with experimental data both in linear and in non-linear regimes. The structural solver revealed good agreement with Finite-Element calculations, in both static load deformation and modal analysis. After describing and validating the two disciplines, the coupling between aerodynamic and structural solvers is described. A rectangular wing composed of skins, spars and ribs is analyzed using the present Aero-Structural solver. An experimental validation of the program developed is carried out. To accomplish this, a rectangular wing made with aluminum and PVC foam is built and tested in a wind tunnel. To measure wing deformations under aerodynamic loading, an in-house fully automated measurement system was developed using a laser measuring sensor and linear-guides actuated by stepper motors. The results showed a general good agreement between the deformation calculated with the numerical model and the data collected from wind tunnel testing. Some sources of experimental errors are identified and some enhancements are proposed.

Keywords

Vortex Lattice Method (VLM), Equivalent Plate Theory (EPM), Aero-Structural Analysis

Contents

Acknowledgments iii

Resumo v

Abstract vii

Contents x

List of Figures xiii

List of Tables xiii

Nomenclature xv

1 Introduction 1

1.1 Aero-Structural Design . . . 1
1.2 Aerodynamic Analysis . . . 2
1.3 Structural Analysis . . . 4
1.4 Objectives . . . 4
1.5 Thesis Outline . . . 5

2 Aerodynamics Solver 7

2.1 Vortex-Lattice Method . . . 7
2.1.1 Linear Theory Formulation . . . 7
2.1.2 Modeling of Reflections from Solid Boundaries . . . 10
2.1.3 Non-Linear Theory Formulation . . . 10
2.2 Parasite Drag Calculation . . . 14
2.3 Compressibility Correction . . . 14
2.4 Computational Improvements . . . 15
2.5 Validation . . . 15
2.5.1 Test Case 1 - Naik and Ostowari Experimental Validation . . . 16
2.5.2 Test Case 2 - Sivells Experimental Validation . . . 18
2.5.3 Test Case 3 - Wing/Tail Configuration . . . 21
2.5.4 Summary . . . 22

3 Structural Solver 23

3.1 Equivalent Plate Theory and Implementation . . . 23
3.1.1 Mathematical Formulation . . . 23
3.2 Computational Improvements . . . 25
3.3 Validation . . . 26
3.3.1 Modal Analysis . . . 26
3.3.2 Static Load Analysis . . . 28
3.3.3 Summary . . . 29

4 Aero-structural Solver **31**
4.1 Aero-structural Model Implementation . . . 31
4.1.1 Mathematical Formulation . . . 32
4.1.2 Aero-structural Iterative Procedure . . . 33
4.2 Aeroelasticity . . . 33
4.2.1 Flutter . . . 33
4.2.2 Flutter Speed Prediction Implementation . . . 34
4.3 The Aero-Structural Program Implementation . . . 35
4.4 The Aero-Structural Graphical User Interface (GUI) . . . 35
4.5 Numerical Study . . . 38
4.5.1 Wing Structural and Geometric Considerations . . . 38
4.5.2 Solid Wall Correction . . . 39
4.5.3 Wing Numerical Results . . . 40

5 Experimental Study **43**
5.1 The Wind Tunnel . . . 43
5.2 The Measurement Installation . . . 44
5.2.1 Stepper Motor Control System . . . 44
5.2.2 The Linear Guides . . . 46
5.2.3 The Laser Measuring Sensor . . . 46
5.2.4 Double Window System . . . 48
5.2.5 Complete Assembly . . . 48
5.2.6 The CNC and Sensor Acquisition software . . . 49
5.3 The Test Wing . . . 50
5.3.1 Wing Construction . . . 50
5.3.2 Wing Installation Inside the Wind Tunnel . . . 50
5.4 Sensor Support Influence on Velocity Distribution . . . 52
5.5 Solid and Wake Blockage Evaluation . . . 53
5.6 Experimental Test Results . . . 54

6 Comparison Between Numerical and Experimental Results **57**
6.1 Comments on Experimental Errors . . . 58

7 Conclusions **61**
7.1 Future Work . . . 61
7.1.1 Numerical . . . 62
7.1.2 Experimental . . . 62

Bibliography **65**

A The Vortex Ring **67**
A.1 Velocity Induced by a Straight Vortex Segment . . . 67
A.2 The Vortex Ring element . . . 69

B Leuze ODSL8 Optical laser distance sensor specifications **71**

C Paper Accepted for ICEUBI2011 **73**

List of Figures

1.1 Diagram representing sequential optimization of aerodynamics and structures. . 2

2.1 The vortex ring element. 7
2.2 Vortex ring model for a thin lifting surface. 8
2.3 Definition of wing outward normal. 10
2.4 Modeling of ground effect by using the image technique. 10
2.5 Flowchart of the iterative decambering approach for a wing. 13
2.6 Planform of the rectangular wings used in Naik and Ostowari Experimental Validation (only right wing portion shown). 17
2.7 Wing $C_L - \alpha$ predicted using VLM3D for a rectangular wing of aspect ratio 12, using a NACA 4409 airfoil at Reynolds number of 0.25 million. 17
2.8 Wing $C_L - \alpha$ predicted using VLM3D for a rectangular wing of aspect ratio 9, using a NACA 4409 airfoil at Reynolds number of 0.25 million. 18
2.9 Planform of the trapezoidal wing (only right wing portion shown). 19
2.10 Wing $C_L - \alpha$ and $C_D - C_L$ predicted using VLM3D for a trapezoidal wing without washout, using a NACA 65-210 airfoil at Reynolds number of 4.4 million. 20
2.11 Wing $C_L - \alpha$ and $C_D - C_L$ predicted using VLM3D for a trapezoidal wing with 2° washout, using a NACA 65-210 airfoil at Reynolds number of 4.4 million. 20
2.12 Planform of the wing-tail configuration (only right portion shown). 21
2.13 Figure showing: a) hypothetical airfoil lift curve and b) individual contributions of the wing and tail to the total lift of the wing-tail configuration. 22

3.1 Domain transformation used in Kapania and Liu formulation. 24
3.2 Tip and root airfoils used in the tested wing. 27
3.3 CAD model of the trapezoidal wing used in the equivalent plate validation tests. Note that the skins are transparent, revealing the spars and ribs inside the wing. 28
3.4 Displacement of the test wing, due to a torque application. 29

4.1 Aerodynamic and structural solvers coupling methodology. 31
4.2 Figure showing the classical flutter phenomenon. 34
4.3 Screenshot showing the console redirection tab. The normal operation text during an aero-structural analysis is shown. 36
4.4 Screenshot showing the graphics tab. Note that in the aerodynamic XY graph the C_l distribution is selected and that in the main graph, the w deformation is selected. 37
4.5 Screenshot showing GUI options dialog and the OpenGL 3D viewer. 37
4.6 Airfoil used for the tip and root wing stations of the tested wing. 39
4.7 CAD model of the wing used in the aero-structural numerical tests. Note that skin is transparent, revealing the spars and ribs inside the wing. 39
4.8 CAD model showing the wing confined by two solid walls. Each wall is separated 0.4m from the wing. 40
4.9 Displacements of the test wing, due to aerodynamic loading at $\alpha = 0°$, V = 20.26m/s: a) u, b) v, c) w deflection distribution and d) spanwise u, v and w deflection distribution at 50% chord line. 41

4.10 Displacements of the test wing, due to aerodynamic loading at $\alpha = 4°$, V = 20.15m/s: a) u, b) v, c) w deflection distribution and d) spanwise u, v and w deflection distribution at 50% chord line. 41
4.11 Displacements of the test wing, due to aerodynamic loading at $\alpha = 6°$, V = 20.10m/s: a) u, b) v, c) w deflection distribution and d) spanwise u, v and w deflection distribution at 50% chord line. 42

5.1 Photograph showing the EReME wind tunnel. 44
5.2 Photograph showing the electronic components needed to control the stepper motors: 1) 36V and 5V power sources switches, 2) 36V power source, 3) 5V power source, 4) longitudinal and 5) vertical direction stepper motor drives and 6) CNC motion controller. 45
5.3 Photographs illustrating stepper motors used and the connection to the linear guide. 45
5.4 Photography showing the linear moving guides mounted in "T" configuration and the metal frame used to support the system. 46
5.5 Leuze ODSL8 optical distance measuring sensor used in the experimental validation. 47
5.6 Sensor mast with and without the streamlined cowl. 47
5.7 Photograph showing the complete test assembly. 48
5.8 Screenshot showing the CNC controller software. At the center, the path used to acquire the deformations along the wing and at the right the respective G-code, is observed. 49
5.9 Screenshot showing the sensor acquisition software. On the left the graph view is observed and on the right the notebook view. 50
5.10 Photograph of the actual wing used in the experimental test. 51
5.11 Photograph showing the wing in place for wind tunnel testing. 51
5.12 Wind tunnel velocity profile comparing the different situations studied: clean section, sensor support without cowl and sensor support with cowl. Note that sensor support is in position Z=0.31m. 52
5.13 Displacement of the test wing, due to aerodynamic loading at $\alpha = 0°$: a) w deflection distribution across the wing and b) spanwise w deflection distribution at half chord line. 54
5.14 Displacement of the test wing, due to aerodynamic loading at $\alpha = 4°$: a) w deflection distribution across the wing and b) spanwise w deflection distribution at half chord line. 54
5.15 Displacement of the test wing, due to aerodynamic loading at $\alpha = 6°$: a) w deflection distribution across the wing and b) spanwise w deflection distribution at half chord line. 55

6.1 Spanwise w deflection distribution at half chord length for the experimental and numerical tests: a) $0°$, b) $4°$ and c) $6°$. 58

A.1 Velocity induced by a straight vortex segment. 67
A.2 Definition of the view angles used for the vortex-induced velocity calculation. . . 68
A.3 Nomeclature used for the velocity induced by a tree-dimensional straight vortex segment. 68
A.4 The vortex ring element. 69

List of Tables

3.1 Geometric and material properties of the test wing 26
3.2 Structural components position and dimensions used in the test wing. 27
3.3 Comparison of natural vibration frequencies computed with EPM and FEM. 28

4.1 Geometric and material properties of the rectangular wing used in aero-structural analysis. 38
4.2 Structural components position and dimensions used in the aero-structural test wing. 38
4.3 Environment and wind tunnel conditions for 0°, 4° and 6° test cases. 40

5.1 Summary of wind-tunnel blockage elements and its respective correction. 54

B.1 Laser sensor specifications. 71

Nomenclature

α	angle of attack
c	wing/airfoil chord
C_d	airfoil drag coefficient
C_l	airfoil lift coefficient
C_m	airfoil pitching moment coefficient about the quarter chord
$C_{l,max}$	maximum airfoil lift coefficient
α_{0l}	angle of attack corresponding to airfoil zero lift
$dC_l/d\alpha$ or C_{l_α}	airfoil lift curve slope
C_D	wing drag coefficient
C_L	wing lift coefficient
C_M	wing pitching moment coefficient
$C_{L,max}$	maximum wing lift coefficient
α_{0L}	angle of attack corresponding to wing zero lift
$dC_L/d\alpha$ or C_{L_α}	wing lift curve slope
F	residual vector
f	element of residual vector
J	Jacobian matrix
m	total number of vortex rings
N	number of wing sections
n_a	total number of aerodynamic nodes
$U_\infty, V_\infty, W_\infty$	velocity components of the free-stream flow
u_a, v_a, w_a	induced velocity of the vortex ring in x, y and z direction
x_2	chordwise starts location of the second decambering function
M_∞	freestream Mach number
Q_∞	freestream flow vector
$\delta_1(x)$	first decambering function
$\delta_2(x)$	second decambering function
δ_x	vector containing the corrections to the Newton variables
Γ	strength of bound vortex

Φ velocity potential

n normal vector

$\theta_2(x)$ angular coordinate corresponding to x_2

D under-relaxation factor used in Newton iteration

ε_{sb} solid blockage correction

ε_{wb} wake blockage correction

u, v, w wing deflections in x, y and z axis

V_f wing flutter speed

Acronyms

API Application programming interface

CFD Computational Fluid Dynamics

CNC computer numerical control

DLL dynamic-link-libraries

EPM Equivalent Plate Model

FEM Finite Element Model

FSDT First order shear deformation theory

GUI Graphical User Interface

LLT Lifting Line Theory

MIMD multiple instruction, multiple data

NTP Normal Temperature and Pressure

OpenMP Open Multi-Processing

RAM Random-access memory

SIMD Single instruction, multiple data

VLM Vortex Lattice Method

Subscripts

i, j index of wing section

max maximum

sec represents value for a wing section

visc represents value from two-dimensional viscous experimental or computational data

Patience and perseverance have a magical effect before which difficulties disappear and obstacles vanish into air.

John Quincy Adams - American 6th US President (1825-29)

Chapter 1

Introduction

Universidade da Beira Interior started developing UAV's almost ten years ago. In this type of vehicle, as in a commercial or military airplane, optimization is crucial in order to utilize the available resources in the best possible way. To allow aerodynamic and structural optimization, aerodynamic and structural solvers that provide rapid, but yet accurate calculations are essential. In fact, to investigate various configurations in a cost effective way, the time needed for each calculation should be reduced. Thus, good solvers should always result from a compromise between accuracy and computational requirements.
In this way, the lack of an aero-structural tool capable of analyzing wings during preliminary design phases, that offers quick yet precise results, stimulated the development of the proposed work. The strong need to apply in UAV design is evidenced by the experimental validation that will be carried out. The experimental validation aims to evaluate the accuracy of the proposed aero-structural program, searching for a good correlation between the numerical model and the reality.

1.1 Aero-Structural Design

Aero-structural design is an active development topic that presents several challenges. In this design approach, aerodynamic and structural disciplines are coupled, being possible to determine wing deformation under the aerodynamic loads. Traditionally, aero-structural design has been performed in a cut-and-try basis: aerodynamicists have an idea of the shape of an "optimal" load distribution and then tailor the jig shape of the structure so that the deflected wing shape under a 1-g load gives the desired load distribution [1]. This approach may be adequate up to a certain level for conventional transport aircraft, where considerable accumulated experience exists. In the case of either new planform concepts or new flight regimes, however, the lack of experience combined with the complexities of aero-structural interactions can lead to designs that are far from optimal.
In the worst case, an ill-informed designer might try to perform sequential optimization of the participating disciplines. This sequential approach is illustrated in Fig.1.1 for the case of aerodynamics and structures. Since the aerodynamic optimization is not aware of the effect that its design variables have on the structural weight, it always tries to yield an elliptic lift distribution to minimize drag. On the other hand, structural optimization finds the minimum structural weight for fixed aerodynamic variables. This sequential optimization process usually converges, but the final result is not the true optimum of the coupled system.
Since two distinct design disciplines are used, they should be carefully selected taking into account the desired application. Two issues in the transfer of information between disciplines are of utmost importance to the success of an automatic design technique [2]. The first one is related with the level of fidelity in the coupling of both disciplines. In fact, this has to be carefully considered in order to guarantee that the accuracy of the individual disciplines is not

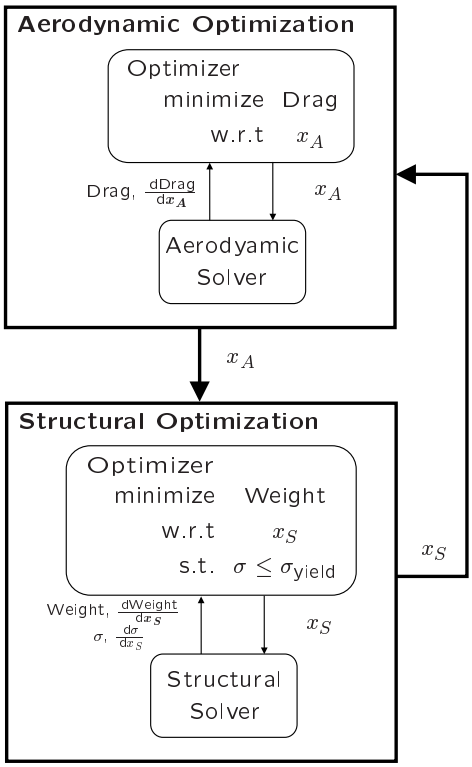

Figure 1.1: Diagram representing sequential optimization of aerodynamics and structures [1].

jeopardized. In the second place, the evolving disciplinary designs must have exact geometric agreement by the end of the design process.

1.2 Aerodynamic Analysis

With the remarkable success of Prandtl's lifting-line theory (LLT) in being able to predict the flow past medium to high aspect ratio unswept wings in incompressible flow, LLT became a standard tool for computing wing aerodynamics, when low fidelity is desired. LLT uses a single unswept lifting line (or bound vortex) to model the circulation on the wing. The strength of this bound vortex, Γ, varies along the span. At any given spanwise location, the change in Γ is shed as trailing vorticity which, in turn, causes induced velocities along the lifting line. LLT enables the computation of the Γ distribution for which the accompanying induced velocities and the resulting effective angles of attack along the span are consistent with the Γ distribution. For this purpose, the classical Prandtl LLT assumes a linear lift-curve slope for the airfoil sections that form the wing. This lift-curve slope is typically close to 2π per radian. With the success of LLT in the prediction of wing flows at low angles of attack, the attention soon turned to whether LLT could be modified for the analysis of wings where nonlinear lift-curve slopes for the airfoil sections can be taken into consideration. To achieve this, basically two categories emerged: the iterative Γ distribution and the α correction.

The first author to successfully use the first technique was Tani [3] in 1934. In his technique, a spanwise bound vorticity (Γ) distribution is first assumed. This distribution is used to compute

the distribution of induced velocities and hence induced angles of attack and effective angles of attack along the lifting line. The distribution of the effective angles of attack is then used to look up the operating C_l of the local section using the known nonlinear $C_l - \alpha$ data for the airfoil. A new Γ distribution is then computed from the spanwise C_l distribution. The iteration is carried out till the Γ distribution converges. Extension of the approach to post-stall angles of attack have been investigated in several subsequent research efforts. Based on a suggestion by von Kármán, Schairer [4] and Sears [5] investigated the possibility of non-unique solutions for post-stall angles of attack. According to Sears [5], von Kármán noticed that Prandtl's lifting-line equation has non unique solutions for cases when the lift-curve slope becomes negative (i.e. when the α increases past the onset of stall). These non-unique solutions include both symmetric and antisymmetric lift distributions even when both the geometry and onset flow are symmetric. Sears mentions that von Kármán further postulated that even in the conditions just past the onset of wing stall, when some sections of the wing may have positive lift-curve slopes (pre-stall condition) and other sections may have negative lift-curve slopes (post-stall condition), non unique and asymmetric lift distributions are possible. It occurred to von Kármán and Sears that the appearance of large and sometimes violent rolling moments past stall on symmetric wind-tunnel models at zero yaw may be explained by the possibility of asymmetric lift distributions at perfectly symmetric flight conditions.

The second approach is entirely different. This method was developed by Tseng and Lan [6]. While their main focus was on vortex-dominated flows on low aspect ratio fighter-type wings at high α, the effect of boundary-layer separation was incorporated by iteratively reducing the angle of attack at each section of the wing. The reduction at any given wing section is determined by the difference between the potential flow solution and the viscous C_l from the nonlinear section $C_l - \alpha$ curve.

Although, LLT was well developed and applied to various situations, some limitations are found with this method. In fact, LLT does not allow accurate calculation for wings with sweep, low aspect ratio or high dihedral. Thus, more recently, an iterative decambering scheme formulated by Mukherjee and Gopalarathnam [7, 8] was developed to be incorporated in a Vortex-Lattice Method (VLM). In this, the chordwise camber distribution at each section of the wing is reduced to account for the viscous effects at high angles of attack. This approach differs from the previous approaches in its capability to use both the C_l and the C_m data for the section and in the use of a two-variable function for the decambering. In addition, unlike all of the earlier methods, the current approach uses a multidimensional Newton iteration that accounts for the cross-coupling effects between the sections in predicting the decambering for each step in the iteration.

Despite being possible to predict stall and post-stall characteristics of wings using experimental or computational section data for these high angles of attack, it is recognized that the flow over a wing at post-stall conditions is highly three dimensional and that considerable error can result in using this approach. However, such a prediction method is necessary for rapid prediction capabilities in the early design phases of aircraft development. Furthermore, even high-fidelity computational fluid dynamics (CFD) techniques are only now approaching the stage where they can be reliably used for high-alpha aerodynamic prediction. However, these techniques do not yet provide the required flexibility and computational speed for the analysis of a general non-planar wing configuration. In addition, the complexities of the volume grid generation hinder the ability to analyze general non-planar configurations [9]. Thus, low fidelity aerodynamic models, such as the LLT and VLM continue to be of interest. In fact, these methods need low

computational cost, yet provide enough accuracy for the initial stages of wing design. Since it is of interest to have a low computational cost, a Vortex Lattice Method (VLM) is chosen to perform the aerodynamic calculation in the present work.

1.3 Structural Analysis

In structural analysis, finite element analysis (FEA) is broadly used because of its generality, versatility and reliability. The finite element method discretizes the structure into one or more types of basic structural components - the finite elements. This type of analysis is also the method of choice when local discontinuities (holes, abrupt dimension variations,...) exist and detailed results in the vicinity of this discontinuities are needed. However, to accurately analyze this discontinuities, a mesh refinement should be performed near the zone of interest. However, a wide application of detailed FEA at the late conceptual design stage or in the early preliminary design stage still faces some important obstacles. In the first place, a FEA model demands a preparation time that may be prohibitive, especially when the designs analyzed are significantly different. In second place, for complex structures a detailed FEA needs huge amount of CPU time and computation capacity, which effectively increase the cost.
In view of this situation, Equivalent Plate Models (EPM) arise as a compromise to simulate complex structures for the purpose of obtaining solutions in the early design stages. This idea is reasonable as long as the complex structure behaves physically in a close manner to the continuum model used and only global quantities of the response are of concern [10].
In the area of analyzing aerospace wing structures, a number of studies have been conducted on using equivalent beam models to represent simple box wings composed of laminated or anisotropic materials,[11, 12] and they have yielded accurate results for the special problems studied. But from a realistic point of view, using an equivalent plate to model a wing structure is more promising because a wing, especially the one that has a low aspect ratio, is likely to behave more as a plate than as a beam.
Given the nature of aero-structural tool that is being developed, the EPM is the natural choice, since the low computational resources is a requisite. The current EPM is mainly based on the work performed by Kapania and Liu [10], in which the author applied a first order shear deformation theory (FSDT) equivalent plate wing modeling method for the static and dynamic analysis of general wing structures. This method follows the Reissner-Mindlin theory and has as trial functions Ritz-method-based with Legendre polynomials.

1.4 Objectives

The main objective of the current work is to develop and validate an Aero-Structural capable tool. To achieve this primary goal, various tasks should be performed. The main tasks are:

- Development and validation of the aerodynamic program, using the Vortex Lattice Method (VLM);
- Development and validation of the structural program, using the Equivalent Plate Model (EPM);
- Integration of both aerodynamic and structural disciplines, to achieve an Aero-structural capable tool;

- Development of a fully automated measurement system to be coupled to the wind tunnel test section;
- Experimental validation of the developed tool, through wind tunnel testing.

All the referred tasks are necessary and indispensable to achieve the primary objective of this work. In particular, the forth task plays an important roll in the wind tunnel testing, since without the means to acquire wing displacements, the experimental validation is impossible to be carried out.

1.5 Thesis Outline

This thesis is divided into seven main chapters. In Chapter 2, the aerodynamic solver is presented. In the current work, the aerodynamic solver is based on Vortex Lattice Method (VLM). The aerodynamics discipline is expanded with the decambering approach, in order to allow for non-linear wing characteristics to be computed. The resulting program, named VLM3D is then validated against cases found in the literature (and other VLM codes).
Chapter 3 provides a detailed insight into the development of the structural solver. The module employs a structural analysis program based on the Equivalent Plate Model (EPM) theory. This analysis program allows the determination of both static deformation under the aerodynamic loads (computed in the aerodynamics module) and computation of the eigen modes of the wing structure. The analysis program presented is validated against a finite element model (FEM).
The objective of Chapter 4 is to describe the aero-structural implementation. An overview of the computational implementation details and the capabilities added by the graphical User Interface (GUI), as well as its improvements in the user experience are also explained. To conclude this chapter, numerical results are presented for the deformation under aerodynamic loads for a general wing composed of skin, spars and ribs. Additionally, semi-empirical expressions that allow the determination of aeroelastic instabilities are introduced.
In Chapter 5, the wing developed for the numerical study is built and tested in the wind tunnel, to measure the deformation imposed by the aerodynamic loads. To achieve this goal, a whole new measurement installation is developed and implemented, using linear guides actuated with stepper motors and also a laser measuring sensor.
In Chapter 6, the numerical and experimental results are confronted, effectively evaluating the accuracy of the numerical results against the experimental results. A comment about the different error sources is made, in order to find and identify possible correction schemes and enhancements to the overall experimental installation.
Finally, in Chapter 7, conclusions are drawn from the results presented and the satisfactory fulfillment of the objectives is discussed. Additionally, some suggestions are hinted on how to improve the aero-structural tool developed, as a basis for future work. Some suggestions are also made about possible ways to enhance the experimental installation and to reduce the sources of errors.

Chapter 2

Aerodynamics Solver

This chapter provides detailed information on the aerodynamic model used for this thesis. The focus is on the linear aerodynamic model description and also in the non-linear capability introduced by the decambering approach. Additionally, validation tests are performed to investigate the correctness and the limitations of the current implementation.

2.1 Vortex-Lattice Method

The aerodynamic model is important to properly evaluate the performance of a particular design configuration. The model must allow the calculation of wing lift, drag and moment coefficients in a computational efficient way, in order to allow the analysis of different configurations in a short period of time.
In the current work, a FORTRAN code was developed for analysis of multiple lifting surface configurations using a steady Vortex Lattice Method (VLM). The implemented decambering approach extends the original linear formulation and allows non-linear characteristics of the wing to be computed.

2.1.1 Linear Theory Formulation

The derivation of the theory behind the vortex lattice method presented here mainly follows [13]. In the formulation presented in [13], vortex rings are used to discretize the three-dimensional thin lifting surface. Also, the zero-normal-flow boundary condition is satisfied on the actual lifting surface which may have camber and different planform shapes.

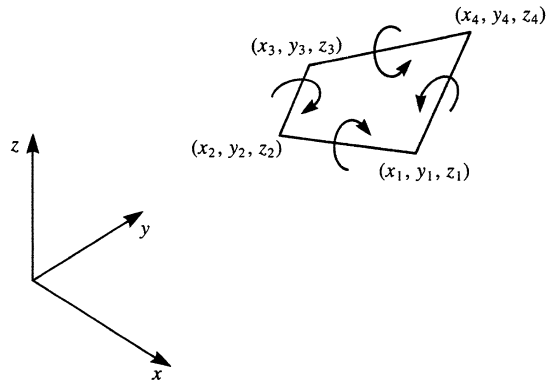

Figure 2.1: The vortex ring element [13].

As said before, the constitutive elements of the thin surface are the vortex rings, (see Fig.2.1), which are fundamentally composed of four straight vortex segments. A complete derivation of the mathematics of the vortex ring element is present in appendix A. The main reason to

use these elements over the horseshoe vortex, is essentially related to the low computational requirements of this element. From the derivation in appendix A, the total induced velocity of the vortex ring at an arbitrary control point can be calculated, noting that the total induced velocity is the sum of the contribution of the four vortex segments. So,

$$(u_a, v_a, w_a) = (u_{1a}, v_{1a}, w_{1a}) + (u_{2a}, v_{2a}, w_{2a}) + (u_{3a}, v_{3a}, w_{3a}) + (u_{4a}, v_{4a}, w_{4a}) \quad (2.1)$$

The method by which the thin wing planform is divided into panels is shown in Fig.2.2. The lifting surface is divided into several spanwise and chord-wise lattices, and in each panel a vortex ring is placed, building the vortex lattice. The leading segment of the vortex ring is placed on the panel's quarter chord line and the collocation point is at the center of the three-quarter chord line. The panel normal vector is also defined at this point. A positive Γ is defined according to the right-hand rotation rule. Since, no unsteady analysis is done, the wake behind the wing is not discretized. In order to satisfy the Kutta condition at the trailing edge the wake is replaced by a series of horse-shoe vortices. The zero-normal-flow boundary condition is satisfied at the control point of each lattice.

One of the major differences between the VLM and panel methods is that in the former the singularities are placed on the mean surface of the wing, rather than on the actual surface. This distribution of vorticity seeks to emulate the changes in velocity induced on the flow as it traverses the upper and lower surfaces of a wing.

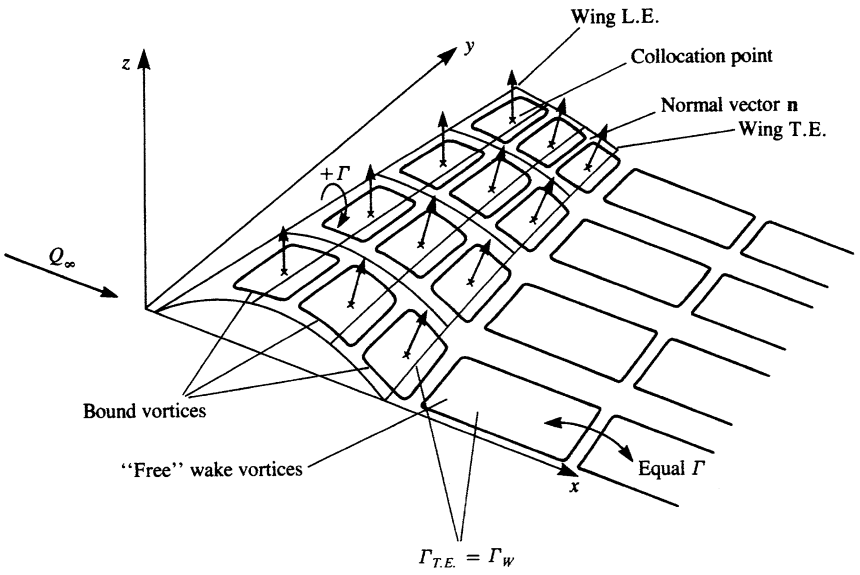

Figure 2.2: Vortex ring model for a thin lifting surface [13].

Regarding the boundary condition for solving Laplace's equation, it is possible to conclude that only the zero normal flow across the wing surface (impermeability condition) has to be applied. Hence:

$$\nabla (\phi + \phi_\infty) \cdot \mathbf{n} = 0 \quad (2.2)$$

In order to evaluate the surface normal, a very simple and efficient method is used as shown in Fig.2.3. The opposite corner points of the panel define two vectors, $\mathbf{A}_k$ and $\mathbf{B}_k$, and their

vector product is the surface normal. Hence:

$$\mathbf{n}_k = \frac{\mathbf{A}_k \times \mathbf{B}_k}{|\mathbf{A}_k \times \mathbf{B}_k|} \quad (2.3)$$

This method is used in the current implementation, since no analytical description of the wing mean surface is available. This method is precise when sufficient chordwise panels are used.

The influence coefficients can now be readily calculated, computing the dot product of the induced velocity of a particular vortex ring and the lattice normal vector. The induced velocity calculated is due to unit strength vortex. Because symmetry is invoked (the distribution of circulation, Γ, is symmetric), the system only has N equations rather than $2N$. Assuming that collocation point number 1 is being treated, the total velocity induced by the first vortex ring and its image is found to be:

$$(u, v, w)_{11} = (u_i, v_i, w_i)_{11} + (u_{ii}, -v_{ii}, w_{ii})_{11} \quad (2.4)$$

where i denotes the vortex ring and ii its image from the left semispan.

Then, the influence coefficient is:

$$a_{11} = (u, v, w)_{11} \cdot \mathbf{n}_1 \quad (2.5)$$

This process is repeated until all the collocation points have been computed.

In order to form the right-hand-side (RHS) of the linear system of equations, the normal velocity components of the free-stream flow should be computed. Hence:

$$RHS = -Q_\infty \cdot \mathbf{n}_i = -(U_\infty, V_\infty, W_\infty) \cdot \mathbf{n}_i \quad (2.6)$$

Once the computation of the influence coefficients and right-hand-side vector is done, the zero normal flow boundary condition (denoted by Eq.(2.2)) will result in the following system of linear equations:

$$\begin{pmatrix} a_{11} & a_{12} & \cdots & a_{1m} \\ \vdots & & \ddots & \vdots \\ a_{m1} & a_{m2} & \cdots & a_{mm} \end{pmatrix} \begin{pmatrix} \Gamma_1 \\ \vdots \\ \Gamma_m \end{pmatrix} = \begin{pmatrix} RHS_1 \\ \vdots \\ RHS_m \end{pmatrix} \quad (2.7)$$

where m denotes the total number of vortex rings.

The solution of Eq.(2.7) yields the value of the vortex strength for each panel. Thus, to compute the lift acting on each panel, the Kutta-Joukowski theorem is applied to each vortice-lattice panel. So,

$$\Delta L = \rho Q_\infty \Delta\Gamma \Delta y \quad (2.8)$$

Similarly, the induced drag calculation is:

$$\Delta D_i = -\rho w_{ind} \Delta\Gamma \Delta y \quad (2.9)$$

The lift and drag distribution is integrated to obtain total lift and drag.

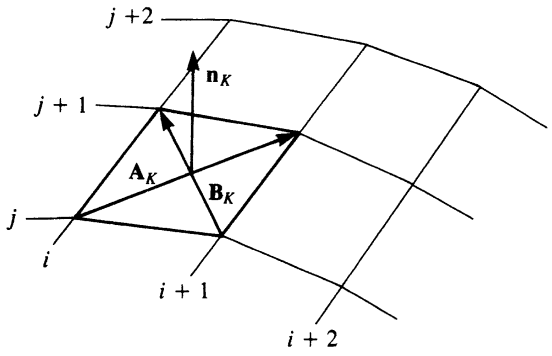

Figure 2.3: Definition of wing outward normal [13].

2.1.2 Modeling of Reflections from Solid Boundaries

In situations when ground proximity or wall proximity is modeled, a simple method can be used to include these features in a numerical scheme.
The inclusion of wall proximity can be achieved by modeling a mirror image of the wing under the $x - y$ plane. So, the velocity at a point P induced by the elements on the real wing and of the imaginary wing are added up. From a numerical point of view, the influence coefficients calculation is modified to include this mirrored image. Figure 2.4 shows graphically the described procedure. Note that the wing is raised in the xyz coordinate system and the ground plane is assumed to be at the $z = 0$ plane.

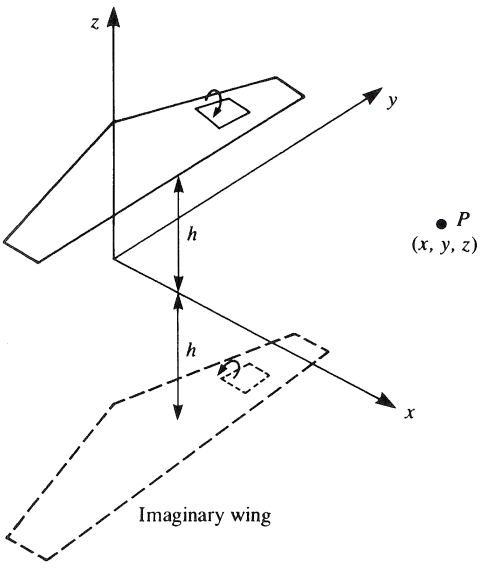

Figure 2.4: Modeling of ground effect by using the image technique [13].

This technique can be extended to model also solid boundaries above the wing. In this case, a mirror image of the wing above the $x - y$ plane of the wing is added.

2.1.3 Non-Linear Theory Formulation

The following section is based on the decambering approach from references [7, 8].

As explained earlier, the lifting surface is divided into several spanwise and chord-wise lattices. Each spanwise section j (composed of a row of chord-wise lattices) has two variables, $\delta_{1,j}$ and $\delta_{2,j}$, for defining the local decambered geometry at that section. Unlike in the two-dimensional case, where the δ_1 and δ_2 are selected to match the differences between the potential-flow and the viscous-flow results, in the three-dimensional case, changing a δ on one section is likely to have a significant effect on the neighboring sections and on the sections of the downstream lifting surfaces. To account for these effects, a $2N-$dimensional Newton iteration is used to predict δ_1 and δ_2 at each of the N sections of all the wings so that ΔC_l and ΔC_m at these sections approach zero as the iteration progresses. A $2N \times 2N$ matrix equation as shown in Eq.(2.10) has to be solved for each step of the Newton iteration [14]. In this equation, F is a $2N-$dimensional vector containing the residuals of the functions f_i to be zeroed, δ_x is the $2N-$dimensional vector containing the corrections required for the $2N$ variables x_i to bring the vector F closer to zero, and J is the $2N \times 2N$ Jacobian of the system containing the gradient information.

$$J.\delta x = -F \quad \textbf{(2.10)}$$

The Jacobian is partitioned into four sub-matrices as shown in Eq.(2.11). Equations (2.12) to (2.15) show the elements of the four sub-matrices.

$$J = \begin{pmatrix} J_{l1} & J_{m1} \\ J_{l2} & J_{m2} \end{pmatrix} \quad \textbf{(2.11)}$$

$$(J_{l1})_{i,j} = \frac{\partial \Delta C_{li}}{\partial \delta_{1,j}} = \frac{(C_{lp})_i - (C_{ls})_i}{[(\delta_{1s})_j + p] - (\delta_{1s})_j} \quad \textbf{(2.12)}$$

$$(J_{m1})_{i,j} = \frac{\partial \Delta C_{mi}}{\partial \delta_{1,j}} = \frac{(C_{mp})_i - (C_{ms})_i}{[(\delta_{1s})_j + p] - (\delta_{1s})_j} \quad \textbf{(2.13)}$$

$$(J_{l2})_{i,j} = \frac{\partial \Delta C_{li}}{\partial \delta_{1,j}} = \frac{(C_{lp})_i - (C_{ls})_i}{[(\delta_{2s})_j + p] - (\delta_{2s})_j} \quad \textbf{(2.14)}$$

$$(J_{m2})_{i,j} = \frac{\partial \Delta C_{mi}}{\partial \delta_{1,j}} = \frac{(C_{mp})_i - (C_{ms})_i}{[(\delta_{2s})_j + p] - (\delta_{2s})_j} \quad \textbf{(2.15)}$$

For each step of the iteration, F and J are determined, and δ_x is computed using Eq.(2.10). The corrections are then applied to the values of δ_1 and δ_2 for all the sections in an effort to bring the residuals closer to zero.

2.1.3.1 The Iterative Procedure to Compute Lift and Pitching Moment Coefficients

The iteration scheme can be summarized using the flowchart in Fig.2.5, and the following procedure:

1. Assume starting values of the decambering defined by δ_1 and δ_2 for each section of the

wing;

2. Compute the wing aerodynamic characteristics using VLM3D. For this computation, the unit normal vector of each lattice is rotated to account for the decambered shape of each section of the wing; the VLM3D analysis provides C_l and C_m at each section as output. These are the starting values for the current step of the iteration and are denoted by $(C_{ls})_j$ and $(C_{ms})_j$ for section j;

3. Compute the starting values of the local effective angles of attack of each section corresponding to the section C_l of that section, using Eq.(2.16). The referred equation assumes a section lift-curve slope of 2π per radian and accounts for the zero-lift angle of attack of the decambered section, which depends on the values of δ_1 and δ_2 and the α_{0l} (airfoil zero lift angle) of the original airfoil camberline.

$$\alpha_{eff} = \frac{(Cl)_{sec}}{2\pi} - \delta_1 - \delta_2 \left(1 - \frac{\theta_2}{2\pi} + \frac{\sin\theta_2}{2\pi}\right) + \alpha_{0l} \quad \textbf{(2.16)}$$

4. Compute the target C_l of each section; for example, the target C_l of section j is given by $(C_{lt})_j$, which is the C_l on the airfoil lift curve corresponding to $(\alpha_s)_j$. Similarly, $(C_{mt})_j$, the target C_m, is the C_m on the airfoil $C_m - \alpha$ curve corresponding to $(\alpha_s)_j$. Hence, the residuals are $(\Delta C_l)_j = (C_{ls})_j - (C_{lt})_j$ and $(\Delta C_m)_j = (C_{ms})_j - (C_{mt})_j$;

5. Perturb δ_1 at section j by adding a small perturbation p;

6. Compute the wing aerodynamic characteristics with the perturbed decambering using VLM3D. Then, compute the j^{th} column of J_{l1} and J_{m1} using Eqs.(2.12) and (2.13);

7. Reset the value of δ_1 at section j to $(\delta_{1s})_j$;

8. Cycle through steps 5 - 6 for all values of the section index j to compute all the columns of J_{l1} and J_{m1};

9. Repeat steps 5 - 8 now perturbing δ_2 instead of δ_1 to compute J_{l2} and J_{m2};

10. Using the Newton equation in Eq.(2.10), compute the correction vector δ_x. Update the values of δ_1 sand δ_2 by adding the correction vector δ_x multiplied by a user-specified damping factor D (also referred to under-relaxation factor). In the current work, D has been set to 0.01.

This iteration process is carried out until all the residuals have converged to a specified tolerance. In the current work the user can define the tolerance value, which should lie in the interval 0.01 to 0.001.

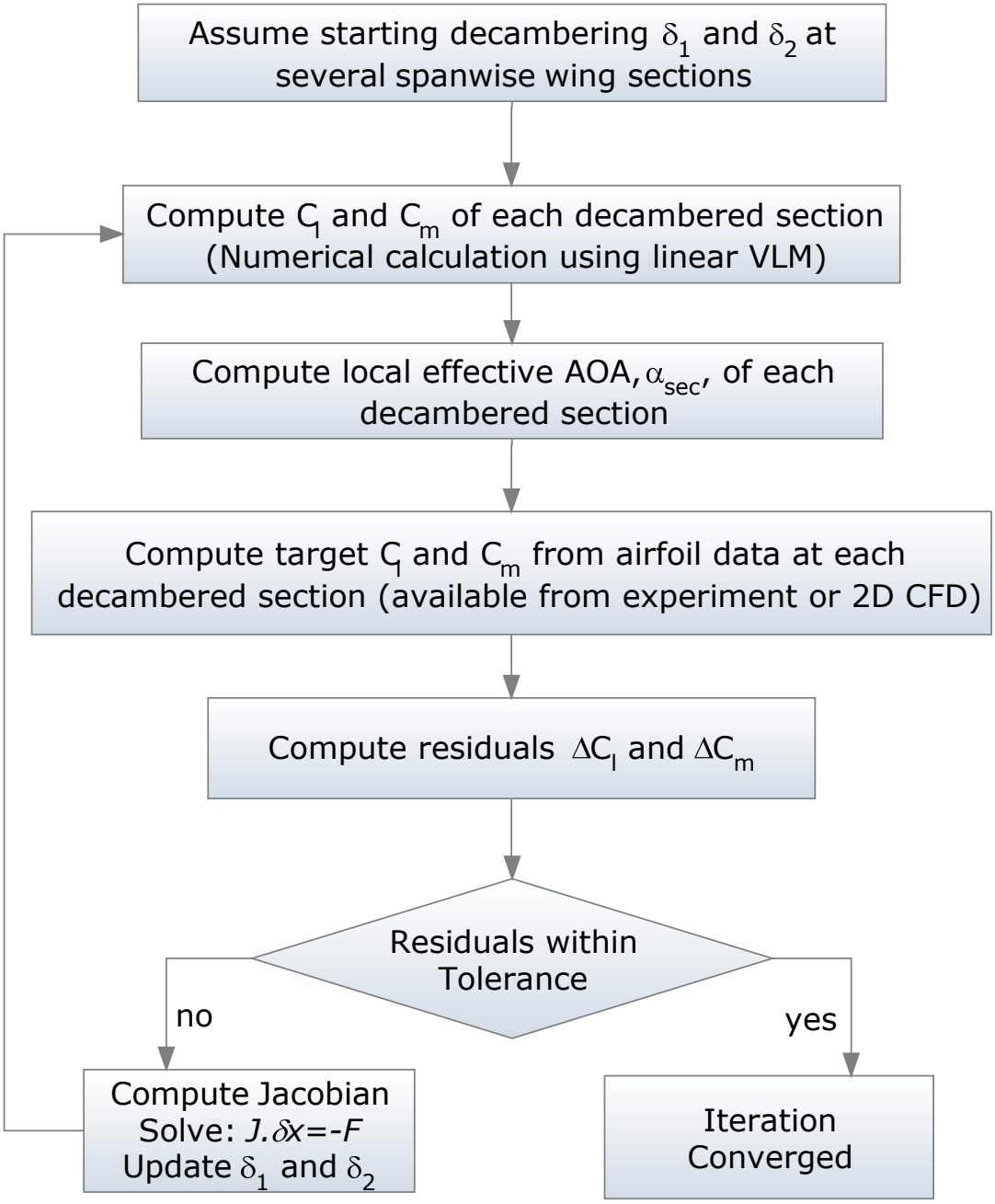

Figure 2.5: Flowchart of the iterative decambering approach for a wing.

2.2 Parasite Drag Calculation

Given the assumptions of the VLM code, only the induced drag can be directly calculated. To overcome this limitation, the known section drag coefficient can be used to compute the parasite drag. Given the definition of effective angle of attack:

$$\alpha_{eff}(y) = \alpha - \alpha_i(y) \quad (2.17)$$

and noting that the parasite drag is calculated by the following integral equation:

$$C_{D0} = \frac{1}{S}\int_{-\frac{b}{2}}^{\frac{b}{2}} C_d(y)c(y)dy \quad (2.18)$$

where $C_d(y)$ is calculated for the effective angle of attack given by Eq.(2.17), obtained from known airfoil data, and $c(y)$ is the local chord length. Then, the total drag coefficient is obtained by adding the induced drag to Eq.(2.18). The integral in Eq.(2.18) is computed using Simpson's rule. This approximation yields good results until three-dimensional flow separation becomes predominant.

2.3 Compressibility Correction

In the VLM theory formulation, the assumption of incompressible flow is used in order to simplify the solution. Because of this assumption, it is required that a compressibility correction is applied according to the freestream Mach number (M_∞) [15], otherwise the solution will be inaccurate. Usually, compressibility effects become significant beyond $M_\infty = 0.3$. The simplest correction available is the Prandtl-Glauert rule, which consists of applying a transformation to the geometry along the x axis. More specifically, the equivalent wing in incompressible flow is a lengthened version of the original one, stretched by a factor $\beta = \sqrt{1 - M_\infty^2}$. Despite its simplicity, direct application of Prandtl-Glauert in a three-dimensional vortex lattice would result in a pressure distribution that would not accurately describe the induced drag [16].
In order to solve this issue, Melin et al.[16] developed a different scheme for applying the Prandtl-Glauert rule. This approach could be used to effectively correct results for the effects of compressibility.
In this approach, VLM is initiated as usual, solving for the incompressible vortex strength distribution Γ_i. Once the incompressible vortex strengths are computed, the compressible vortex distribution can be computed through Eq.(2.19), where the incompressible vortex strength at each panel is multiplied with the Prandtl-Glauert correction factor:

$$\Gamma_c = \frac{1}{\beta}\Gamma_i \quad (2.19)$$

The induced velocity at the vortex core is then computed using the compressible vortex strength as:

$$Q_{\Gamma_c} = a_i\Gamma_c \quad (2.20)$$

where, a_i is the aerodynamic influence coefficient.
The compressible vortex induced velocity in three-dimensional space form is added to the

velocity contributions from the freestream to give:

$$Q_{eff} = Q_{\infty} + Q_{\Gamma_c} \quad (2.21)$$

The compressible vorticity and effective velocity at the vortex core is then used to compute the lift acting on each panel, i.e., the Kutta-Joukowski theorem is rewritten in the form:

$$\Delta L = \rho Q_{eff} \Delta\Gamma_c \Delta y \quad (2.22)$$

Similarly, the induced drag calculation is modified to be:

$$\Delta D_i = -\rho w_{ind} \Delta\Gamma_c \Delta y \quad (2.23)$$

The lift and drag distribution is integrated to obtain total lift and drag. The application of this compressibility correction rule allows the expansion of the envelope within which it is reasonable to analyze a straight untapered wing with VLM codes up to $M_{\infty} = 0.7$. After this point, the appearance of supersonic flow regions across the wing is almost certain (i.e., the critical Mach number is reached), invalidating the usage of such a formulation.

2.4 Computational Improvements

Given the initial implementation of the VLM from Katz and Plotkin [13], various modifications were introduced. Probably, the most profound alteration was the insertion of the decambering approach. This approach needs the solution of a huge number of linear systems for each perturbation iteration, which leads to a significantly performance degradation. The answer to this bottleneck was undoubtedly related with code parallelization.

The VLM solver was subjected to a thorough investigation, searching for areas that were candidate to an efficient parallelization. This investigation showed that the calculation of the Jacobian matrix of the decambering approach was a good candidate for parallelization. To compute this matrix, each of the wing sections have to be perturbed. In the first implementation, the perturbations were made sequentially. More recently, the code was rewritten to ensure thread safety and avoid data races, thus allowing the introduction of a parallel computation. To implement the parallelization, the OpenMP API (Application Programming Interface) was used. Apart from these modifications, the old linear solvers were substituted by new parallel and highly optimized routines, exploring the last SIMD (Single instruction, multiple data) and MIMD (multiple instruction, multiple data) CPU instructions, in order to decrease computational time.

All the above mentioned modifications, led to performance improvements superior to 1000%. In fact, the computation time needed to perform a calculation of wing coefficients in the non-linear mode is very close to the initial linear calculation.

2.5 Validation

The non-linear VLM using the iterative decambering approach, has been implemented for the analysis of multiple-lifting-surface configurations. This custom VLM code was named VLM3D.

In this section, various test results from VLM3D are presented for several airfoil lift curves, different planform shapes and several lifting-surface configurations. The test cases are organized as follows:

1. In this test case a comparison between the results predicted with the current method and the experimental results from Ostowary and Naik [17] is done. In their work [17], experimental $C_l - \alpha$ data for the NACA 4409 airfoil at Reynolds numbers of 0.25 million are presented along with experimental $C_L - \alpha$ data for finite constant-chord wings of several aspect ratios with the same airfoil and at the same Reynolds numbers. In this test case, the two-dimensional experimental data has been used as input for the method and the predicted finite wing lift curves have been compared with the experimental data.

2. The goal of the second test case is to verify the accuracy of the predicted $C_L - \alpha$ curve, as in the previous test, and also to compare the drag polar computed with the proposed method, with experimental results from Sivells [18]. In this work [18], experimental $C_L - \alpha$ and $C_D - C_L$ data for finite trapezoidal wings, with and without washout, are presented. The experimental survey used two NACA five digit airfoils: 64-210 and 65-210. Despite of this, only data from NACA 65-210 finite wings is used for validation purposes. Contrasting with the first test case, there is not two-dimensional experimental data from [18]. Thus, the two-dimensional experimental data used as input for the aerodynamic solver is from [19].

3. The third test case aims to illustrate the effectiveness of the current implementation of VLM method for a multiple lifting-surface configuration. In this example, the geometry considered is a high aspect ratio (AR = 10) constant-chord wing with a conventional aft tail. A single symmetric airfoil is assumed for both wing and tail. The airfoil lift curve is an hypothetical lift curve presented in Fig.2.13(a). The results computed with VLM3D are then compared with a similar calculation from reference [7].

2.5.1 Test Case 1 - Naik and Ostowari Experimental Validation

In this section, two-dimensional experimental data from [17] for a NACA 4409 airfoil at Reynolds numbers of 0.25 million is used as input to generate results for rectangular wings of aspect ratios 12 and 9, using VLM3D. The planforms of the two rectangular wings used are shown in Fig.2.6. The results from the iterative decambering approach are then compared with the experimental $C_L - \alpha$ curves for the corresponding wings from the experimental data of Naik and Ostowari [17].
The following sub-sections present the results for each case.

2.5.1.1 Rectangular Wing (AR=12) with NACA 4409 Airfoil

In this case, the airfoil $C_l - \alpha$ curve is from the experimental data [17] for the NACA 4409 airfoil at Re = 0.25×10^6. The rectangular wing of aspect ratio 12, as shown in Fig.2.6(a) is considered. Figure 2.7 shows the wing $C_L - \alpha$ curves calculated using VLM3D. In the same figure, the airfoil $C_l - \alpha$ curve and the wing $C_L - \alpha$ curve from experiment [17] are also shown for comparison.

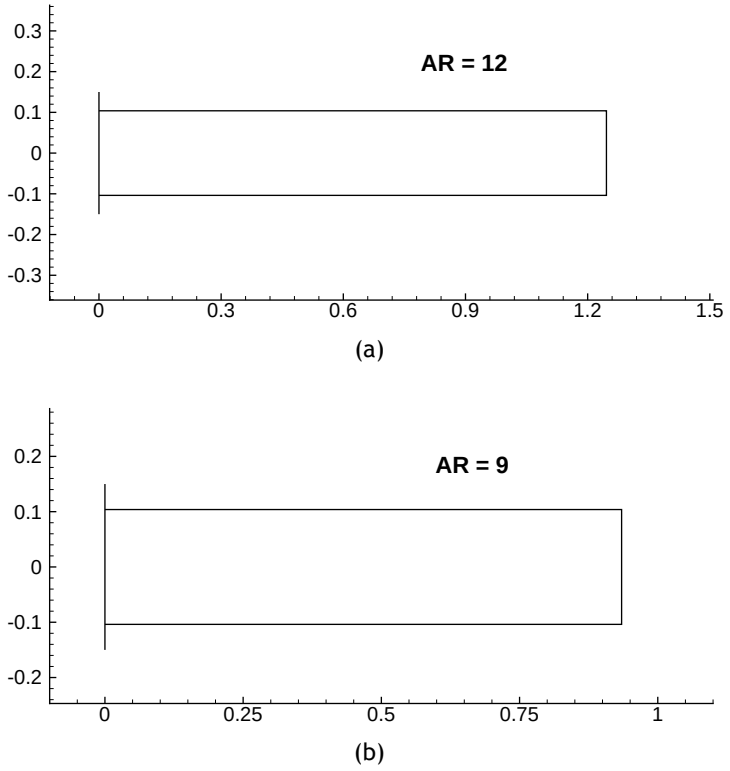

Figure 2.6: Planform of the rectangular wings used in Naik and Ostowari Experimental Validation (only right wing portion shown).

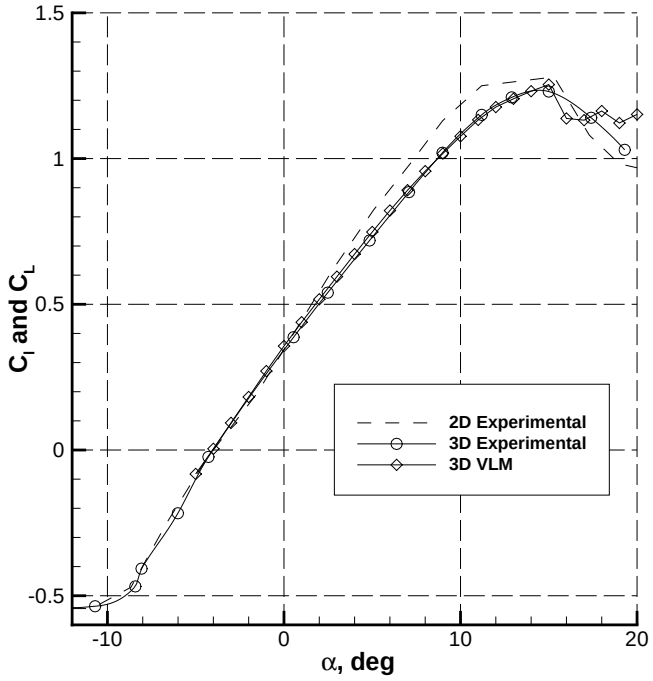

Figure 2.7: Wing $C_L - \alpha$ predicted using VLM3D for a rectangular wing of aspect ratio 12, using a NACA 4409 airfoil at Reynolds number of 0.25 million.

Observing Fig.2.7, it is possible to conclude that a very good agreement exists between the

experimental data and the numerical data computed using VLM3D. In fact, the lift curve slope and the zero lift angle are approximated with an error below 1%. Regarding the $C_{L,max}$ calculation, VLM3D predicts a value of 1.25 and the experimental value is 1.23, which gives an overestimate of 1.7%, well below the maximum acceptable error of 5%. Past the stall point the behavior predicted with the aerodynamic tool differs from the experimental data. However, the experimental data is clearly insufficient to draw conclusions.

2.5.1.2 Rectangular Wing (AR=9) with NACA 4409 Airfoil

In the second wing, the same airfoil $C_l - \alpha$ curve is used, from the experimental studies of Naik and Ostowari [17]. The rectangular wing studied has an aspect ratio of 9, as shown in Fig.2.6(b). Figure 2.8 shows the wing $C_L - \alpha$ curves from VLM3D calculations. In the same figure the airfoil $C_l - \alpha$ curve and the wing $C_L - \alpha$ curve from experiment [17] are also shown for comparison.

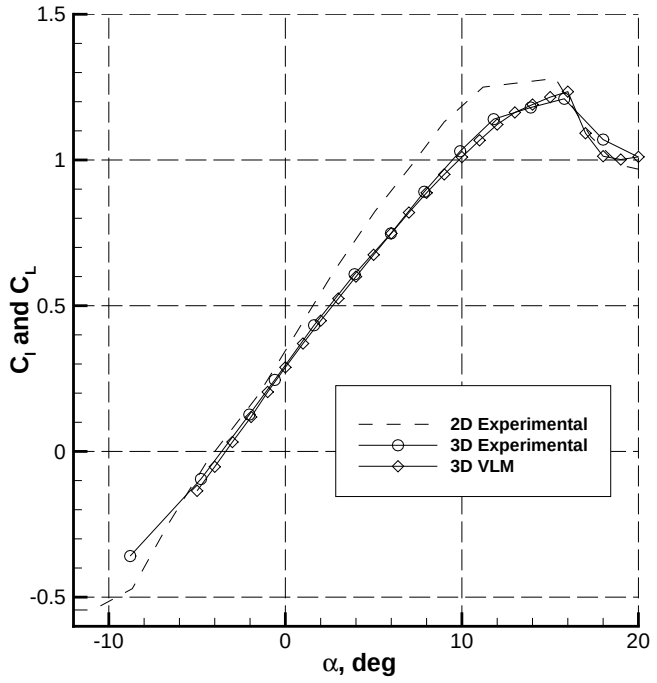

Figure 2.8: Wing $C_L - \alpha$ predicted using VLM3D for a rectangular wing of aspect ratio 9, using a NACA 4409 airfoil at Reynolds number of 0.25 million.

In the second wing studied, very similar conclusions could be drawn. On one hand, a very good agreement exists between the experimental data and the numerical data computed using VLM3D. The zero lift angle and the lift curve slope are approximated with only minor differences. In the present case, the value of $C_{L,max}$ predicted by VLM3D is 1.23 and the experimental value is 1.20, which gives an overestimate of 2.5%, a little higher than in the previous case studied. Past the stall point, the behavior predicted with the aerodynamic tool closely follows the experimental data.

2.5.2 Test Case 2 - Sivells Experimental Validation

In this section, two-dimensional experimental data [19] for a NACA 65-210 airfoil at Reynolds numbers of 4.4 million, is used as input to generate results for trapezoidal wings with 0° washout

and with 2° washout, using VLM3D. The planform of the tested trapezoidal wing is shown in Fig.2.9.
The results from the iterative decambering approach are then compared with the experimental $C_L - \alpha$ and $C_D - C_L$ curves for the corresponding wings from the experimental data of Sivells [18].
The following sub-sections present the results for each case.

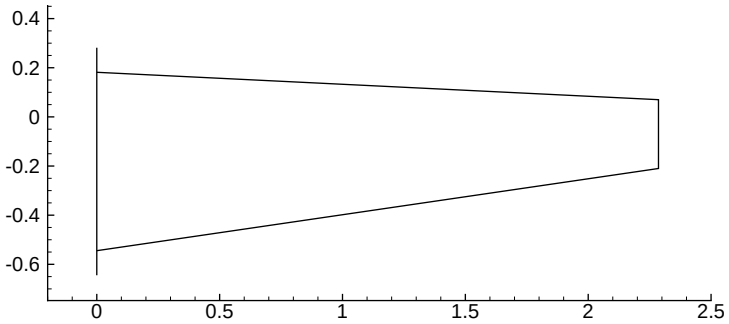

Figure 2.9: Planform of the trapezoidal wing (only right wing portion shown).

2.5.2.1 Trapezoidal Wing with 0° Washout with a NACA 65-210 Airfoil

Figure 2.10(a) shows the two dimensional $C_l - \alpha$ curve, three-dimensional $C_L - \alpha$ curve calculated with VLM3D and also the experimental $C_L - \alpha$ curve, for a wing without washout. Comparing the calculated and experimental lift slope curves, it is possible to observe a very good agreement between the referred curves. In fact, $C_{L,max}$ is predicted within 3% error margin and the lift curve slope $dC_L/d\alpha$ is estimated with an error below 1%. The post-stall prediction with VLM3D reveals the same trend as in the experimental data. However, there is not sufficient experimental data to corroborate this statement. Figure 2.10(b), shows the two dimensional $C_d - C_l$ curve, three-dimensional $C_D - C_L$ curve calculated with VLM3D and also the experimental $C_D - C_L$ curve, for a wing without washout. Again, a very good agreement is seen between experimental data and VLM3D data. Thus, C_{D0} and $C_{D,min}$ are predicted with accuracy.

2.5.2.2 Trapezoidal Wing with 2° Washout with a NACA 65-210 Airfoil

Figure 2.11(a) shows the two dimensional $C_l - \alpha$ curve, three-dimensional $C_L - \alpha$ curve calculated with VLM3D and also the experimental $C_L - \alpha$ curve, for a wing with 2° washout. Again, a very good agreement between the referred curves is observed. In fact, $C_{L,max}$ is predicted with an even tighter margin, being the error inferior to 2%. The $dC_L/d\alpha$ is also estimated with accuracy. On the other hand, the post-stall prediction with VLM3D reveals a smooth lift coefficient decrease that contradicts the abrupt stall shown in the experimental curve. However, the lack of sufficient post-stall measurements invalidates a conclusion to be taken. Figure 2.11(b) shows the two dimensional $C_d - C_l$ curve, three-dimensional $C_D - C_L$ curve calculated with VLM3D and also the experimental $C_D - C_L$ curve, for a wing with 2° washout. Observing the calculated and experimental $C_D - C_L$, it is possible to verify a good compliance. In fact, these curves almost coincide with each other, being the predictions of C_{D0} and $C_{D,min}$ very close to the experimental results.

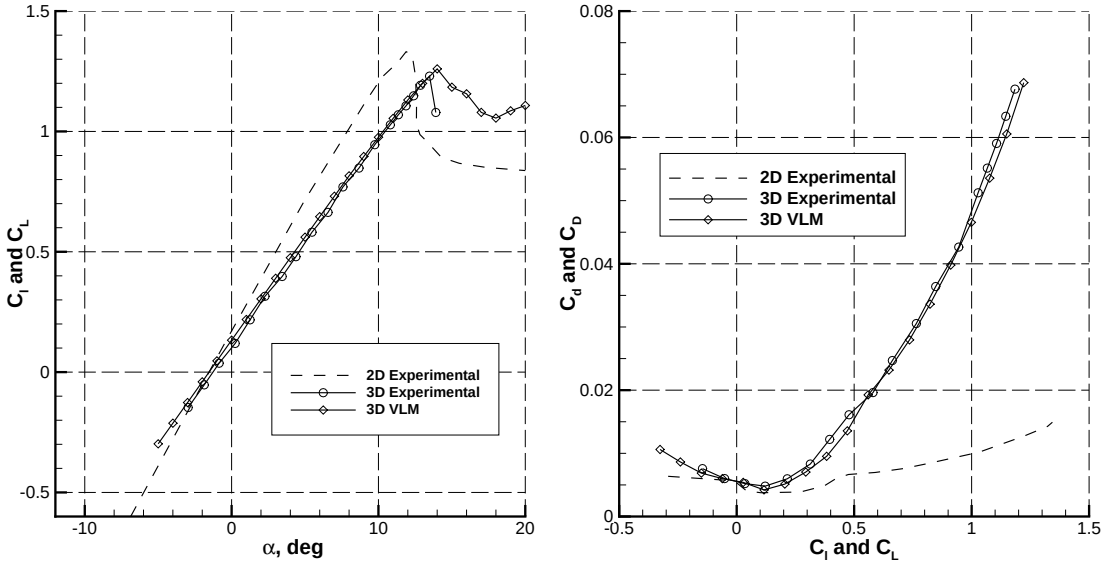

Figure 2.10: Wing $C_L - \alpha$ and $C_D - C_L$ predicted using VLM3D for a trapezoidal wing without washout, using a NACA 65-210 airfoil at Reynolds number of 4.4 million.

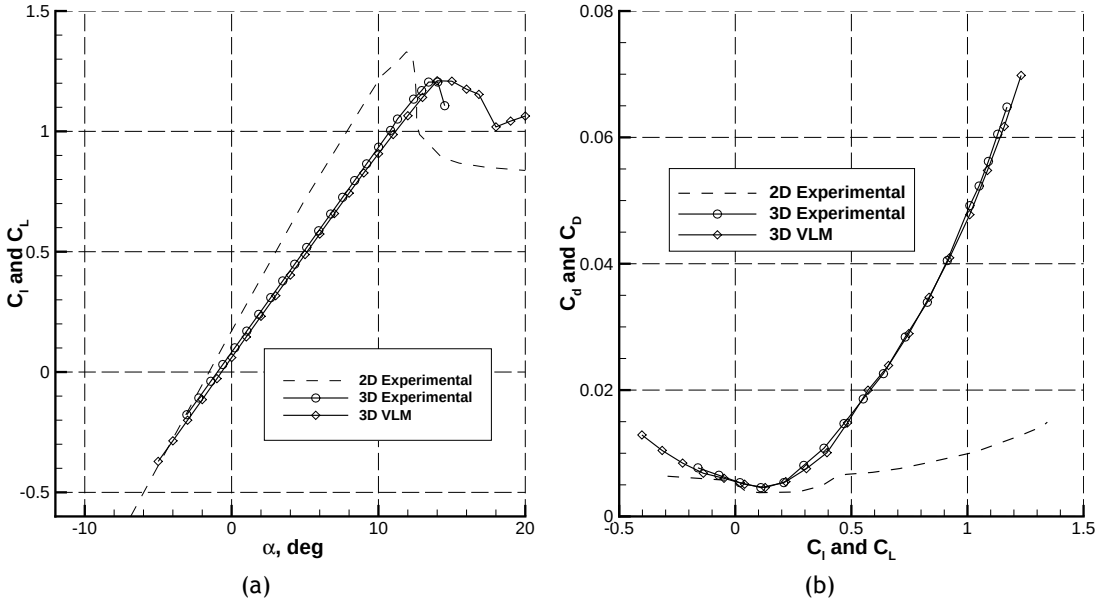

Figure 2.11: Wing $C_L - \alpha$ and $C_D - C_L$ predicted using VLM3D for a trapezoidal wing with 2° washout, using a NACA 65-210 airfoil at Reynolds number of 4.4 million.

2.5.3 Test Case 3 - Wing/Tail Configuration

This example illustrates the effectiveness of the method for a multiple lifting-surface configuration. The geometry considered is composed by a high aspect ratio (AR = 10) constant-chord wing and a conventional aft tail. The planform for the wing-tail configuration is shown in Fig.2.12. A single symmetric airfoil is assumed for both the wing and tail. The tail incidence is selected to be -5°. The results are compared against a similar case from reference [7]. The airfoil lift curve is the same used by the reference considered. A hypothetical lift curve is shown in Fig.2.13(a).

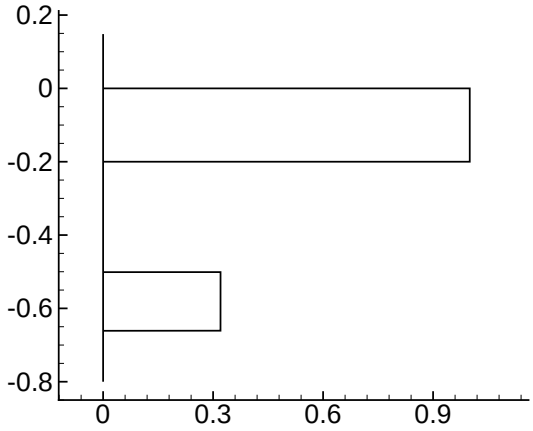

Figure 2.12: Planform of the wing-tail configuration (only right portion shown).

Results for the lift coefficient of the wing, tail and the sum of both are presented in Fig.2.13(b). In the same figure, the curves obtained in the reference considered are also presented for comparison purposes.

In Fig.2.13(b), lift coefficient of wing and tail alone, along with the wing-tail total $C_L - \alpha$ is presented. Results calculated with the present implementation are plotted along with the results from Rinku et al. It must be mentioned that the tail lift coefficient in this plot is nondimensionalized with reference to the tail area.

Observing the referred graph, a very good agreement exists between the curves calculated with the present implementation and with Rinku et al. implementation. Until α is increased to about 17°, the wing and tail C_L continues to increase. Past this AOA, the wing starts to stall. In this zone, there is a slightly difference between both implementations. In fact, the current method predicts a smaller value to wing $C_{L,max}$. However, after the stall both implementations converge to almost the same value.

In this example, the tail remains unstalled over the entire α range considered.

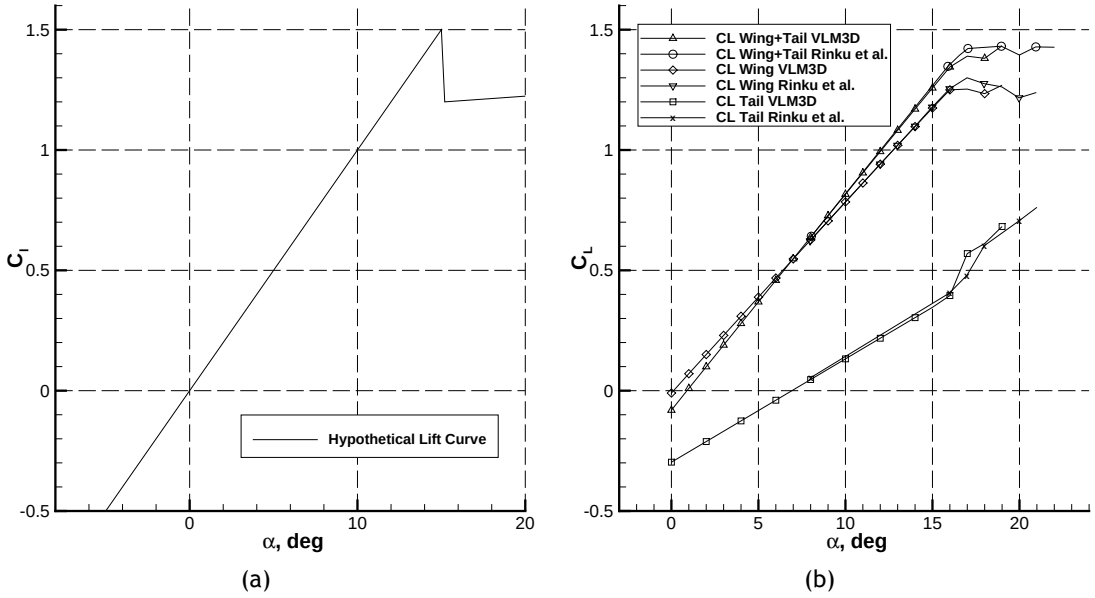

Figure 2.13: Figure showing: a) hypothetical airfoil lift curve (from ref.[7]) and b) individual contributions of the wing and tail to the total lift of the wing-tail configuration.

2.5.4 Summary

The validation procedure carried out showed that the aerodynamic tool is capable of predicting both linear and non-linear characteristics of both wing alone and also multi-lifting surfaces, with high accuracy. This is an important step in order to achieve an aero-structural solver that is capable of analyzing the static aero-structural response of wings effectively.

Chapter 3

Structural Solver

3.1 Equivalent Plate Theory and Implementation

The implementation of this theory by Gamboa and Melo [20] is mainly based on the work of Kapania and Liu [10], in which a first order shear deformation theory (FSDT) was applied to create an EPM of a wing. A computer code was then developed in FORTRAN to evaluate the performance of the structure according to such a model. The current work was then about to enhance the performance of the current implementation and also to create the way to interconnect this program with the aerodynamic solver.

3.1.1 Mathematical Formulation

As previously said, the implementation described here mainly follows the work of Kapania and Liu [10]. An outline of the methodology is presented next.
There are two main assumptions to this formulation: a line normal to the non-deformed mid-surface remains straight after deformation, and the transverse normal stress may be neglected in the constitutive equations. Therefore, the displacement field has the following form:

$$\begin{aligned} u(x,y,z,t) &= u_0(x,y,t) + z\phi_x(x,y,t) \\ v(x,y,z,t) &= v_0(x,y,t) + z\phi_y(x,y,t) \\ w(x,y,z,t) &= w_0(x,y,t) \end{aligned} \quad (3.1)$$

where u, v and w are the displacements in x, y and z directions, respectively, and ϕ_x and ϕ_y are rotations about the x and y axes, respectively. The strains are given by:

$$\begin{aligned} \varepsilon_1 &= \varepsilon_{xx} = \frac{\partial u}{\partial x} = \frac{\partial u_0}{\partial x} + z\frac{\partial \phi_x}{\partial x} \\ \varepsilon_2 &= \varepsilon_{yy} = \frac{\partial v}{\partial y} = \frac{\partial v_0}{\partial y} + z\frac{\partial \phi_y}{\partial y} \\ \varepsilon_3 &= \varepsilon_{zz} = \frac{\partial w}{\partial z} = 0 \\ \varepsilon_4 &= \gamma_{xy} = 2\varepsilon_{xy} = \frac{\partial u}{\partial y} + \frac{\partial v}{\partial x} = \frac{\partial u_0}{\partial y} + \frac{\partial v_0}{\partial x} + z\left(\frac{\partial \phi_x}{\partial y} + \frac{\partial \phi_y}{\partial x}\right) \\ \varepsilon_5 &= \gamma_{yz} = 2\varepsilon_{yz} = \frac{\partial v}{\partial z} + \frac{\partial w}{\partial y} = \frac{\partial w_0}{\partial y} + \phi_y \\ \varepsilon_6 &= \gamma_{zx} = 2\varepsilon_{zx} = \frac{\partial w}{\partial x} + \frac{\partial u}{\partial z} = \frac{\partial w_0}{\partial x} + \phi_x \end{aligned} \quad (3.2)$$

The strain energy of the wing structure is:

$$U = \frac{1}{2}\int\int\int_V \{\sigma\}^T\{\varepsilon\}\, dV = \frac{1}{2}\int\int\int_V \{\varepsilon\}^T[D]\{\varepsilon\}\, dV \quad (3.3)$$

where the constitutive relations for the material (Hooke's Law, establishing the relation be-

tween the stress state $\{\sigma\}$ and the strains $\{\varepsilon\}$) were applied in the form of the tensor $[D]$ (taken as symmetrical). On the other hand, for the kinetic energy of the equivalent plate we have:

$$T = \frac{1}{2}\int\int\int_V \rho\, \mathbf{v}.\mathbf{v}\, dV \quad (3.4)$$

v being the velocity vector:

$$\mathbf{v} = \left(\frac{\partial u_0}{\partial t} + z\frac{\partial \phi_x}{\partial t}, \frac{\partial v_0}{\partial t} + z\frac{\partial \phi_y}{\partial t}, \frac{\partial w_0}{\partial t}\right) \quad (3.5)$$

In order to perform the calculations, the general wing geometry needs to be transformed into the square domain defined by ξ, η, shown in Fig.3.1.

The transformation can be formulated mathematically as:

$$\begin{aligned} x &= \sum_{i=1}^{4} N_i(\xi,\eta)x_i \\ y &= \sum_{i=1}^{4} N_i(\xi,\eta)y_i \end{aligned} \quad (3.6)$$

where,

$$\begin{aligned} N_1(\xi,\eta) &= \frac{1}{4}(1-\xi)(1-\eta) \\ N_2(\xi,\eta) &= \frac{1}{4}(1+\xi)(1-\eta) \\ N_3(\xi,\eta) &= \frac{1}{4}(1+\xi)(1+\eta) \\ N_4(\xi,\eta) &= \frac{1}{4}(1-\xi)(1+\eta) \end{aligned} \quad (3.7)$$

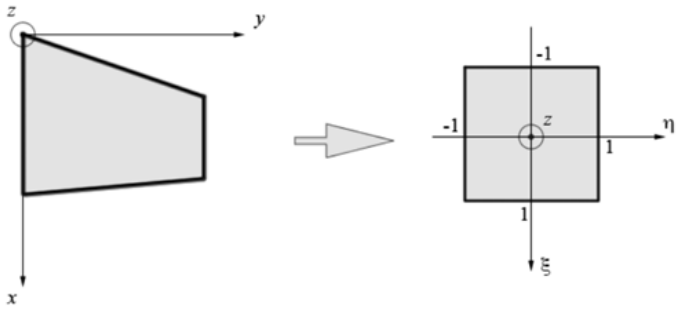

Figure 3.1: Domain transformation used in Kapania and Liu formulation [10].

The application of such transformation and subsequent discretization of Eqs.(3.3) and (3.4) leads to a rather lengthy derivation which goes beyond the scope of the current work (but is again explained in [10] and [21]). In order to evaluate the integrals in the aforementioned equations, Gaussian quadrature is used. The integrands and limits of integration are defined by the geometry of the wing and the properties of its structural elements.

3.1.1.1 Static Deformation

To compute the static deformation of the structure, the work done by external forces must be calculated:

$$Q = \frac{1}{2}\int\int P(x,y,t).(u,v,w)\ dxdy \quad (3.8)$$

where, $\{P\}$ is the generalized load vector, given by:

$$\{P\} = \{\{P_1\}\ \{P_2\}\ \{P_3\}\ \{P_4\}\ \{P_5\}\}^T \quad (3.9)$$

For concentrated loads the components of the generalized load vector are:

$$\begin{aligned}
P_1 &= P_x[x(\xi_a,\eta_a), y(\xi_a,\eta_a), t]\{B_{IJ}(\xi_a,\eta_a)\}^T \\
P_2 &= P_y[x(\xi_a,\eta_a), y(\xi_a,\eta_a), t]\{B_{KL}(\xi_a,\eta_a)\}^T \\
P_3 &= P_z[x(\xi_a,\eta_a), y(\xi_a,\eta_a), t]\{B_{MN}(\xi_a,\eta_a)\}^T \\
P_4 &= zP_x[x(\xi_a,\eta_a), y(\xi_a,\eta_a), t]\{B_{PQ}(\xi_a,\eta_a)\}^T \\
P_5 &= zP_y[x(\xi_a,\eta_a), y(\xi_a,\eta_a), t]\{B_{RS}(\xi_a,\eta_a)\}^T
\end{aligned} \quad (3.10)$$

where (ξ_a, η_a) is the transformed coordinates of the point where the load is applied.
The displacement and rotation functions are then approximated by Legendre weighting functions and the integrals in Eqs.(3.3) and (3.4) are evaluated so that the following system of equations is obtained:

$$[K]\{q\} = \{P\} \quad (3.11)$$

Where $[K]$ is the stiffness matrix obtained through integration of Eq.(3.3), $\{q\}$ is the generalized displacement vector (weighting the Legendre functions) and $\{P\}$ is the generalized load vector. In the current implementation, the loading input is actually the output from the aerodynamics module (VLM3D), which generates a distribution of point loads across the wing surface.

3.1.1.2 Natural Vibration

In order to compute wing natural vibration frequencies and modes, the following generalized eigenvalue problem must be solved:

$$\left[K - \omega^2 M\right]\{x\} = 0 \quad (3.12)$$

where, $[M]$ is the mass matrix resulting from the evaluation of the integral in Eq.(3.4), ω^2 is the eigenvalue (natural frequency squared), and finally, $\{x\}$ is the eigenvector representing the mode shape.

3.2 Computational Improvements

Given the previous implementation, from Gamboa and Melo, some modifications were performed. In the first place, parallel and highly optimized factorization routines were used, to decrease the computational time needed. One other key aspect that was taken into account is

related to code parallelization. The EPM code was subjected to a thorough investigation, searching for areas that were candidates to an efficient parallelization. This investigation showed that the structural program has various hot spots that were good candidates for parallelization. For example, the computation of the stiffness matrix needs the sum of the contribution from the various wing components (skins, ribs, spars...). All the contributions are now calculated in parallel, effectively using all the computer resources and thus saving computational time. The code was rewritten to ensure thread safety and avoid data races. To implement the parallelization, the OpenMP API (Application Programming Interface) was used.

3.3 Validation

In order to assess the accuracy of the current implementation of the equivalent plate method and also its performance, a set of tests were carried out for a general trapezoidal wing composed of skins, spars, and ribs. The results obtained with the present method were compared against a commercial finite element model. The geometric and material parameters of the trapezoidal wing are given in table 3.1. Notice that the plate is clamped at the root.

Table 3.1: Geometric and material properties of the test wing

Geometric properties		Material Properties	
Semispan, $\frac{b}{2}$	4.88 m	mass density, ρ	2700kg/m^3
Tip twist	0 deg	Young's modulus, E	70.7 GPa
LE Sweep, Λ_{LE}	30 deg	Poisson's ratio, ν	0.3
Dihedral, φ	0 deg		
Root chord, c_r	1.83 m		
Tip chord, c_t	0.91 m		

All the wing components (spars, ribs and skin) are made of aluminum. There are two skin panels covering its upper and lower parts. In particular, the wing components dimensions are the following: skin thickness t_0 = 3mm, spar cap height h_1 = 5mm, spar cap width l_1 = 9.47mm, spar web thickness t_1 = 1.47mm. Notice that the ribs have the same cap dimensions and web thickness as the spars. All components dimensions are summarized in table 3.2.
The airfoil thickness-to-chord ratio varies from 0.15 at the root to 0.06 at the tip. Notice that both root and tip airfoils were obtained through a Karman-Treftz conformal transformation [22]. A general CAD model of the trapezoidal wing used in the equivalent plate validation tests is seen in Fig.3.3.

3.3.1 Modal Analysis

The modal analysis is carried out using the present equivalent plate model. These results are then compared to the corresponding finite element model in ANSYS®.
Table 3.3 compares the modal frequencies between the equivalent plate model and the finite element model from reference [21]. Observing the results, one can conclude that the present equivalent plate model is capable of approximating the modal frequencies. Nevertheless, in

Table 3.2: Structural components position and dimensions used in the test wing.

Structural variable	Value
Spars position [chord fraction] (root and tip)	0.2/0.4/0.6/0.8
Spar web thickness (root and tip)	1.47 mm
Spar cap height (root and tip)	5.00 mm
Spar cap width (root and tip)	9.47 mm
Ribs position [semispan fraction] (LE and TE)	0.0909/0.1818/0.2727/0.3636/ 0.4545/0.5455/0.6364/0.7273/ 0.8182/0.9091/1.0
Rib web thickness	1.47 mm
Rib cap height	5.00 mm
Rib cap width	9.47 mm
Skin thickness	3.0 mm

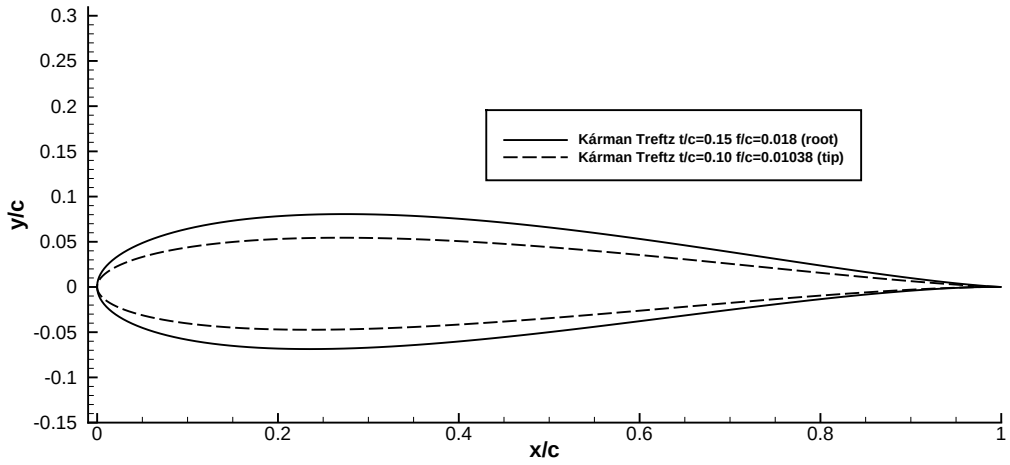

Figure 3.2: Tip and root airfoils used in the tested wing.

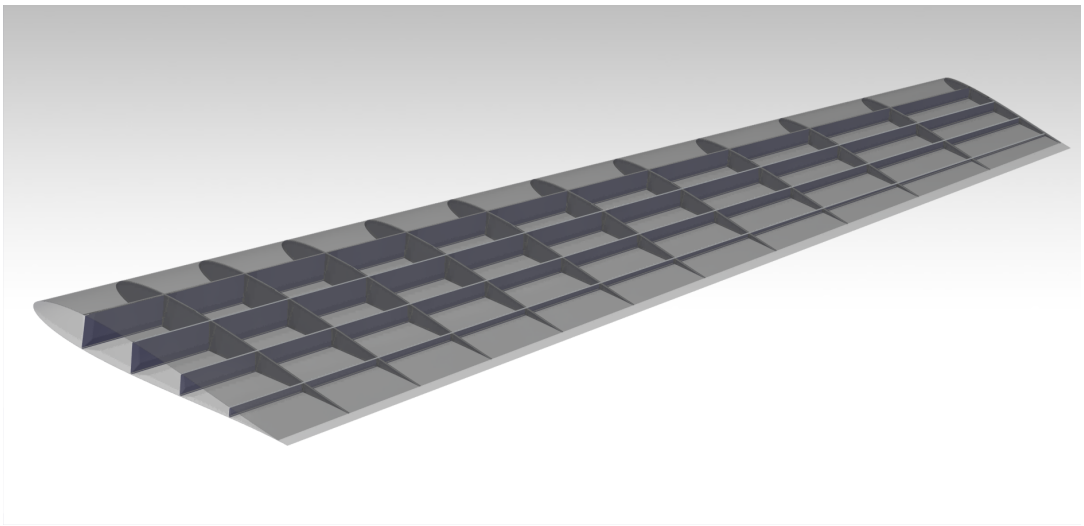

Figure 3.3: CAD model of the trapezoidal wing used in the equivalent plate validation tests. Note that the skins are transparent, revealing the spars and ribs inside the wing.

order to improve the numerical results, a high number of integration points is necessary. Despite of this, the 5th modal frequency shows a relatively high error, being overestimated by about 8.4%. This comparison shows that EPM is capable of predicting modal frequencies with a very good agreement.

Table 3.3: Comparison of natural vibration frequencies computed with EPM and FEM.

Mode	EPM [rad.s^{-1}]	FEM [rad.s^{-1}]	Error [%]
1st	46.451	46.639	0.4
2nd	203.408	200.068	1.67
3rd	280.541	284.249	1.3
4th	371.215	358.933	3.42
5th	496.568	458.022	8.42
6th	744.267	726.96	2.38

3.3.2 Static Load Analysis

In order to perform the analysis under static loads, a pair of loads, equal in magnitude (4448 N) and opposite in direction are applied at the wing tip (at the locations of the first and last spars).

The deformations along the wing leading edge and the wing tip are compared against the corresponding finite element model from reference [21]. Figure 3.4(a) shows the displacement results along the wing leading edge and Fig.3.4(b) the deformation at the wing tip.

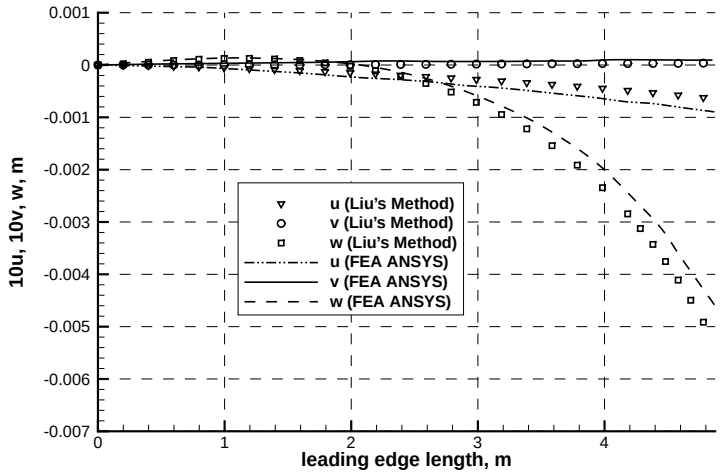

(a) Wing leading edge deflection.

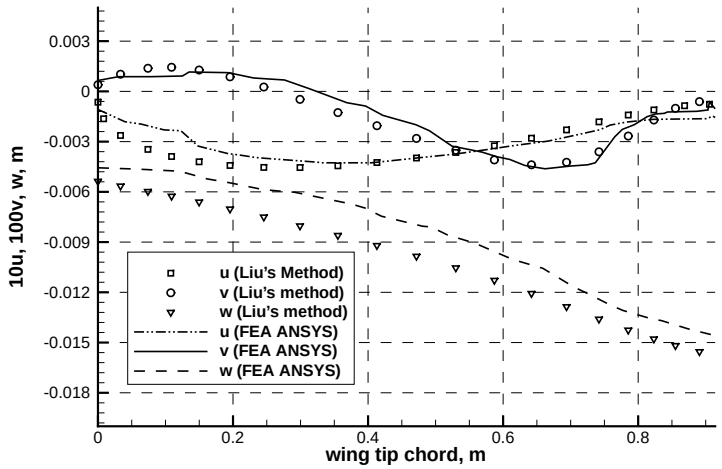

(b) Wing tip deflections.

Figure 3.4: Displacement of the test wing, due to a torque application.

Regarding the leading edge displacement, the equivalent-plate model overestimates the w deformation and underestimates the u deformation but even though a very close approximation for both deformations is obtained. The v deformation practically coincides with the finite element calculations, being approximated with the highest accuracy among the three displacements.
Along the wing tip, Liu's method captures the trend of the displacement field very accurately. On one hand, deformations u and v are approximated very precisely, almost coinciding with the finite element model. On the other hand, deflection w is slightly overestimated. However, it is clear that the approximation given by EPM has a good accuracy.

3.3.3 Summary

The validation procedure carried out showed that the EPM tool is capable of predicting both modal frequencies and static deformation with sufficient accuracy. On the other hand, the

simplicity in parameterizing the structure and the low computational cost of such an implementation when compared with an equivalently detailed finite element model, makes the EPM a good method for preliminary wing design phases.

Chapter 4

Aero-structural Solver

The purpose of the current chapter is to provide a detailed insight into the aero-structural model implementation. An overview of the computational implementation details is also made, effectively showing the decisions taken and their impact on the final result. The capabilities added by the Graphical User Interface (GUI) and its improvements in the user experience, are also addressed. Finally, numerical results are presented for the deformation under aerodynamic loads for a general wing composed by skin, spars and ribs.

4.1 Aero-structural Model Implementation

After describing the aerodynamic and structural disciplines, the aero-structural solver could be formulated and implemented.
One of the essential aspects in the aero-structural formulation is the transfer of the coupling variables between the aerodynamic and structural analysis [23]. There are two mainly aspects involved that need to be addressed during the information transfer. The first one is the level of fidelity in the coupling of the aerodynamic and structural model, which has to guarantee that the accuracy of the individual analyses is not compromised. The second concern is that the discretization in each model must preserve geometric consistency during the analysis process. The aerodynamic and structural solvers coupling in the context of the aero-structural analysis is shown in Fig.4.1.

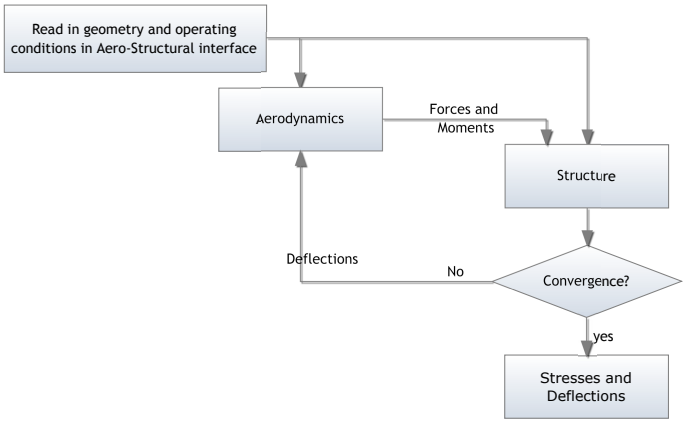

Figure 4.1: Aerodynamic and structural solvers coupling methodology.

4.1.1 Mathematical Formulation

The aero-structural analysis is done through the transfer of two matrices: the aerodynamic load matrix and the displacement matrix. The aerodynamic solver is responsible to compute the aerodynamic forces generated by the surrounding flowfield. The force vector computed with VLM, has the following form:

$$\begin{aligned} P_{a_x} &= \{f_{x_k}\}^T \\ P_{a_y} &= \{f_{y_k}\}^T, k = 1,\ n_a \\ P_{a_z} &= \{f_{z_k}\}^T \end{aligned} \quad (4.1)$$

where, n_a is the total number of aerodynamic node points and P_{a_x}, P_{a_y} and P_{a_z} are the aerodynamic force vectors in x, y and z directions, respectively. The aerodynamic loads given by Eq.(4.1) are transfered to the EPM, along with the application points. Using the definition given by Eq.(4.1), the generalized vector components are modified to be:

$$\begin{aligned} P_1 &= P_{a_x}[x(\xi_a,\eta_a), y(\xi_a,\eta_a), t]\{B_{IJ}(\xi_a,\eta_a)\}^T \\ P_2 &= P_{a_y}[x(\xi_a,\eta_a), y(\xi_a,\eta_a), t]\{B_{KL}(\xi_a,\eta_a)\}^T \\ P_3 &= P_{a_z}[x(\xi_a,\eta_a), y(\xi_a,\eta_a), t]\{B_{MN}(\xi_a,\eta_a)\}^T \\ P_4 &= zP_{a_x}[x(\xi_a,\eta_a), y(\xi_a,\eta_a), t]\{B_{PQ}(\xi_a,\eta_a)\}^T \\ P_5 &= zP_{a_y}[x(\xi_a,\eta_a), y(\xi_a,\eta_a), t]\{B_{RS}(\xi_a,\eta_a)\}^T \end{aligned} \quad (4.2)$$

The displacement and rotation functions are then approximated by Legendre weighting functions and the integrals in Eqs.(3.3) and (3.4) (treated in section 3.1.1) are evaluated so that the following system of equations is obtained:

$$[K]\{q_a\} = \{P\} \quad (4.3)$$

where $[K]$ is the stiffness matrix obtained through integration of Eq.(3.3), q_a is the generalized displacement vector imposed by the aerodynamic forces (weighting the Legendre functions) and $\{P\}$ is the generalized aerodynamic load vector.

Vector q_a is used to evaluate the Legendre polynomials and the displacements vector is calculated, using the aerodynamic mesh nodes as references. The displacements are then accumulated in a matrix with the form:

$$\Delta\delta = \{u_k, v_k, w_k\}^T, k = 1, n_a \quad (4.4)$$

where, u_k, v_k and w_k are the deformation in x, y and z direction, respectively, corresponding to a particular aerodynamic node. After this calculation, the aerodynamic nodes are updated with the associated deformations. So the updated aerodynamic mesh is:

$$Q_{a_{up}} = Q_a + \Delta\delta \quad (4.5)$$

where Q_a is the matrix of aerodynamic nodes, given by:

$$Q_a = \{x_k, y_k, z_k\}^T, k = 1, n_a \quad (4.6)$$

4.1.2 Aero-structural Iterative Procedure

Given the interaction between the aerodynamic and structural tools, an iterative procedure is the natural approach to solve for the final deflected wing.
The aerodynamic point loads vector computed with the VLM tool is transferred to the structural tool along with the coordinates of the application points. Since in the structural tool there is not an associated mesh, the loads are applied without any pre-processing. Transferring the displacements given from the structural analysis to the aerodynamic module is achieved by generating the deflected aerodynamic mesh. This procedure is straightforward to implement, since the equivalent plate model deflections are computed using Legendre Polynomials, which can be evaluated at any point inside the wing planform. In the current implementation, the deflections are computed at each point of the aerodynamic mesh, and added to the undeformed mesh.
The first time the aerodynamic solver is called, the displacement field of the structure is equal to zero. After the aerodynamic solver completes, aerodynamic forces are transferred and the structural solver is called. The new displacement field is then translated to a movement of the aerodynamic mesh and the aerodynamic solver is called again. This process continues until the state of aerodynamic and structure converged as determined by the norm of the structural displacement residuals. In the current work, the total number of iterations is typically between 5 to 10.
The iteration scheme can be summarized using the following procedure:

1. Start VLM3D aerodynamic program and the Equivalent-Plate structural program;
2. Compute aerodynamic loadings using VLM3D program and transfer loading to coupling variables;
3. Compute deflected wing surface under the aerodynamic loads using the Equivalent-Plate structural program and update the aerodynamic mesh;

This iterative procedure is carried out until a specified tolerance is achieved. In the current work the user can define the tolerance value, which should be between 0.1 and 0.005. This aero-structural solution converges unless the given structural and aerodynamic variables result in a wing that is divergent.

4.2 Aeroelasticity

Aeroelasticity is the study of the interaction of an elastic structure with its fluid surroundings. This interaction may lead to disastrous results if it is not adequately predicted and no steps are taken to control it. The aero-structural coupling, treated in the previous sections, is an example of aeroelasticity, more specifically, static aeroelasticity.

4.2.1 Flutter

A phenomenon known as flutter consists of the dynamic interaction between the structure itself and the aerodynamic loads. Although types of flutter based on excitation of pure bending or pure torsion modes are stable, the same is not verified for cases where these types of motion coexist with a certain phase difference. This is known as the classical flutter. A common

example is presented in Fig.4.2, where a 90° phase difference exists, between the bending and torsion modes.

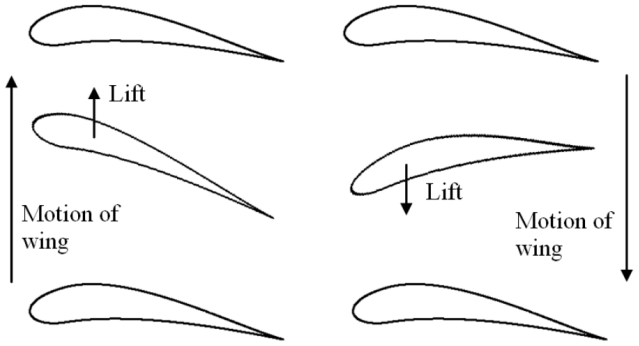

Figure 4.2: Figure showing the classical flutter phenomenon [24].

It is immediately apparent that while crossing the equilibrium position in bending, the wing suffers both maximum and minimum lift loads due to the twist-increased/decreased angle of attack. The fact that these loads are synchronous with the motion of the wing means that at a given speed, V_f (flutter speed), the aerodynamic loads surpass the admissible values and the oscillations quickly diverge, eventually leading to structural collapse. There are also other types of flutter, mainly the aileron buzz, buffeting and stalling flutter. However, these are often considered as non-classical flutter.

4.2.2 Flutter Speed Prediction Implementation

Having the capability of predicting the natural frequencies of a wing structure, semi-empirical expressions to predict flutter speed can be derived. The current approach use the relation introduced in [25], in order to estimate the flutter speed of trapezoidal wings.

$$V_f = \frac{\omega_\alpha r_\alpha}{\sqrt{2C_{L_\alpha}\rho\epsilon\frac{b/2}{m_{wing}}}} \quad (4.7)$$

where, ω_α is the first uncoupled torsional frequency of the wing structure, r_α is the radius of gyration of the wing expressed as a fraction of the average semi-chord, ρ is the freestream air density, ϵ is the distance from the wing section center of mass to the aerodynamic center (1/4 chord) as a fraction of the chord and C_{L_α} is the slope of the wing lift curve.

The proposed equivalent-plate model (EPM) is used to determine wing frequencies and wing mass. On the other hand, the aerodynamic solver is used to compute the lift curve slope of the wing (C_{L_α}). So, to evaluate Eq.(4.7) one call to each program has to be made.

The values of r_α and ϵ are by default estimated to be $r_\alpha = 0.5$ and $\epsilon = 0.25$, as suggested in reference [25]. In the future, given the wing geometry, the program can be easily extended so that these two parameters can be automatically calculate.

4.3 The Aero-Structural Program Implementation

Given the requirement of modularity, each discipline should be completely independent executable programs. This poses problems related with computational efficiency when transferring the coupling variables. The "classical" approach would be to write the data to text files, that would be red by the other discipline. However, this would drastically reduce computational efficiency and consequently would slow down the tool.
To overcome the presented problem, the coupled aero-structural iteration scheme is implemented in a high performance environment, in which the coupling variables are all transferred through dynamic-link-libraries (DLL's). This allows high speed data sharing and processing, without compromising the modularity of both programs. Using this approach all the data are transferred through the computer's high speed RAM, avoiding the overhead of using the low-speed computer hard-disk.
Both aerodynamic and structural programs are responsible to write its calculations to the DLL shared variables. However, to better coordinate the aero-structural analysis, an intermediate program, called aero-structural interface, was written. This program is responsible for starting and coordinating the calculation and also for doing the required convergence tests. The airfoil's aerodynamic data needed can also be provided to the program (as a plain text file) or automatically calculated using the XFOIL solver [26]. In XFOIL, the steady Euler equations in integral form are used to represent the inviscid flow, and a compressible lag-dissipation integral method is used to represent the boundary layers and wake. The entire viscous solution (boundary layers and wake) is strongly interacted with the incompressible potential flow via the surface transpiration model which permits proper calculation of limited separation regions. Results from XFOIL have been compared against experimental data with good agreement [27].

4.4 The Aero-Structural Graphical User Interface (GUI)

The way the user interacts with the aero-structural tool is also a very important aspect in the current work. Therefore, a GUI was created to improve the user experience when using and operating the aero-structural solver. The GUI was developed using the GTK+ (Gimp ToolKit [28]) as it is a multi-platform toolkit, offering a complete set of widgets. Since this toolkit is cross-platform, the GUI could easily be ported to Linux, or even to a Mac based computer, without having to completely rewrite the graphical interface. This is a great advantage over using the Microsoft Foundation Class (MFC), since the last one is irremediable tied to Windows based operating system.
The GUI should not break the need for modularity. So, the same executables should be used as standalone applications or with the GUI. The solution to this problem was to use the graphical interface, to automatically start the aerodynamic and structural programs, creating pipes to handle the console "stdin" and "stdout". Using this approach the data written to the application's console is presented in a text frame.
The main GUI window is divided into two main tabs. These are: console view and graphics view. The console view shows all the text that would normally be displayed in the console of each application. The graphics view is responsible to show, in a graphical way, the calculation made with the aerodynamic solver, structural solver or both. Related with the aerodynamic solver, there is a 3D graph showing the current VLM mesh and also a XY graph displaying C_l, lift, α_i, α_{eff}, C_{d0}, C_{di} and C_d distributions. Related with the structural solver, there is a 3D graph that

displays the current equivalent-plate surface and the corresponding u, v, w deformations and also skin $\sigma_{VonMisses}$, σ_x, σ_y and $\tau_x y$. An expansion to display all the wing components stresses is planned in the near future. The console view and the graphics view can be seen in Fig.4.3 and Fig.4.4, respectively.

In the bottom portion of both tabs there are four buttons, as seen in Fig.4.3. Starting from the left, the first one starts the selected analysis. The second is the most important button, since it is responsible for accessing the options related to all features of the aero-structural solver. The third button, the about button, is, as the name indicates, used to find more information about the program, the author and the modules used to make it possible. The last button quits the application. When the options button is clicked for the first time, the user has the possibility

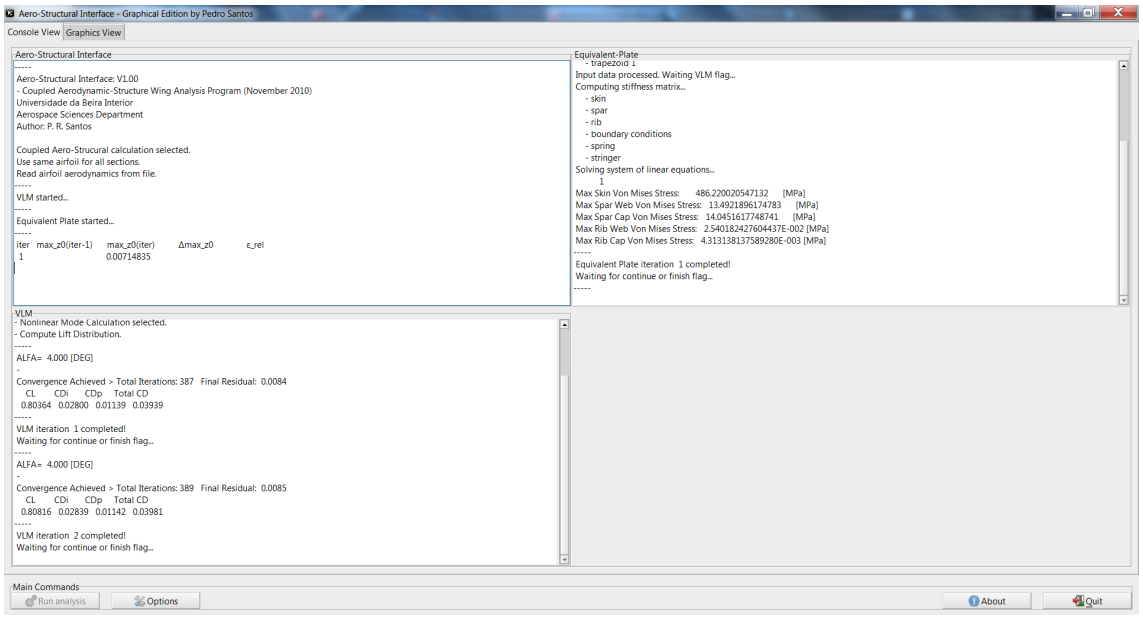

Figure 4.3: Screenshot showing the console redirection tab. The normal operation text during an aero-structural analysis is shown.

to load a configuration file. This feature greatly enhances user experience, since a previously configured analysis could be loaded without any effort. Note that there is the possibility to work with the loaded configuration file without updating it, and thus preserving the original file untouched. After loading the configuration file, the options dialog is presented. It is composed by a tree that organizes all the options by categories, which greatly simplifies the access to the large number of parameters (more than one-hundred). There is also a 3D viewer for which an OpenGL graphics engine was developed. It has the ability to display in real-time the wing being configured in the options dialog. This viewer also presents zoom, pan and rotate capabilities and is capable of rendering wing shadow and reflections. It also supports anti-aliasing to enhance render quality. The options dialog and 3D viewer are shown in Fig.4.5.

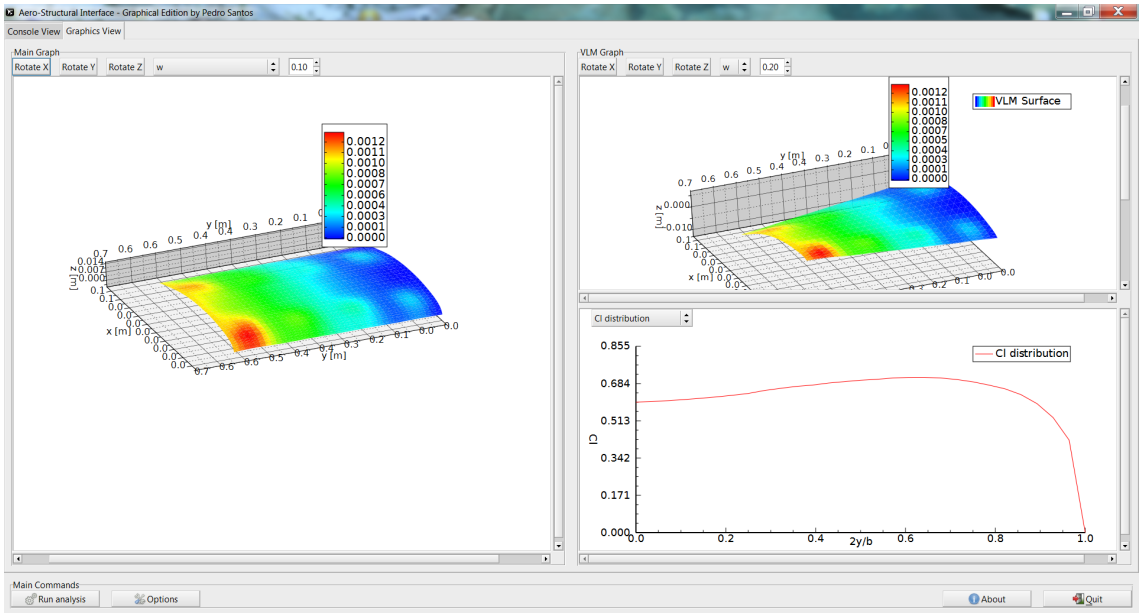

Figure 4.4: Screenshot showing the graphics tab. Note that in the aerodynamic XY graph the C_l distribution is selected and that in the main graph, the w deformation is selected.

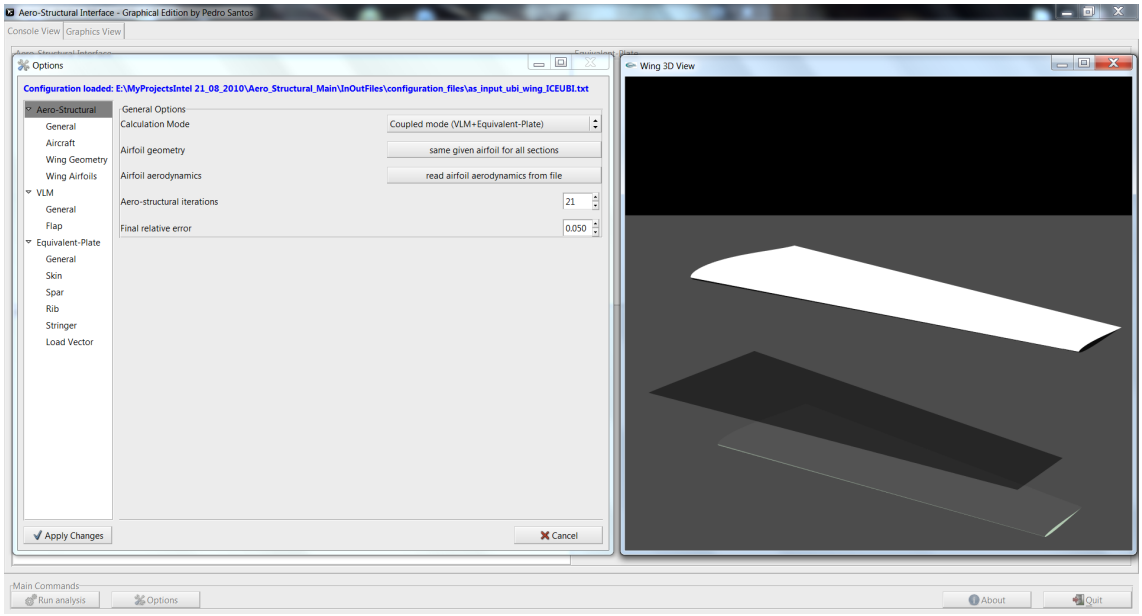

Figure 4.5: Screenshot showing GUI options dialog and the OpenGL 3D viewer.

4.5 Numerical Study

In order to evaluate the results computed with the current implementation of the aero-structural methodology and also its performance, a numerical study is carried out for a rectangular wing composed of skins, spars, and ribs.

4.5.1 Wing Structural and Geometric Considerations

To test the aero-structural tool, a rectangular wing is considered. The wing geometry and materials are chosen to match the ones used to build the experimental wing (which is the subject of the next chapter). So, a similarity exists between the numerical and the experimental wing. The geometric and material parameters of the rectangular wing are given in Table 4.1.

Table 4.1: Geometric and material properties of the rectangular wing used in aero-structural analysis.

Geometric properties		Skin and Spar Material (Aluminium 6061 T6) [30]		Ribs material (Airex C70.75) [29]	
Semispan, b/2	0.6 m	mass density,	2700 kg/m^3	mass density,	80 kg/m^3
Tip twist	2°	Young's modulus,	68.9 GPa	Young's modulus,	66 MPa
Dihedral,	0.6°	Shear Modulus,	26 GPa	Shear Modulus,	30 MPa
chord, c	0.15 m	Poisson's ratio,	0.33	Poisson's ratio,	0.1

The wing considered has two spars, located at 30% and 50% of the chord, and five ribs distributed uniformly along the wing span. Both skin and spars are made of aluminum. In particular, these components have the following dimensions: skin thickness t_0 = 0.4mm, spar cap height h_1 = 0.4mm, spar cap width l_1 = 5mm, spar web thickness t_1 = 0.4mm. The ribs are made of PVC foam Airex® C70.75 with 6.2mm of thickness. Table 4.2 summarizes wing components dimensions and positions. Note that the wing is assumed to be clamped at the root.

Table 4.2: Structural components position and dimensions used in the aero-structural test wing.

Structural variable	Value
Spars position [chord fraction] (root and tip)	0.3/0.5
Spar web thickness (root and tip)	0.4 mm
Spar cap height (root and tip)	0.4 mm
Spar cap width (root and tip)	5.0 mm
Ribs position [semispan fraction] (LE and TE)	0.0/0.25/0.5/0.75/1.0
Ribs thickness	6.2 mm
Skin thickness	0.4 mm

The airfoil chosen for the wing is a modified version of the SG6042. In Fig.4.6 is possible to observe the airfoil contour of the referred airfoil. This airfoil has been chosen mainly because of the flat lower surface, since it will facilitate the construction of the test wing (which is the subject of the next chapter).

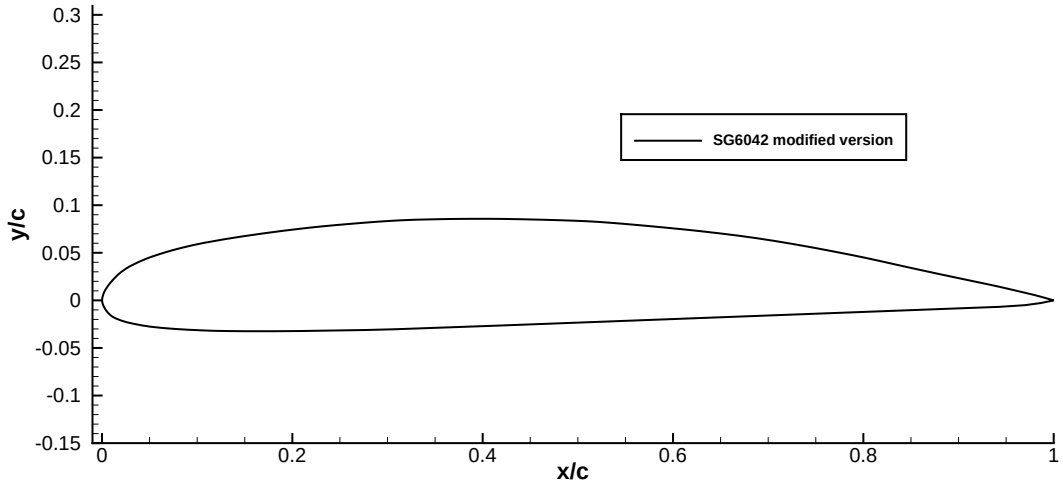

Figure 4.6: Airfoil used for the tip and root wing stations of the tested wing.

The proposed wing was designed in a CAD program. The general CAD model is presented in Fig.4.7.

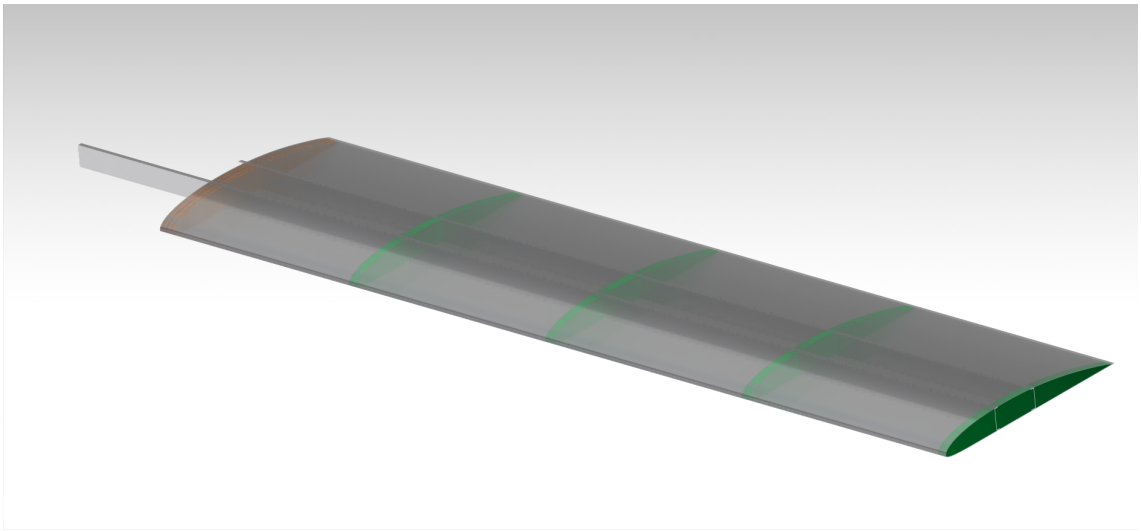

Figure 4.7: CAD model of the wing used in the aero-structural numerical tests. Note that skin is transparent, revealing the spars and ribs inside the wing.

4.5.2 Solid Wall Correction

In an effort to enhance the similarity between the numerical and the experimental results, two solid walls are modeled using the reflection technique described in section 2.1.2. These solid walls are added in the upper and lower surface of the wing and attempt to model the potential effect of the wind tunnel test section lateral walls. These walls are added at a distance of

0.4m, given the total wind-tunnel test section width of 0.8m. Figure 4.8 shows a CAD model of the described wing-walls model.

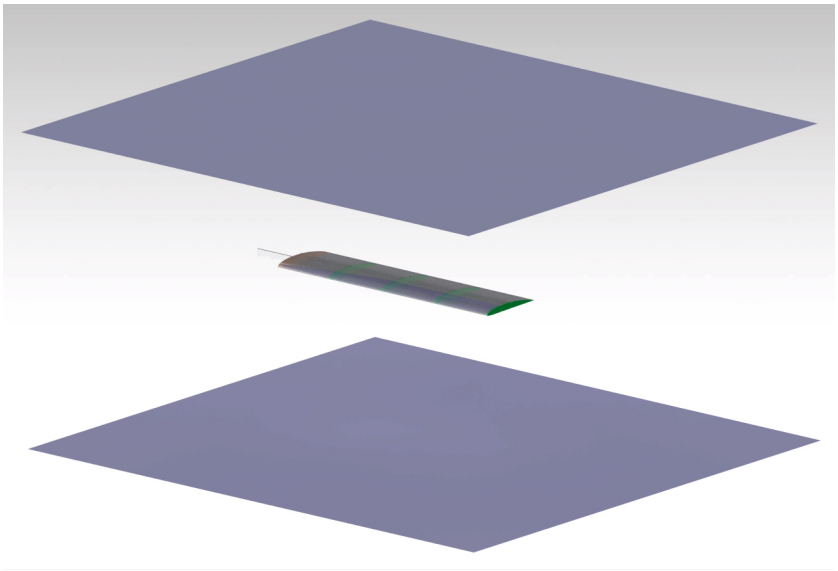

Figure 4.8: CAD model showing the wing confined by two solid walls. Each wall is separated 0.4m from the wing.

4.5.3 Wing Numerical Results

The wing is analyzed at three different angles of attack: 0°, 4° and 6°. The environment conditions and speed varies for each angle of attack. These conditions are summarized in table 4.3, for 0°, 4° and 6°. These conditions are selected to match the conditions experienced during the wind tunnel testing (which is the subject of the next chapter). Despite this, the velocity for each of the test cases is very close to 20m/s. The Reynolds numbers of the tested wing for all three cases, are also very similar.

Table 4.3: Environment and wind tunnel conditions for 0°, 4° and 6° test cases.

Parameter	0°	4°	6°
Velocity, V [m/s]	20.26	20.15	20.10
Ambient Temperature, T [°C]	24.5	22.6	24.55
Ambient Humidity, %	43.85	52.15	33.7
Ambient Pressure, P [Pa]	95431	95771	95447
Air Density, ρ [kg/m^3]	1.111	1.122	1.113
Air Dynamic Viscosity, μ [N.s/m^2]	1.880×10^{-5}	1.8705×10^{-5}	1.8805×10^{-5}
Wing Reynolds Number	179630	181251	178392

With the proposed test conditions, the wing is evaluated for each AOA. Figures 4.9, 4.10 and 4.11 show the distribution of wing deflections u, v and w and also spanwise u, v and w deflection distribution at half chord line, for each AOA.

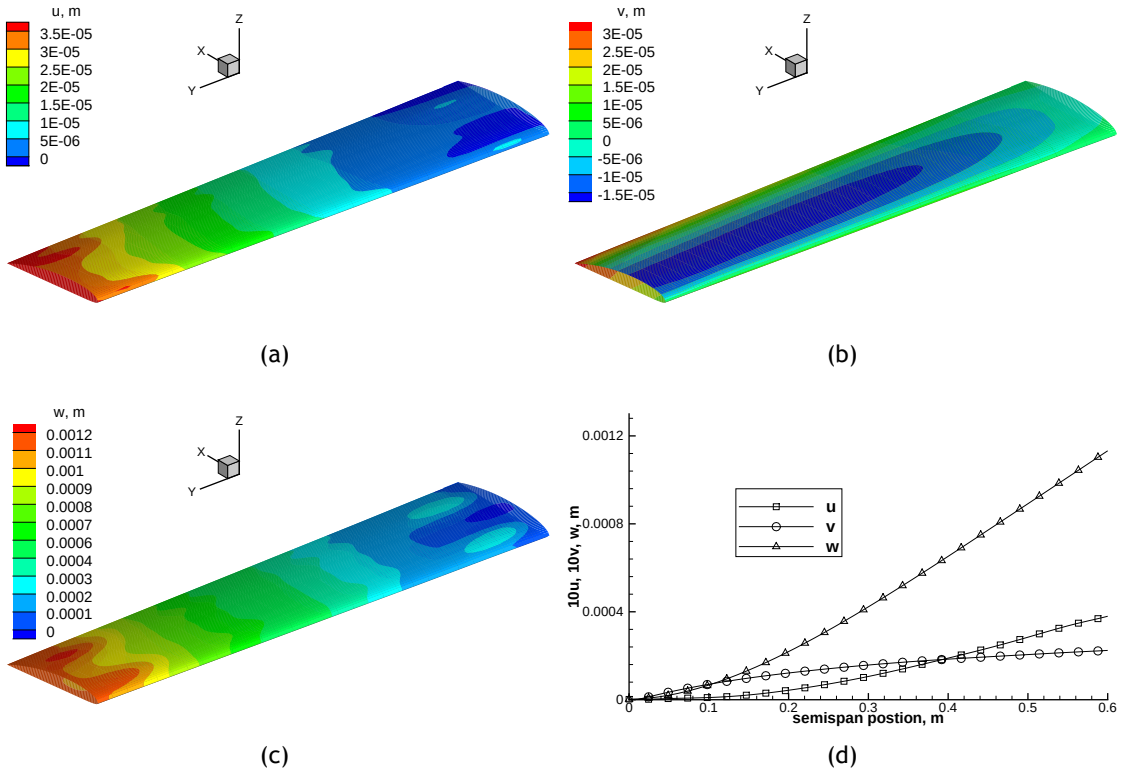

Figure 4.9: Displacements of the test wing, due to aerodynamic loading at $\alpha = 0°$, V = 20.26m/s: a) u, b) v, c) w deflection distribution and d) spanwise u, v and w deflection distribution at 50% chord line.

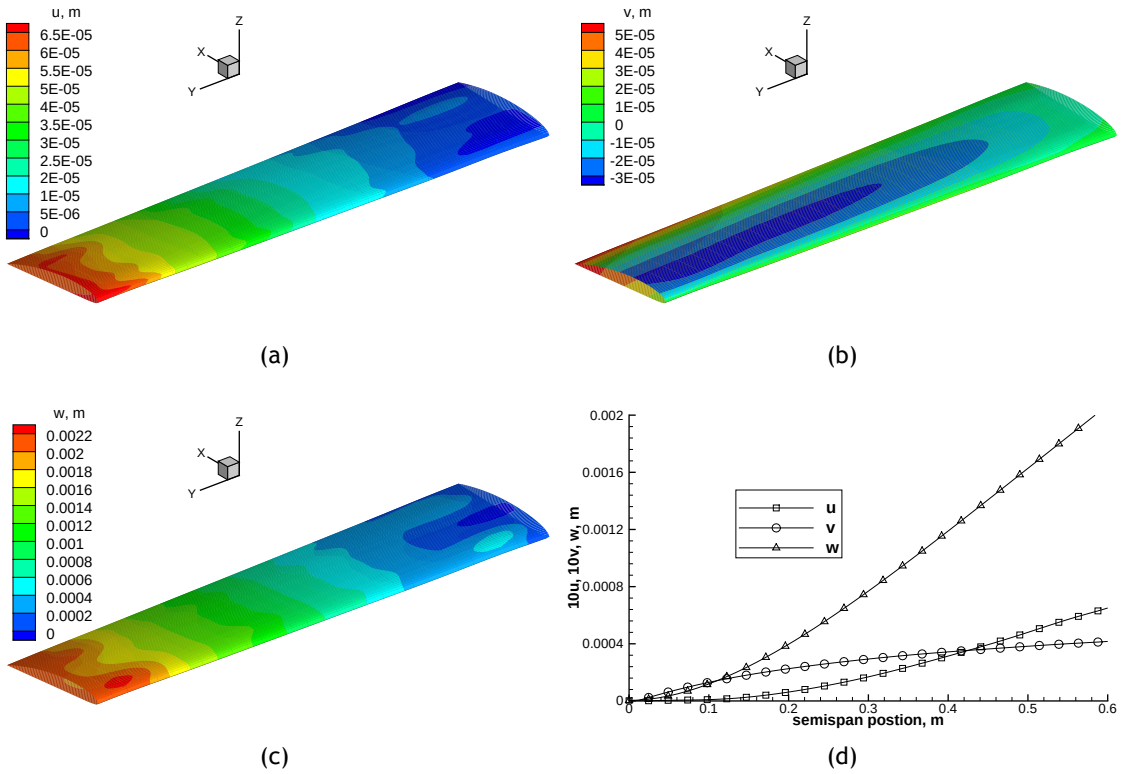

Figure 4.10: Displacements of the test wing, due to aerodynamic loading at $\alpha = 4°$, V = 20.15m/s: a) u, b) v, c) w deflection distribution and d) spanwise u, v and w deflection distribution at 50% chord line.

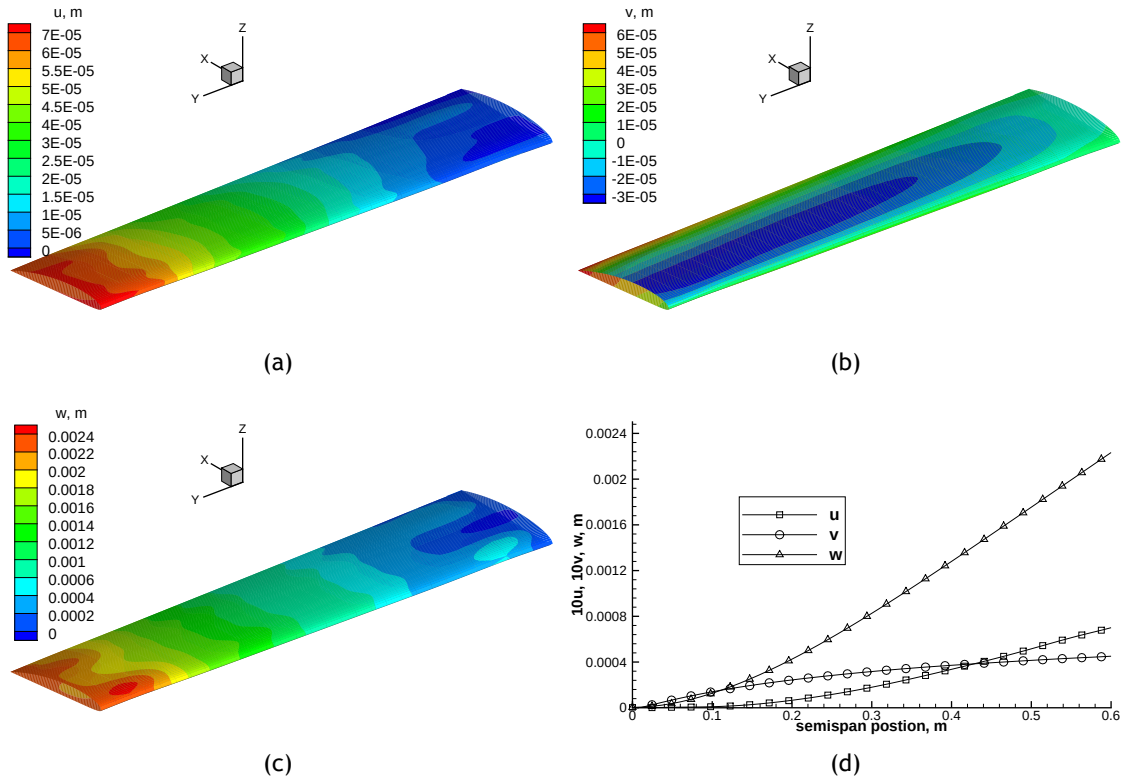

Figure 4.11: Displacements of the test wing, due to aerodynamic loading at $\alpha = 6°$, V = 20.10m/s: a) u, b) v, c) w deflection distribution and d) spanwise u, v and w deflection distribution at 50% chord line.

As expected, in all AOA's, w deflection has the higher magnitude, when compared with u and v. On the other hand, all the situations studied show an increasing vertical deformation as the distance from the wing root increases. This is an expected scenario given the fact the wing is considered to be clamped at the root and also that the wing is producing a positive lift.
In particular, considering the $\alpha = 0°$ situation, a maximum tip deflection of 1.24mm is observed (Fig.4.9(c)). As for the case of $\alpha = 4°$, the tip w deflection has increased, since the lift produced by the wing has also increased. So, the aerodynamic loads became more intense, leading to a more severe wing deformation. As a consequence, the maximum tip deflection is now 2.27mm (Fig.4.10(c)). In the last case studied, $\alpha = 6°$, this increase in tip deformation is even more notorious. In fact, the tip deflection has now grown up to 2.45mm (Fig.4.11(c)).
Observing Figs.4.9(d), 4.10(d) and 4.11(d), which present u, v and w distribution at half chord line, the similarities between the shape of the mentioned curves are visible. In fact, leaving aside the different magnitude of the curves, the deformation shape does not change dramatically for different AOA's. This is an interesting conclusion that points out that the aerodynamic forces distribution does not significantly change in shape, but change in magnitude. This conclusion is valid for small angles of attack and for AOA's greater than zero lift, since near and after stall the force distribution dramatically changes.

Chapter 5

Experimental Study

In this chapter, the main focus is on the wind tunnel testing of the wing shown in section 4.5 of this work. To accomplish this, a fully automated measurement system is developed. As seen in the referred section, the w deformation is prevalent over u and v. In fact, at least one order of magnitude separate w from u and v. Therefore, the main focus of the experiment will be to measure the deformation in the upper direction, since the other deformations are simply too small to measure in a one-dimensional experimental installation.
One other assumption that has to be taken into account when measuring the deformation is related to u and v deformations. Since undeformed and deformed wing surfaces will be taken in the same wing xy coordinates, one has to assume that deformations in x and y are small. Otherwise, these coordinates would have to be corrected by an amount equivalent to u and v. However, as seen above these corrections are very small and will be neglected in the current work.
There is also another aspect that should be considered. The EPM theory predicts the deformation in the mid surface of the wing. However, it is not feasible to measure the mid-surface deformation directly. To overcome this, the upper surface displacement will be measured. However, one has to assume that the mid-surface displacements do not significantly change at the upper surface.

5.1 The Wind Tunnel

The wind tunnel used to perform the experimental test is an open type wind tunnel from the French manufacturer EReME. It has a variable speed AC motor with a nominal power of 15kW at 970 RPM. Directly linked to the motor shaft is a sucking axial fan with 1.2m of diameter. The wind tunnel test section has a width of 800mm, a height of 800mm and a length of 1500mm. The maximum velocity inside the test section in NTP (Normal Temperature and Pressure) conditions is around 30m/s.
The settling chamber has a cross section of 2m$\times$2m and is fitted with a stainless steel Honeycomb. The diffuser has a square inlet section of 0.8m$\times$0.8m and an outlet circular section of 1.2m. Figure 5.1 shows a photograph of the wind tunnel installed in the Aerodynamics and Propulsion Laboratory of Universidade da Beira Interior.

Figure 5.1: Photograph showing the EReME wind tunnel.

5.2 The Measurement Installation

In order to build a fully automated wing deformation measuring installation, it is necessary to integrate several distinct components. Essentially, the installation is composed by two linear moving guides: one in the longitudinal direction and another in the vertical direction. The linear guides are actuated by two stepper motors. The laser measuring sensor is mounted on the vertical guide and using the moving guides it is capable of performing controlled two dimensional movements. The following subsections describe in detail the main components used to assemble the test facility.

5.2.1 Stepper Motor Control System

The stepper motors and their control system are the heart of the automation. Together, they control the linear guides, thus providing controlled and accurate movements to perform the wing deformation measuring by means of the laser sensor. All the control and power equipment is illustrated in Fig.5.2.
The aforementioned components are briefly described in the next topics:

1. Power Sources: In the current project two power sources are used. The first one rated 36V/9.7A is used to power the stepper motor drives. The second power source rated 5V/2A is used to power up the CNC motion controller;

2. Stepper motor drives: In the current application, a KL-5056D from Keling Technology Inc. [31] is used. The motor driver is fully digital and is based on the DSP control algorithm. This algorithm ensures a high level of system smoothness, providing optimum torque and nulls mid-range instability. Motor self-test and parameter auto-setup technology greatly facilitates system setup and improve system performance with different motors;

3. CNC motion controller: It is a link between computer and stepper motor drives. It generates the step/dir commands needed by the power drivers to operate the stepper motors. The motion controller uses a free USB port to communicate with the computer. Although the USB port is available in all modern computers, an inherent problem exists with the

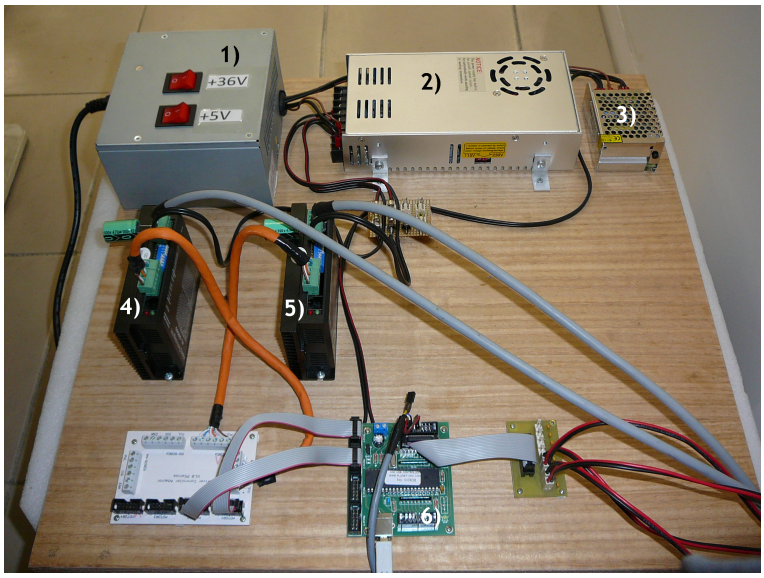

Figure 5.2: Photograph showing the electronic components needed to control the stepper motors: 1) 36V and 5V power sources switches, 2) 36V power source, 3) 5V power source, 4) longitudinal and 5) vertical direction stepper motor drives and 6) CNC motion controller.

connection, because the peripheral must share ground line with the host. Since this device is operating in a noisy environment due to the wind tunnel motor, the USB data and ground should be isolated from the host, otherwise the USB signal becomes corrupted and communication is lost. In order to accomplish this, a USB isolator [32] is used;

4. Stepper motors: In the current work two NEMA 17 size stepper motor are used. In the longitudinal linear guide, the stepper ST4118L1206 from Nanotec® is used. It has a holding torque of 0.49Nm. In the vertical linear guide the stepper ST4118M1206 also from Nanotec® is used. It has a lower holding torque than the "L", being rated 0.40Nm. Both motors can be seen in Fig.5.3(a).

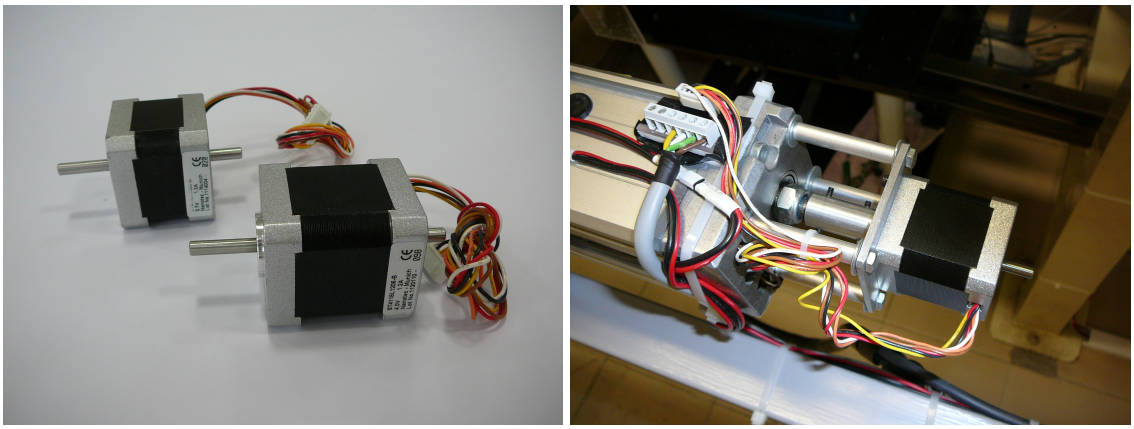

(a) Stepper motors used: ST4118M1206 on the left and ST4118L1206 on the right.

(b) ST4118L1206 connection to linear guide.

Figure 5.3: Photographs illustrating stepper motors used and the connection to the linear guide.

5.2.2 The Linear Guides

In the current experimental assembly there are two linear moving guides. They are from the manufacturer ISEL® model 400. They have an accuracy of 0.0125mm when connected to a 1.8°/step motor. Thus, a high accuracy is achieved using this linear guides. The linear guides are mounted, on the side of the wind tunnel test section, in a "T" configuration in order to allow movements in longitudinal and vertical directions. An upper additional guide is added to the system in order to improve torsional rigidity of the overall assembly.
The linear guides are supported to the side of the wind tunnel test section using a custom made metal frame. This metal frame was designed to have a reduced size, without compromising the ability to remove the lateral window of the wind tunnel test section. In Fig.5.4, it is possible to see the custom made metal frame, as well as the linear guides in its "T" configuration.

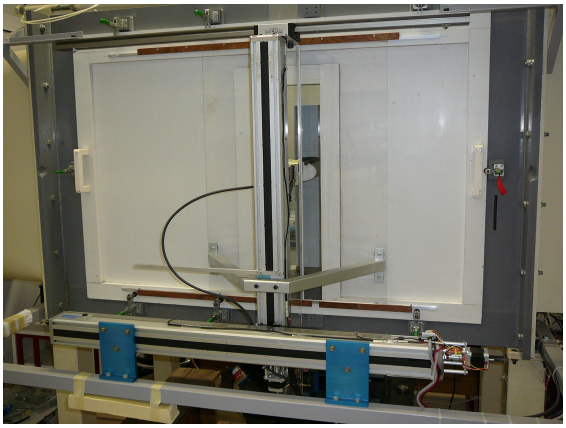

Figure 5.4: Photography showing the linear moving guides mounted in "T" configuration and the metal frame used to support the system.

5.2.3 The Laser Measuring Sensor

The laser distance measuring sensor is the key component of the experimental installation, since the vertical wing deformations are acquired by this sensor. A contactless laser sensor was chosen to measure the deformation, in order to virtually eliminate the perturbation caused by the measuring probe. The selected sensor is the Leuze® ODSL8 optical distance measuring sensor (Fig.5.5). It is a digital sensor capable of taking measurements ranging from 20mm to 400mm with a resolution smaller than 0.1mm. This particular sensor has a repeatability and an absolute measuring accuracy that depends on the measuring interval. In fact, from 20mm to 200mm, the absolute measuring accuracy and repeatability are, respectively, $\pm 1\%$ and $\pm 0.25\%$. On the other hand, from 200mm to 400mm, the absolute measuring accuracy and repeatability are, respectively, $\pm 2\%$ and $\pm 1\%$. Since a higher precision is desired, the first interval is selected.
The selected sensor uses the serial protocol to send a continuous data stream to the computer. Two serial protocols are available: RS232 and RS485. The first protocol is more commonly found in desktop computers. However, the second protocol uses a two-pair differential connection, which greatly increases noise rejection. Because of this last argument, the RS485 protocol is chosen over the RS232 to connect the sensor to the computer.
More detailed specifications are available in appendix B and reference [33].

Figure 5.5: Leuze ODSL8 optical distance measuring sensor used in the experimental validation.

The sensor is supported by a long mast made of basswood. In order to improve the bending rigidity of the mast, two unidirectional pultruded carbon-fiber inserts are added in the top and bottom sides of the mast. As referred before, to increase accuracy the sensor should be as close as possible to the target. This implies that a portion of the mast has to be inside the wind tunnel working section.

To minimize the interference caused by this, a cowl was developed using a NACA0030 airfoil. This cowl is made of expanded polystyrene foam (EPS) whose shape was cut with the hot-wire technique. A skin of fiberglass was then laminated around the foam profile. The cowl was designed to have an opening in order to accommodate the mast. Finally, a carbon-fiber cover, fixed in place with six screws, ensures the correct profile shape and secures the cowl in place. The finished mast assembly, with and without the cowl, is shown in Fig.5.6. A detailed analysis of the sensor support assembly interference in the flow-field is presented in section 5.4.

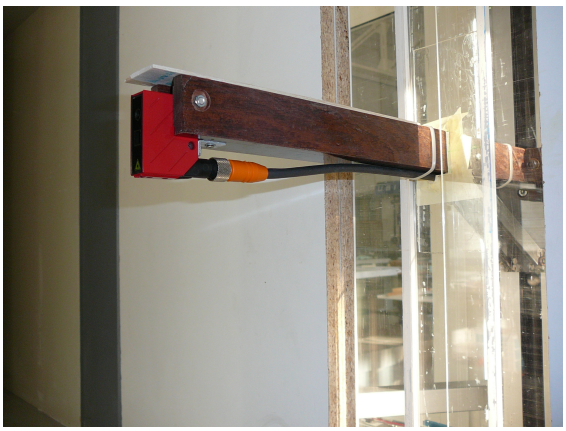

(a) Mast without the cowl, revealing the carbon-fiber inserts.

(b) Mast with the cowl, made from a NACA0030 profile.

Figure 5.6: Sensor mast with and without the streamlined cowl.

5.2.4 Double Window System

The double window plays an important role in the experimental installation. Since the linear guides are mounted on the side of the wind tunnel working section, the lateral window has a rectangular portion that was completely removed, thus allowing the sensor support to move in the longitudinal and vertical directions. This compromises the wind tunnel sealing.
The solution adopted to restore the sealing is a double window made from acrylic. This window has the particularity of being mounted in two guides: one allowing the longitudinal movement and another the vertical movement. Isolator tape has been applied in the interface between the moving window and the fixed window. As the wind tunnel velocity increases the pressure inside reduces, pressing the window against the tape and effectively making the test section airtight.

5.2.5 Complete Assembly

After describing the individual components that constitute the test assembly, Fig.5.7 shows all the components integrated.

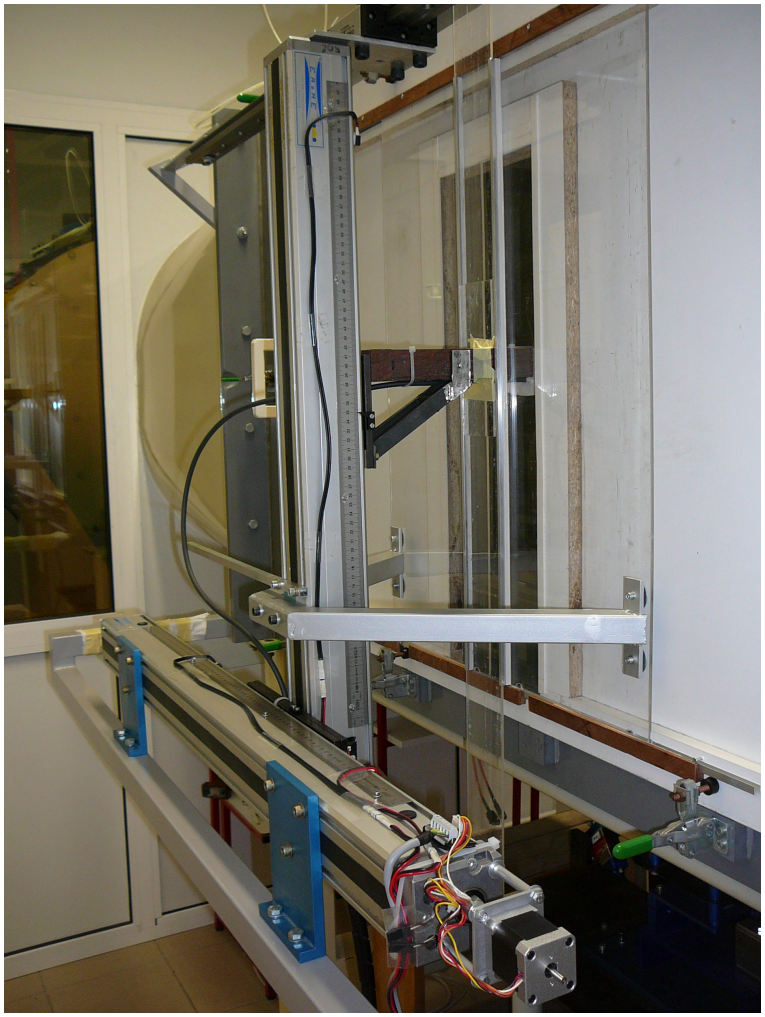

Figure 5.7: Photograph showing the complete test assembly.

5.2.6 The CNC and Sensor Acquisition software

The CNC controller has a specially designed software to work with it. The program allows the import of G-code, which is used to write the path that the measuring sensor will describe. A screenshot of CNC software during the wing acquisition path is shown in Fig.5.8.

A software was developed to read-in the computer serial port and decode the digital signal generated by the laser sensor. This program was called Sensor Acquisition Software (SAS). It is a graphical program, completely written in the C++ programming language. The graphical portion was done using GTK+ (Gimp ToolKit [28]). It is capable of displaying the measurements both in graphical and also numerical form, using a notebook-like sheet. A screenshot of SAS during a measurement procedure is visible in Fig.5.9.

In order to coordinate both programs and achieve the fully automated system, one of the CNC controller outputs is used. This is done in such a way that the sensor is only acquiring measurements when the CNC steppers are stopped. This is the desired scenario since no measurements are to be made between the preselected points.

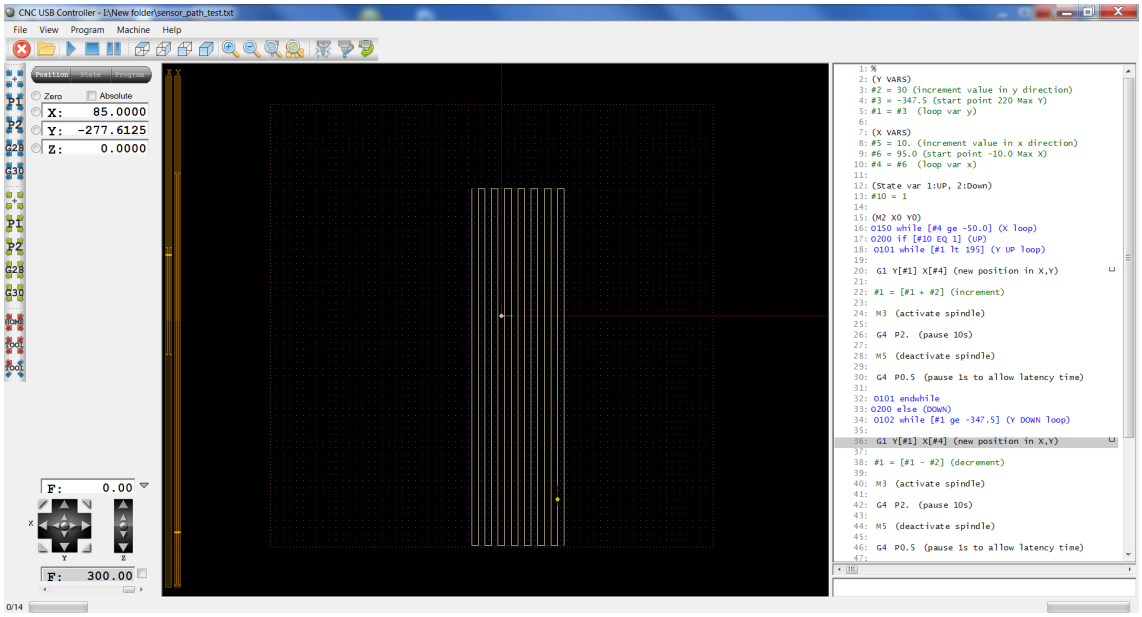

Figure 5.8: Screenshot showing the CNC controller software. At the center, the path used to acquire the deformations along the wing and at the right the respective G-code, is observed.

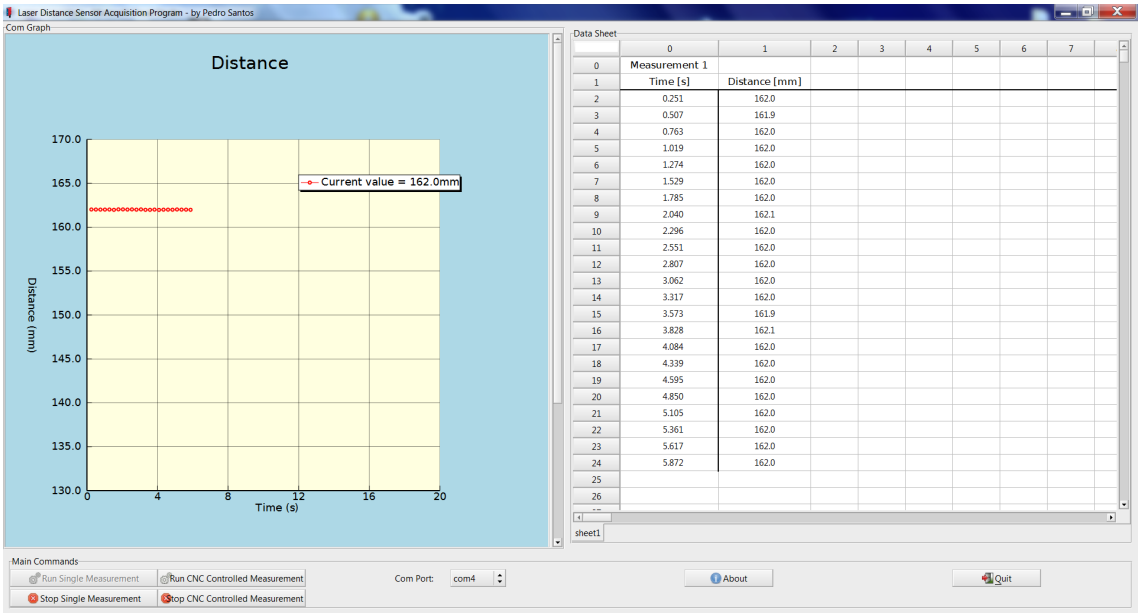

Figure 5.9: Screenshot showing the sensor acquisition software. On the left the graph view is observed and on the right the notebook view.

5.3 The Test Wing

The experimental test wing is similar to the one used in the aero-structural numerical study. Its characteristics are described in section 4.5.1 of this work. The next two subsections provide a closer look to wing construction and its installation inside the wind tunnel test section.

5.3.1 Wing Construction

The wing was built using the materials described in table 4.1 (section 4.5.1). The wing skin and spars were made from aluminum sheets. The skin and spars were conformed to the desired shape using custom made wooden molds.
All components were bonded together using high strength epoxy glue and the cure process was done at a temperature around 80°C. The temperature is crucial when curing epoxy, since the final characteristics are highly dependent on the cure temperature. Figure 5.10 shows the wing completely assembled.

5.3.2 Wing Installation Inside the Wind Tunnel

The finished wing was attached to the wing tunnel bottom by means of a plywood interface plate. This interface has two circular arc groves to secure the wing in place with bolts to the wind tunnel test section floor and to allow the adjustment of the angle of attack.
A non-structural white matted plastic film was applied to the wing's surface to enhance its reflective quality and hence the performance of the laser sensor. In fact, after some testing, it was concluded that the aluminum skin surface does not allow a correct operation of the laser sensor.
Figure 5.11 shows the wing mounted inside the wind tunnel test section with the plastic film applied.

Figure 5.10: Photograph of the actual wing used in the experimental test.

Figure 5.11: Photograph showing the wing in place for wind tunnel testing.

5.4 Sensor Support Influence on Velocity Distribution

The objective of the current section is to understand and quantify the influence of the sensor support, described in section 5.2.3. Thus, the wind-tunnel velocity profile was measured at the longitudinal plane of symmetry (xz plane). The chosen longitudinal position coincides with the center of the laser sensor mast. Three distinct configurations were measured: clean section, sensor support without cowl and sensor support with cowl. The measurements taken for these three distinct configurations can be seen in Fig.5.12 for test velocity of 20m/s.

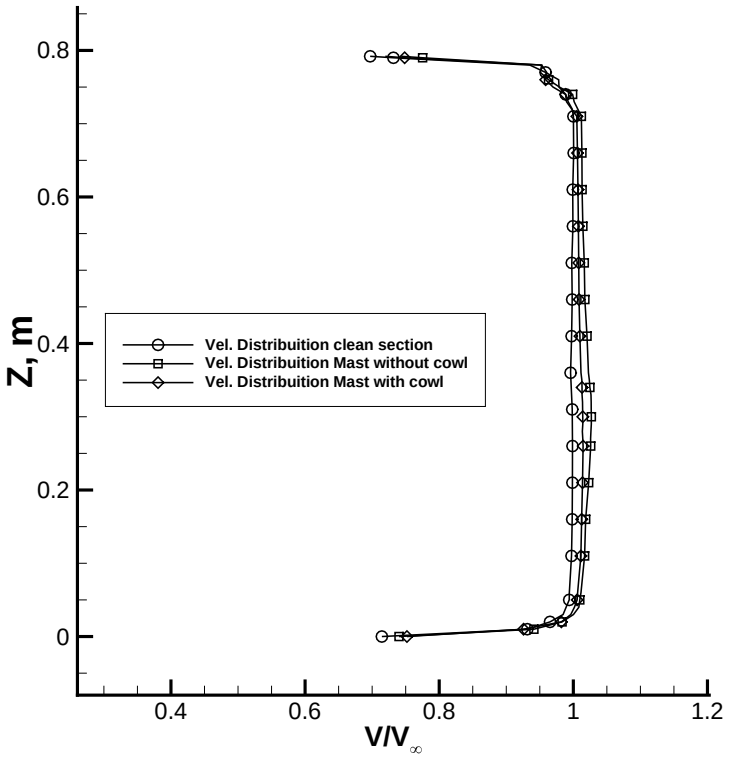

Figure 5.12: Wind tunnel velocity profile comparing the different situations studied: clean section, sensor support without cowl and sensor support with cowl. Note that sensor support is in position Z=0.31m.

Observing the figure, it is clear that the clean section presents an almost constant velocity profile outside the boundary layer.

When adding the mast without the cowl, all the velocity profile experience an increase in speed. This increase is more severe in the vicinity of the mast, as indicated by the small hump at about 0.3m above the working section floor. The maximum speed increase is around 2.7%.

As in the previous case, the velocity profile measured with the cowled mast experience an increase in magnitude. Nevertheless, this velocity increase is not so intense as in the previous case. In fact, the hump previously observed almost vanished, which indicates that the sudden flow acceleration was greatly reduced. Using the cowl, the maximum speed increase is now around 1.4%, which represents an improvement of almost 50%.

In this study, the expected benefit of the introduction of the sensor support cowling was proven. Thus, the influence of the presence of the sensor support was reduced to a minimum.

5.5 Solid and Wake Blockage Evaluation

When testing a model in a closed test section there are two main phenomena that should be considered: solid blockage and wake blockage.
The solid blockage is related to the presence of the model inside the test section and its effect in the area reduction through which the air must flow. Hence, by continuity and Bernoulli's equation, the velocity of the air increases as it flows over the model [34]. This increase in velocity, which may be considered constant over the model, is called solid blockage. The solid blockage velocity increase is defined by [34]:

$$\epsilon_{sb} = \frac{\Delta V}{V_u} \quad (5.1)$$

where V_u and ΔV are the uncorrected freestream velocity and the velocity increment due to solid blockage, respectively.
The wake blockage is related to the wake behind the model and the fact that the wake will have a mean velocity lower than the freestream. According to the law of continuity, the velocity outside the wake in a closed tunnel must be higher than the freestream velocity because a constant mass flow rate of fluid must pass through the test section. The higher velocity in the mainstream has, by Bernoulli's principle, a lowered pressure, and this lowered pressure puts the model in a pressure gradient, resulting in a velocity increment. The wake blockage is defined in a similar manner to the solid blockage. Thus, according to reference [34], the wake blockage is defined by:

$$\varepsilon_{wb} = \frac{\Delta V}{V_u} \quad (5.2)$$

where V_u and ΔV are the uncorrected freestream velocity and the velocity increment due to wake blockage, respectively.
Both solid and wake blockages contribute to increase the velocity inside the wind tunnel test section. So, the total velocity due to wake and solid blockage will be:

$$V = V_u(1 + \varepsilon_{sb} + \varepsilon_{wb}) \quad (5.3)$$

where, ε_{sb} and ε_{wb} are the solid and wake blockage corrections, respectively.
In the current work, only the velocity is to be corrected, because no aerodynamic coefficients are being measured. Thus, according to reference [34], a good approximation for total blockage is given by the following equation:

$$\varepsilon_t = \frac{1}{4}\frac{Model\ Frontal\ Area}{Area\ Test\ Section} \quad (5.4)$$

where the equation parameters are self-explanatory.
Equation 5.4 is applied to the test wing and also to the measurement sensor cowl, yielding the results presented in table 5.1. Note that the blockage ratio is the ratio of the test model frontal area to test section cross-sectional area. From table 5.1 it is possible to observe that the blockage ratio of the sensor support and the test wing is about 3.7%, well below the maximum 7.5% suggested in reference [34]. The low blockage ratio is reflected in the low value of the blockage correction. In fact, the speed increment is about 1%, a low value that will certainly favor good test results.

Table 5.1: Summary of wind-tunnel blockage elements and its respective correction.

	Test wing	Sensor Cowl	Total
Frontal area $[m^2]$	0.0095	0.0140	
ε_t	0.0037	0.0055	0.0092
Blockage ratio	0.0148	0.0219	0.0367

5.6 Experimental Test Results

As in the numerical simulations (section 4.5.3), three AOA were chosen to perform deflection measurement. These are: 0°, 4° and 6°.
The test conditions vary for each angle of attack, as summarized in Table 4.3 in section 4.5.3. Figures 5.13, 5.14 and 5.15 show the w deflection distribution along the wing and the spanwise w deflection distribution at half chord length, for each AOA.

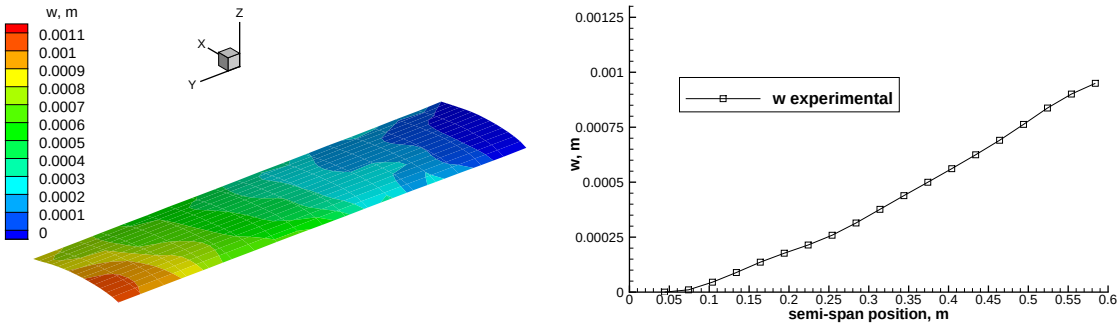

(a) (b)

Figure 5.13: Displacement of the test wing, due to aerodynamic loading at $\alpha = 0°$: a) w deflection distribution across the wing and b) spanwise w deflection distribution at half chord line.

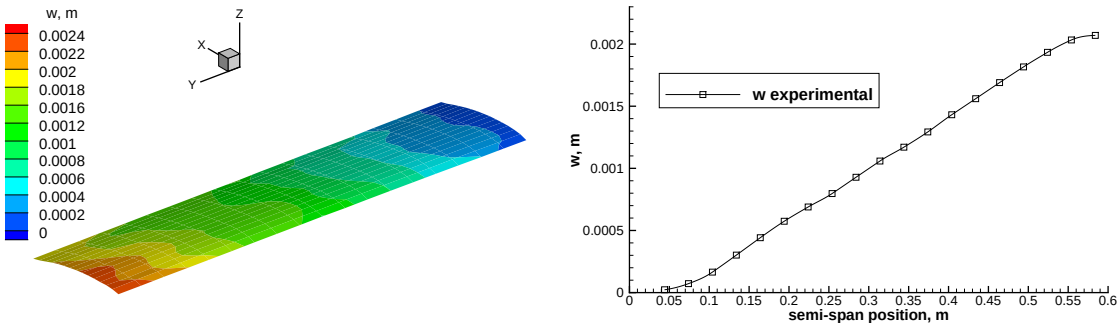

(a) (b)

Figure 5.14: Displacement of the test wing, due to aerodynamic loading at $\alpha = 4°$: a) w deflection distribution across the wing and b) spanwise w deflection distribution at half chord line.

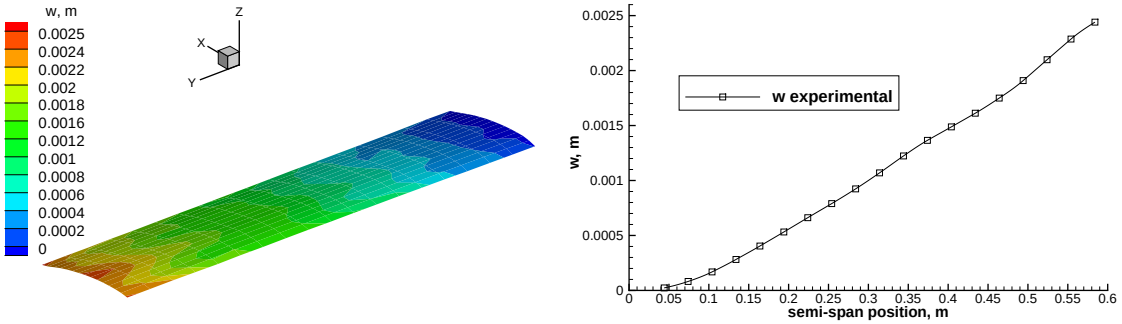

(a) (b)

Figure 5.15: Displacement of the test wing, due to aerodynamic loading at $\alpha = 6°$: a) w deflection distribution across the wing and b) spanwise w deflection distribution at half chord line.

Observing Figs.5.13, 5.14 and 5.15, it becomes immediately clear that the vertical deformation increases as the distance from the wing root is augmented. This confirms that the wing is producing a positive lift. It is also visible that near the root the deformation is close to zero, which indicates the wing is correctly clamped to the bottom of the wind tunnel test section.
Observing now the deflection distribution for $\alpha = 0°$, $\alpha = 4°$ and $\alpha = 6°$, it is clear that tip chordwise distributions are different for each case. In fact, for the first and second AOA studied, the maximum w deflection is approximately located near the leading edge. However, for the last studied angle, the maximum tip deflection moved back to a position closer to the wing tip center. Contrarily, the root chordwise distribution is very similar for all the cases studied. In fact, as said before, closer to the wing root the deformations tend to zero.
Regarding maximum tip deflection, the increase of this parameter closely follows the AOA. In fact, for $\alpha = 0°$ the tip deflection is about 1.1mm (Fig.5.13(a)). In the case $\alpha = 4°$, the tip w deflection is now 2.4mm (Fig.5.14(a)). In the last case studied, $\alpha = 6°$, this increase in tip deformation is even more notorious, being 2.5mm (Fig.5.15(a)).

Chapter 6

Comparison Between Numerical and Experimental Results

After presenting the numerical and experimental results, a comparison should be made, to assess the accuracy of the numerical results when compared against the experimental results. As said in the beginning of chapter 5, only the w deformation could be measured, given the characteristics of the laser sensor and the experimental installation. For this reason the comparison will be made only between the referred deformation. In order to favor understanding, the spanwise deformations at half chord length were superimposed for each numerical and experimental case and are shown in Fig.6.1.

Starting with the first case analyzed, $0°$, whose w deflection distribution for the numerical and experimental cases are in Figs.4.9 and 5.13, respectively, it is possible to extract some important conclusions. Observing the area in the vicinity of the wing root, small deformation variations are visible in the chordwise distribution in the numerical case. These differences are not captured in the experimental case, because, even if they existed in the experimental wing, they are simply to small to be measured with the current sensor. The same observation is valid for the region near the wing tip. In fact, the numerical results show a very complex distribution of w deformation, whereas the experimental results show a maximum deflection near the leading edge, which decays to its minimum near the trailing edge.

The displacement distribution for $\alpha = 4°$ presents a much better correlation between experimental and numerical data. In fact, the tip chordwise distribution in both numerical and experimental results shows a maximum deformation near the leading edge that decays to a minimum near the trailing edge.

Regarding the deflection distribution for $\alpha = 6°$, the experimental and numerical tip chordwise distribution differs in the maximum deflection position. In the numerical case the maximum deflection is very close to the wing tip leading edge. However, in the experimental results the maximum deflection point, retreated to a position closer to the wing tip center. This is due mainly to the sensor not being capable of capturing all the small deformation variations, resulting in a distribution that does not represent the reality very closely.

In more detail, Fig.6.1(a) shows the superimposed numerical and experimental curves of spanwise w deformation at 50% of wing chord for $0°$. In these curves, a general good agreement between the deformation growth from root to tip is clearly observed. Despite this, the aero-structural tool moderately overestimates the deformation over the entire wing, being the error near the tip (y=0.58m) around 7%. Unlike this, for the $4°$ and $6°$ cases, the numerical tool moderately underestimates the deformation over the entire wing. One other interesting aspect is that the error has grown from $\alpha = 4°$ to $\alpha = 6°$. In fact, for the former AOA, the relative error is about 9% and for the second the relative error is almost 13%. However, the absolute errors are 0.17mm and 0.29mm for $4°$ and $6°$, respectively. These values are very close to sensor resolution (especially the first case) and also sensor repeatability (both cases).

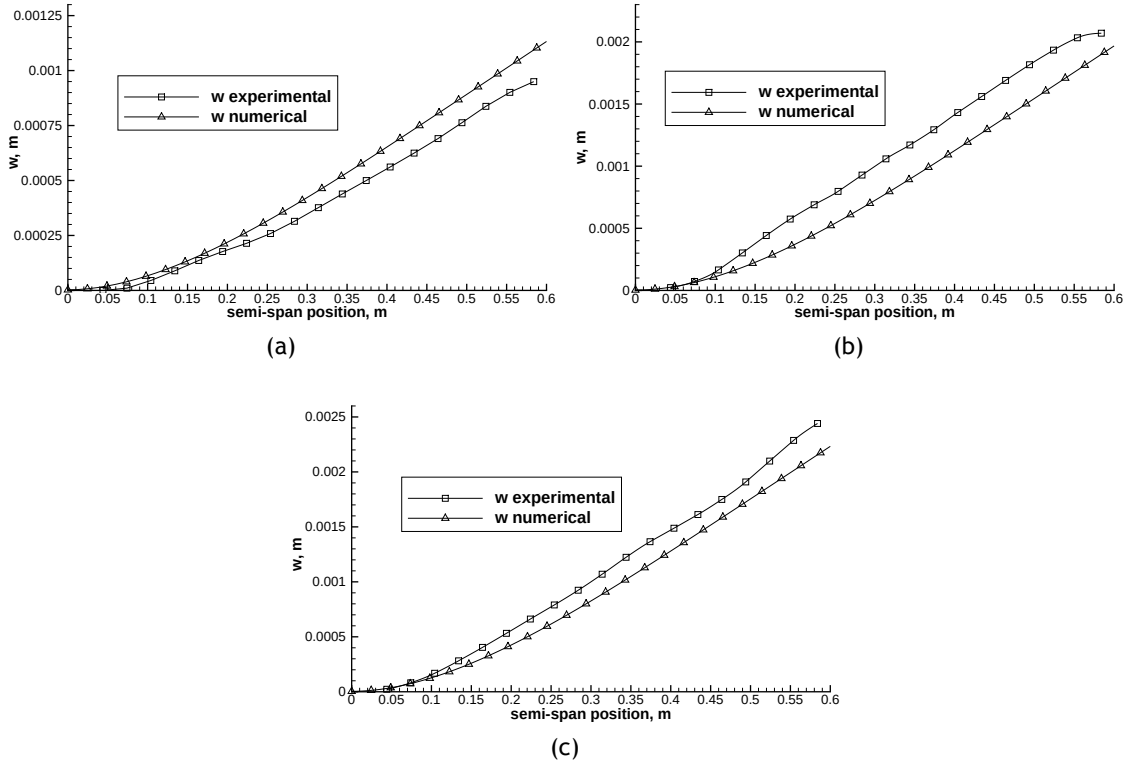

Figure 6.1: Spanwise w deflection distribution at half chord length for the experimental and numerical tests: a) 0°, b) 4° and c) 6°.

6.1 Comments on Experimental Errors

Although the laser sensor is very accurate, there are some issues related to repeatability and absolute measurement accuracy. The distance between the measuring object (wing surface) and sensor was, on average, 150mm, which is a relatively large distance. Given the manufacturer specifications, it is expected a maximum repeatability of $\pm$0.375mm and an absolute measurement accuracy of $\pm$1.5mm. Since only differential measurements were taken, the repeatability parameter is more important. Thus, given the scenario of a measurement being affected by summing 0.375mm and other subtracting the same amount, the total error would be 0.75mm. However, this is the worst possible scenario. In fact, various measurements were taken and the average repeatability was well below 0.1mm. Taking this into consideration and the analysis made in the previous section, one is lead to conclude that some of the differences verified between experimental and numerical results are very close to measurement resolution and repeatability. This is of great concern and there is no doubt that this issue should be addressed in the future, by using a sensor with higher resolution and precision. By doing this, more accurate results could be acquired, thus allowing more concrete and supported conclusions.

One other aspect that should be addressed is related with the positioning error of the linear guides. Since a stepper motor is a mechanical device that is manufactured to a certain tolerance, it has an error associated with it. The stepper motors used in this work have a tolerance of $\pm$5% non-accumulative error regarding the location of any given step. This means that after a certain number of steps, the positioning error will be within the $\pm$5% of the step resolution [35]. The stepper motors used have a resolution of 1.8°/step. So, the positioning error will be

$\pm 0.09^{\circ}$. Given the linear guide relation of 80 steps per mm, this translates in a linear movement of 0.0125mm per step and an error of ± 0.000625mm. So, one is lead to conclude that the position error is very small and could be negligible. Of course great care should be taken so that the rated torque of the system is not exceeded (nor even approached). Otherwise, the motors will loose steps, and since they are used in an open-loop system, there is no way to identify or correct missed steps, which will lead to a subsequent positioning error.

After the reflection about the positioning error, there is another source of uncertainty that should be addressed. This source of error is related to the AOA positioning. Despite great care was taken to correctly adjust the wing AOA, it is clear that associated with the analog scale, there is a parallax error due to human eye. This should be addressed in the future by creating an automatic adjustment mechanism.

One other source of error is due to the wind tunnel test section walls, the so called “reflection effect”. This effect is responsible for changing the lift of surfaces near solid walls, such as in a wind tunnel. This effect may have increased the lift produced by the wing, thus increasing the wing deformation. An attempt to numerically model this effect was made using the reflection technique. Despite this, only the potential effect of the solid walls near the wing upper and lower surfaces, was modeled. More complex viscous effects due to the boundary layer were not accounted for. So, to accurately quantify this effect, wing aerodynamic coefficients inside wind tunnel should be measured, especially the lift coefficient, in order to evaluate the lift produce by the wing. This data could then be compared with the coefficients predicated by the aerodynamic solver (VLM) and important conclusions could be drawn.

The measuring sensor support and its respective cowl also present themselves a source of experimental error. In fact, this support is likely to prevent the flow in the near vicinity to fully develop (creating a confining effect), thus effectively increasing lift locally.

All these aspects were presented individually. However, together they contribute to an overall error that is extremely hard and complex to quantify mathematically. Because of this, the error quantification should be addressed in a near future, in an effort of quantifying the above mentioned aspects as whole.

Chapter 7

Conclusions

An aerodynamic-structural solver has been developed and validated against experimental data from wind tunnel testing. The aero-structural solver uses a Vortex-Lattice Method to predict wing characteristics. The linear VLM was expanded with the decambering approach to allow the wing non-linear characteristics to be computed, using known airfoil section data. The VLM developed has been validated against experimental data, showing a very good agreement. The structural solver use a first order shear deformation theory (FSDT) equivalent plate wing modeling to predict both static deformations and modal analysis. Comparison against finite element modeling showed a good agreement for both static deformation and modal analysis.

A general good agreement between the deformation calculated with the numerical model and the data collected from wind tunnel testing was observed. Despite this, for low angles of attack, such as $\alpha = 0°$, the aero-structural tool moderately overestimates the deformation over the entire wing. On the other hand, for the other two tested AOA ($4°$ and $6°$) the numerical tool revealed a tendency to underestimate the deformation over the entire wing, with an increasing error as angle of attack increases. There is no doubt that this issue should be addressed in the future.

However, some questions had been raised about the accuracy of the laser sensor. In fact, most of the differences observed between numerical and experimental data, were close to sensor resolution and also to sensor repeatability. This poses important questions about the discrepancies observed between numerical and experimental data, since they could be closely related to sensor accuracy. In part, this aspect adds some uncertainty to the conclusions taken. Definitely, this aspect should be addressed in the near future.

After comparing numerical calculations against experimental data, it is possible to affirm that the current tool is appropriate for analyzing and designing wings in the preliminary phases of aircraft project. In fact, the tool is capable of calculating wing displacements under aerodynamic loading with adequate accuracy and with low computational resources, thus effectively allowing multiple calculations to be performed, in a short period of time. These capabilities are essential for design and optimization tasks in the preliminary phases of wing design.

One other point that favor this aero-structural tool, is related with the developed GUI, since it greatly facilitates and enhances the user experience and also the data visualization and post-processing. Thus, using the GUI, the user has a steep learning curve, becoming highly productive after a short period of time..

7.1 Future Work

As discussed throughout the work, some improvements and also some expansions could be performed to the current work. They could be broadly divided in two areas: numerical and experimental. Each of these groups will be discussed separately.

7.1.1 Numerical

From the numerical point of view, the main improvements that should be carried out are related to the structural program. In fact, in the current implementation, only a simple trapezoidal wing can be analyzed. Additionally, only isotropic materials are allowed. So, in the future the EPM should be expanded to allow more complex wing geometries, in other words, allow for compound trapezoidal planform wings. Also, the use of non-isotropic materials should be introduced in the structural model.
Regarding the aerodynamic model, an expansion to allow more complex multi-lifting surface capability, such a wing/canard configuration or a vertical tail, should be carried out.
Concerning the aero-structural tool, perhaps the most important task to be performed in the future, is to integrate the current tools in an aero-structural wing optimization and design program, thus allowing for more detailed optimizations to be carried out. This would allow for Multidisciplinary Design Optimization (MDO) to be performed.

7.1.2 Experimental

During the experimental tests some shortcomings were encountered, that should be undoubtedly addressed in future similar research work. Perhaps the major shortcoming is related with measuring laser sensor. In fact, the weakest point of the experimental installation is the laser sensor. So, a future improvement to the experimental installation would be to substitute the laser sensor with a more accurate version, or even by a contour laser to acquire a 2D profile at once. This modification to a 2D profile sensor will also allow the measuring of the u displacement. Moreover, to increase the quality of the results, two sensors could be mounted in a parallel configuration: one in the wing upper surface and other in the wing lower surface. The upper and lower deformed wing surfaces could then be averaged to approximate mid-surface deformations.
One of the flaws of the current work was the lack of lift, drag and moment coefficients of the experimental wing. So, an important future work would be to measure these coefficients and compare them with those predicted with the aero-structural tool. This would greatly improve the confidence in the experimental results. One other interesting aspect would be to validate drag results computed with the aero-structural tool for the final deflected surface.
Future work will involve improving wing construction quality, possibly using numerical machining to produce wing skin and spars. An increased construction quality will allow a bigger similarity between the numerical wing and the experimental wing.
Finally, some issues were identified related with interferences from wind tunnel test section walls. This problem could be addressed by testing the experimental wing in a wind tunnel with a bigger test section, or even with an open test section.

Bibliography

[1] J. R. R. A. Martins, "A Coupled-Adjoint Method for High-Fidelity Aero-Structural Optimization," Master's thesis, Stanford University, October 2002.

[2] J. J. Reuther, J. J. Alonso, J. R. R. A. Martins, and S. C. Smith, "A Coupled Aero-Structural Optimization Method for Complete Aircraft Configurations," in *AIAA 37th Aerospace Sciences Meeting*, pp. 99–0187, 1999.

[3] I. Tani, "A Simple Method of Calculating the Induced Velocity of a Monoplane Wing," *Aero. Res. Inst., Tokyo Imperial Univ.*, vol. 9, pp. 1115 – 1151, August 2005.

[4] R. S. Schairer, "Unsymmetrical Lift Distributions on a Stalled Monoplane Wing," Master's thesis, California Institute of Technology, 1939.

[5] W. R. Sears, "Some Recent Developments in Airfoil Theory," *Journal of The Aeronautical Sciences*, vol. 23, pp. 490 – 499, May 1956.

[6] J. B. Tseng and C. E. Lan, "Calculation of Aerodynamic Characteristics of Airplane Configurations at High Angles of Attack," tech. rep., NASA CR 4182, 1988.

[7] R. Mukherjee, *Post-Stall Prediction of Multiple-Lifting-Surface Configurations Using a Decambering Approach*. PhD thesis, North Carolina State University, Raleigh, NC, December 2004.

[8] R. Mukherjee and A. Gopalarathnam, "An Iterative Decambering Approach for Post-Stall Prediction of Wing Characteristics using known Section Data," in *41st AIAA Aerospace Sciences Meeting*, (Reno, Nevada), January 2003.

[9] F. T. Johnson, E. N. Tinoco, and N. J. Yu, "Thirty years of development and application of CFD at Boeing Commercial Airplanes, Seattle," *Computers & Fluids*, vol. 34, no. 10, pp. 1115 – 1151, 2005.

[10] R. K. Kapania and Y. Liu, "Static and Vibration Analyses of General Wing Structures using Equivalent-Plate Models," *AIAA JOURNAL*, vol. 38, pp. 1269–1277, July 2000.

[11] O. Song and L. Librescu, "Free Vibration and Aeroelastic Divergence of Aircraft Wings Modeled as Composite Thin-Walled Beams," *AIAA Paper*, vol. 91, no. 1187, 1991.

[12] U. Lee, "Equivalent Dynamic Beam-Rod Models of Aircraft Wing Structures," *Aeronautical Journal*, December 1995.

[13] J. Katz and A. Plotkin, *Low-Speed Aerodynamics*. Cambridge University Press, second ed., 2001.

[14] W. H. Press, S. A. Teukolsky, W. T. Vetterling, and B. P. Flannery, *Numerical Recipes in Fortran - The Art of Scientific Computing*. Cambridge University Press, second ed., 1992.

[15] J. Bertin, *Aerodynamics for Engineers*. Upper Saddle River, NJ: Prentice Hall, second ed., 2002.

[16] T. Melin, A. T. Isikveren, and M. I. Friswell, "Induced-Drag Compressibility Correction for Three-Dimensional Vortex-Lattice Methods," *Journal of Aircraft*, vol. 47, pp. 176–194, July-August 2010.

[17] C. Ostowary and D. Naik, "Post Stall Studies of Untwisted Varying Aspect Ratio Blades with a NACA 44XX Airfoil Section - Part II," *Wind Engeneering*, vol. 9, no. 3, pp. 149–164, 1985.

[18] J. C. Sivells, "Experimental and Calculated Characteristics of Three Wings of NACA 64-210 and 65-210 Airfoil Sections with and without 2° Washout," tech. rep., Langley Memorial Aeronautical Laboratory, December 1947.

[19] I. H. Abbott, A. E. Yondoenhoff, and J. Louis S. Stiyers, "Summary of Airfoil Data," tech. rep., Langley Memorial Aeronautical Laboratory, 1945.

[20] F. Melo, "Projecto Estrutural de Asas usando a Teoria da Placa-Equivalente," Master's thesis, Universidade da Beira Interior, Covilhã, August 2008.

[21] R. Gabriel, "Development of Equivalent Plate Models for Aircraft Wing Structures," Master's thesis, Universidade Tecnica de Lisboa, October 2007.

[22] K. Karamcheti, *Principles of Ideal Fluid Aerodynamics*. Krieger, Malabar, FL, first ed., 1980.

[23] P. W. Jansen, "Aerostructural Optimization of Non-Planar Lifting Surfaces," Master's thesis, University of Toronto, 2009.

[24] T. H. G. Megson, *Aircraft Structures for Engineering Students*. Butterworth-Heinemann, forth ed., 2007.

[25] D. J. Martin, "Summary of Flutter Experiences as a Guide to the Preliminary Design of Lifting Surfaces on Missiles, NACA TN 4197," tech. rep., Langley Aeronautical Laboratory, Langley Field, VA, February 1958.

[26] M. Drela, *MXFOIL 6.94 User Guide*. Massachusetts Institute of Technology & Astro Harold Youngren Aerocraft, Inc., December 2001.

[27] P. V. Gamboa, *Multidisciplinary Design Optimization of Morphing Aircraft*. PhD thesis, Departamento de Ciências Aeroespaciais, Universidade da Beira Interior, December 2007.

[28] "The gimp toolkit." `http://www.gtk.org`. Accessed October 6, 2011.

[29] AIREX®, "Airex® C70 Universal Structural Foam." `http://www.corematerials.3acomposites.com/airex-c70.html`. Accessed September 7, 2011.

[30] *Metals Handbook, Vol.2 - Properties and Selection: Nonferrous Alloys and Special-Purpose Materials*. ASM International, tenth ed., 1990.

[31] K. T. Inc., "Keling inc. kl-5056d." `http://www.kelinginc.net/KL-5056D.pdf`. Accessed October 5, 2011.

[32] Circuits@home, "Circuits@home USB Isolator." `http://www.circuitsathome.com/measurements/usb-isolator`. Accessed October 5, 2011.

[33] Leuze®, "Leuze® ODSL8 Optical laser distance sensors." `http://www.leuze.de/downloads/los/db/28_brods/ods_15gb.pdf`. Accessed September 30, 2011.

[34] J. William H. Rae and A. Pope, *Low-Speed Wind Tunnel Testing*. John Wiley & Sons, second ed., 1984.

[35] V. V. Athani, *Stepper Motors: Fundamentals, Applications and Design*. New Age International, first ed., 2005.

Appendix A

The Vortex Ring

A.1 Velocity Induced by a Straight Vortex Segment

The Biot-Savart law in differential form is [13]:

$$\Delta \mathbf{q} = \frac{\Gamma}{4\pi} \frac{d\mathbf{l} \times (\mathbf{r}_0 - \mathbf{r}_1)}{|\mathbf{r}_0 - \mathbf{r}_1|^3} \quad \text{(A.1)}$$

The velocity induced by a straight vortex segment will be derived, based on the Biot-Savart law.

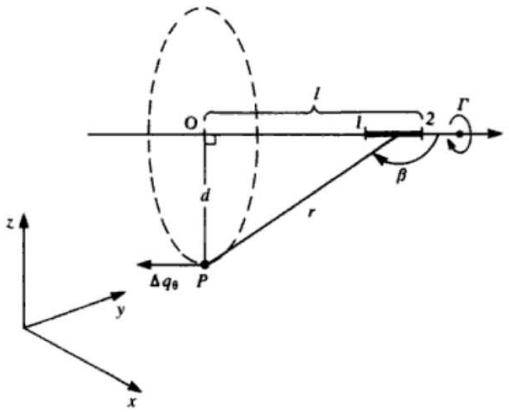

Figure A.1: Velocity induced by a straight vortex segment.

According to Biot-Savart law (Eq. (A.1)) the velocity induced by a segment $d\mathbf{l}$ on this line, at a generic point P, is:

$$\Delta \mathbf{q} = \frac{\Gamma}{4\pi} \frac{d\mathbf{l} \times \mathbf{r}}{r^3} \quad \text{(A.2)}$$

This may be rewritten in scalar form as

$$\Delta q_\theta = \frac{\Gamma}{4\pi} \frac{\sin\beta}{r^2} dl \quad \text{(A.3)}$$

From Fig.A.1 it is possible to deduce that:

$$d = r\sin\beta \text{ and } \tan(\pi - \beta) = \frac{d}{l}$$

and therefore:

$$l = \frac{-d}{\tan\beta} \text{ and } dl = \frac{d}{\sin^2\beta} d\beta$$

Substituting these expressions into Eq.(A.3), we conclude

$$\Delta q_\theta = \frac{\Gamma}{4\pi d} \sin\beta d\beta$$

Integrating this equation over a section $(1 \rightarrow 2)$ of a straight vortex segment shown in Fig. A.2:

$$\Delta(q)_{\theta_{1,2}} = \frac{\Gamma}{4\pi d} \int_{\beta_1}^{\beta_2} \sin\beta d\beta = \frac{\Gamma}{4\pi d}(\cos\beta_1 - \cos\beta_2) \quad \textbf{(A.4)}$$

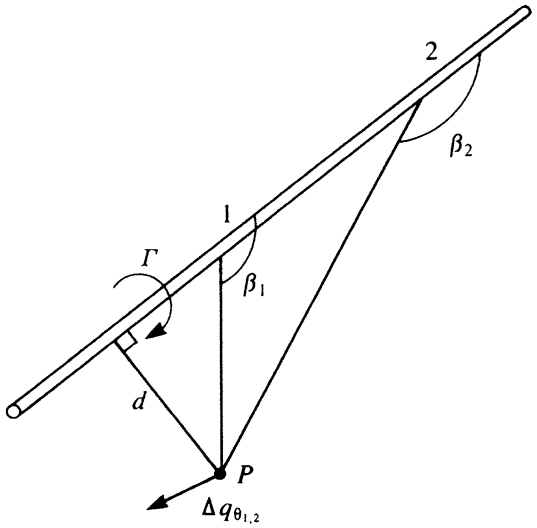

Figure A.2: Definition of the view angles used for the vortex-induced velocity calculation.

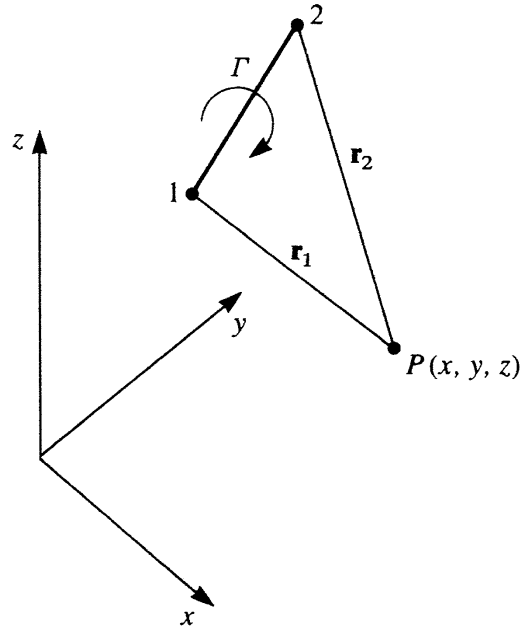

Figure A.3: Nomeclature used for the velocity induced by a tree-dimensional straight vortex segment.

The Eq.(A.4) could be modified to a form more convenient for numerical calculations, using the definitions from Fig.A.2 and A.3. For the general tree-dimensional case the two edges of the vortex segment will be located by $\mathbf{r}_1$ and $\mathbf{r}_2$. The connector vector is therefore:

$$\mathbf{r}_0 = \mathbf{r}_1 - \mathbf{r}_2$$

From Fig. A.3, the distance d and the cossines of angles β are:

$$d = \frac{|\mathbf{r}_1 \times \mathbf{r}_2|}{|\mathbf{r}_0|}$$

$$\cos\beta_1 = \frac{\mathbf{r}_0 \cdot \mathbf{r}_1}{|\mathbf{r}_0||\mathbf{r}_1|}$$

$$\cos\beta_2 = \frac{\mathbf{r}_0 \cdot \mathbf{r}_2}{|\mathbf{r}_0||\mathbf{r}_2|}$$

The direction of the velocity $q_{1,2}$ is normal to the plane created by point P and vortex edges 1,2 and is given by:

$$\frac{\mathbf{r}_1 \times \mathbf{r}_2}{|\mathbf{r}_1 \times \mathbf{r}_2|}$$

Now substituting the above mentioned expressions in Eq. (A.4), one obtain:

$$q_{1,2} = \frac{\Gamma}{4\pi} \frac{|\mathbf{r}_0|}{|\mathbf{r}_1 \times \mathbf{r}_2|} \left(\frac{\mathbf{r}_0 \cdot \mathbf{r}_1}{|\mathbf{r}_0||\mathbf{r}_1|} - \frac{\mathbf{r}_0 \cdot \mathbf{r}_2}{|\mathbf{r}_0||\mathbf{r}_2|} \right) \frac{\mathbf{r}_1 \times \mathbf{r}_2}{|\mathbf{r}_1 \times \mathbf{r}_2|}$$

After simplification becomes:

$$q_{1,2} = \frac{\Gamma}{4\pi} \frac{\mathbf{r}_1 \times \mathbf{r}_2}{|\mathbf{r}_1 \times \mathbf{r}_2|^2} \mathbf{r}_0 \left(\frac{\mathbf{r}_1}{r_1} - \frac{\mathbf{r}_2}{r_2} \right) \quad \text{(A.5)}$$

A.2 The Vortex Ring element

Based on the straight vortex segment, the vortex ring element could be defined, by superimposing the contributions of the four different straight vortex segments that form the vortex ring (see Fig.A.4). Doing this, it is possible to calculate the total induced velocity at any arbitrary point.
So, the net contribution is:

$$(u_a, v_a, w_a) = (u_{1a}, v_{1a}, w_{1a}) + (u_{2a}, v_{2a}, w_{2a}) + (u_{3a}, v_{3a}, w_{3a}) + (u_{4a}, v_{4a}, w_{4a}) \quad \text{(A.6)}$$

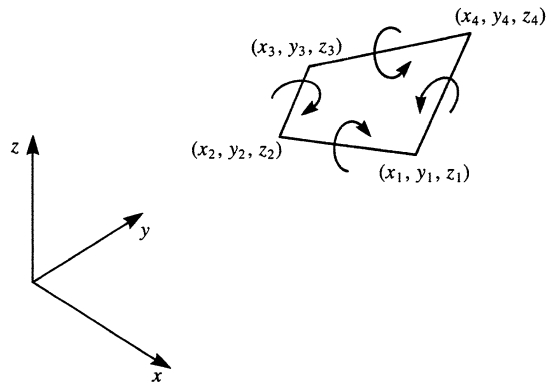

Figure A.4: The vortex ring element [13].

Appendix B

Leuze ODSL8 Optical laser distance sensor specifications

Table B.1: Laser sensor specifications (from ref [33]).

Optical Data	
Measurement Range	$20...400mm$
Resolution	$\leq 0.1mm$
Light Source	laser
Wavelength	$650nm$ (visible red light)
Light spot	divergent, $1 \times 6mm^2$ at $400mm$
Error limits (relative to measurement distance)	
Absolute measurement accuracy	$\pm 1\%$ up to $200mm / \pm 2\% 200...400mm$
Repeatability	$\pm 0.25\%$ up to $200mm / \pm 1\% 200...400mm$
Timing	
Measurement time	$2...5ms$
Response time	$\leq 15ms$
Delay before start-up	$\leq 300ms$
Electrical Data	
Operating voltage U_B	$10...30VDC$
Residual ripple	$\leq 15\%$ of U_B
Open circuit current	$\leq 50mA$
Switching output	PNP transistor, high active
Signal voltage high/low	$\geq U_B$ - 2V / $\leq$ 2V
Digital output - RS232	9600 Baud
- RS485	9600 Baud no termination
Transmission Protocol	2 byte transmission, continuous data flow
Mechanical Data	
Housing	metal
Optics cover	glass
Weight	70g
Connection type	M12 connector, 8-pin, turning

Appendix C

Paper Accepted for ICEUBI2011

P. Santos and P. Gamboa, “Development and Validation of an Aero-Structural Wing Analysis Tool”, ICEUBI 2011 - International Conference on Engineering UBI2011, 28-30 November 2011, Covilhã, Portugal.

ICEUBI2011
International Conference on Engineering UBI2011
Innovation & Development

Development and Validation of an Aero-Structural Wing Analysis Tool

Santos, P., Gamboa, P.
Departamento de Ciências Aeroespaciais, Universidade da Beira Interior, Covilhã, Portugal
p_daniel_santos@hotmail.com, pgamboa@ubi.pt

Aeronautics and Astronautics – CT 02

Abstract

The present work describes the integration of a non-linear Vortex Lattice Method (VLM) aerodynamic solver and an Equivalent Plate Model (EPM) structural solver, culminating in an Aero-Structural tool capable of analyzing wings. The aerodynamic and structural tools used in the Aero-Structural solver are described and validated, using experimental and numerical data. The aerodynamic model is expanded with the decambering approach, in order to allow for non-linear wing characteristics to be computed. This solver showed good agreement with experimental data both in linear and in non-linear regimes. The structural solver revealed good agreement with Finite-Element calculations, in both static load deformation and modal analysis. After describing and validating the two disciplines, the coupling between aerodynamic and structural solvers is described. A rectangular wing composed of skins, spars and ribs is analyzed using the present Aero-Structural solver. Conclusions are taken about convergence time and computational requirements.

Key Words: Vortex Lattice Method (VLM), Equivalent Plate Theory (EPM), Aero-Structural Analysis

Nomenclature

c	=	wing/airfoil chord
C_l	=	airfoil lift coefficient
C_d	=	airfoil drag coefficient
C_m	=	airfoil pitching moment coefficient about the quarter chord
$C_{l,max}$	=	maximum airfoil lift coefficient
C_L	=	wing lift coefficient
C_D	=	wing drag coefficient
C_M	=	wing pitching moment coefficient
F	=	residual vector
f	=	element of residual vector
i, j	=	index of wing section
J	=	Jacobian matrix
N	=	number of wing sections
m	=	total number of vortex rings
CFD	=	Computational Fluid Dynamics
VLM	=	Vortex Lattice Method
EPM	=	Equivalent Plate Model
FEM	=	Finite Element Model
x_2	=	chordwise starts location of the second decambering function
α	=	angle of attack
β	=	angle of yaw
Γ	=	strength of bound vortex
$\mathbf{n}$	=	normal vector
$\mathbf{v}$	=	velocity vector
Φ	=	velocity potential
δ_x	=	vector containing the corrections to the Newton variables
$\delta_1(x)$	=	first decambering function
$\delta_2(x)$	=	second decambering function
$\theta_2(x)$	=	angular coordinate corresponding to x_2
$U_\infty, V_\infty, W_\infty$	=	velocity components of the free-stream flow
u, v, w	=	wing deflections in x, y and z axis

Subscripts

max	=	maximum
sec	=	represents value for a wing section
$visc$	=	represents value from two-dimensional viscous experimental or computational data

I. Introduction

Aero-structural design is an active development topic that presents several challenges. In this design approach, aerodynamic and structural disciplines are coupled, making it possible to determine wing deformation under the aerodynamic loads. Traditionally, aero-structural design has been performed in a cut-and-try basis: aerodynamicists have an idea of the shape of an "optimal" load distribution and then tailor the jig shape of the structure so that the deflected wing shape under a 1-g load gives the desired load distribution [1]. This approach may be adequate up to a certain level for conventional transport aircraft, where considerable accumulated experience exists. In the case of either new planform concepts or new flight regimes, however, the lack of experience combined with the complexities of aero-structural interactions can lead to designs that are far from optimal.

Since two distinct design disciplines are used, they should be carefully selected taking in account the desired application. In fact, the level of fidelity of the chosen aerodynamic and structural disciplines is of utmost importance and should be carefully chosen according to the design requirements.

On one hand, high-fidelity computational fluid dynamics (CFD) techniques provide reliable results in aerodynamic predictions. However, these techniques require large computing resources and significant time even for the analysis at a single angle of attack. They also need the generation of high-quality grids for each configuration, which are time consuming and difficult to automate. On the other hand, low fidelity aerodynamic models need low computational resources, yet providing enough accuracy for the initial stages of wing design. Since it is of interest to have low computational cost, a Vortex-Lattice Method (VLM) is chosen to perform the aerodynamic calculation in the present work. In an effort to predict wing aerodynamic characteristics at both linear and non-linear regime, the iterative decambering scheme suggested by Mukherjee and Gopalarathnam [2,3] is introduced into the VLM. In the decambering approach, the chordwise camber distribution at each section of the wing is reduced to take the viscous effects into consideration at high angles of attack.

In structural analysis, the finite element method (FEM) has proven to be a numerical procedure that provides reliable and accurate results. The finite element method discretizes the structure into one or more types of basic structural components — the finite elements. However, the computational cost and the need to discretize the structure make this method impractical. In view of this situation, Equivalent Plate Models (EPM) arises as a compromise to simulate complex structures for the purpose of obtaining solutions in the early design stages. This idea is reasonable as long as the complex structure behaves physically in a close manner to the continuum model used and only global quantities of the response are of concern [4]. Given the nature of the aero-structural tool that is being developed, the EPM is the natural choice, since the low computational resources are a requisite.

II. Aerodynamics Solver

Steady State Vortex Lattice Method

The derivation of the theory behind the vortex lattice method presented here mainly follows reference [5]. In this formulation, vortex rings are used to discretize the three-dimensional thin lifting surface. The main reason to use these elements over the horseshoe vortex, is essentially related to the low computationally requirements. Also, the zero-normal-flow boundary condition is satisfied on the actual lifting surface which may have camber and different planform shapes. In the current work unsteady analysis is not implemented.

The constitutive elements of the thin surface are the vortex rings, (see Fig. 1a), which are fundamentally composed of four straight vortex segments.

The method by which the thin wing planform is divided into panels is shown in Fig. 1b. In each panel a vortex ring is placed, building the vortex lattice. The leading segment of the vortex ring is placed on panel's quarter chord line and the collocation point is at the centre of the three-quarter chord line. The panel normal vector is also defined at this point.

A positive Γ is defined according to the right-hand rotation rule. In VLM the singularities are placed on the mean surface of the wing, rather than on the actual surface. This distribution of vorticity seeks to emulate the changes in velocity induced on the flow as it traverses the upper and lower surfaces of the wing.

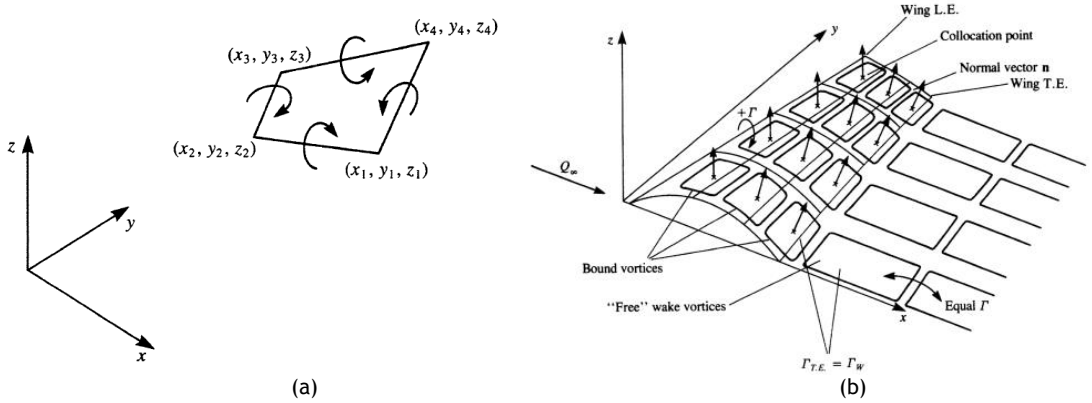

Figure 1 – Vortex Lattice Method: a) vortex ring element notation and coordinate system and b) vortex ring model for a thin lifting surface [5].

Regarding the boundary condition for solving the Laplace's equation, it is possible to conclude that only the zero normal flow across the wing surface (impermeability condition) has to be applied. Hence:

$$\nabla(\Phi + \Phi_\infty) \cdot \mathbf{n} = 0 \tag{1}$$

The influence coefficients can be calculated, computing the by-product of the induced velocity of a particular vortex ring and the lattice normal vector. The calculated induced velocity is due to unity strength vortex. Because symmetry is invoked (the distribution of circulation, Γ, is symmetric), the system only has m equations rather than $2m$.

In order to form the right-hand-side of the linear system of equations, the normal velocity components of the free-stream flow should be computed. Hence:

$$\mathrm{RHS} = -\mathrm{Q}_\infty \cdot \mathbf{n}_\mathrm{i} = -(\mathrm{U}_\infty, \mathrm{V}_\infty, \mathrm{W}_\infty) \cdot \mathbf{n}_i \tag{2}$$

Once the computation of the influence coefficients and right-hand-side vector is done, the zero normal flow boundary condition, represented by Eq. (1), results in the following system of linear equations:

$$\begin{pmatrix} a_{11} & \cdots & a_{1m} \\ \vdots & \ddots & \vdots \\ a_{m1} & \cdots & a_{mm} \end{pmatrix} \begin{pmatrix} \Gamma_1 \\ \vdots \\ \Gamma_m \end{pmatrix} = \begin{pmatrix} RHS_1 \\ \vdots \\ RHS_m \end{pmatrix} \tag{3}$$

where m denotes the total number of vortex rings.

More details on the numerical method are found in reference [5].

Iterative Decambering Approach

The following section has been adapted from references [2,3]. The decambering for an airfoil is computed using a function of two variables δ_1 and δ_2. These two variables are used because the decambering is determined using the difference between the viscous and the potential-flow results (ΔC_l and ΔC_m). The viscous C_l and C_m of the airfoil can be obtained from experimental or computational data and the corresponding potential flow C_l and C_m are calculated using the linear VLM:

$$C_l = (C_l)_{visc} - (C_l)_{potential} \; and \; C_m = (C_m)_{visc} - (C_m)_{potential} \tag{4}$$

The values of δ_2 and δ_1, in radians, for a given ΔC_l and ΔC_m are found to be given by:

$$\delta_2 = \frac{\Delta C_m}{\frac{1}{4}\sin 2\theta_2 - \frac{1}{2}\sin\theta_2} \tag{5}$$

$$\delta_1 = \frac{\Delta C_l - [2(\pi - \delta_2) + 2sin\theta_2]\delta_2}{2\pi} \tag{6}$$

$$\theta_2 = \text{acos}(1 - 2x_2/c) \tag{7}$$

In a three-dimensional analysis, the lifting surface is divided into several spanwise and chordwise panels. Unlike in the two-dimensional case, changing a δ on one section is likely to have a significant effect on the neighboring sections of the lifting surface in the three-dimensional case. To take these effects into consideration, a 2N-dimensional Newton iteration is used to calculate $\delta_1$and δ_2 at each of the N sections of the wing. Newton iteration is repeated until the ΔC_l and ΔC_m at these sections are close to zero. A $2\text{N} \times 2\text{N}$ matrix equation must be solved for each step of the Newton iteration [6] as shown in Eq. (8):

$$\text{J} \cdot \delta\text{x} = -\text{F} \tag{8}$$

where F is a 2N-dimensional vector containing the residuals of the functions f_i to be zeroed, δx is the 2N-dimensional vector containing the corrections required to the 2N variables x_i to bring the vector F closer to zero, and J is the $2\text{N} \times 2\text{N}$ Jacobian of the system containing the gradient information.

For each step of the iteration, F and J are determined, and δx is computed using Eq. (8). The corrections are then applied to the variables to bring the residuals closer to zero. In the current approach, the residual functions f were the values of ΔC_l and ΔC_m for each of the wing sections, and the variables x were the values of δ_1 and δ_2 for each of the sections. Further details about the decambering approach may be found in references [2,3].

Validation

In order to evaluate the accuracy of the non-linear VLM implementation, tests were carried out for a trapezoidal wing with 3° of dihedral and an aspect ratio of 9. In particular, experimental two-dimensional data for a NACA 65-210 airfoil at Reynolds numbers of 4.4 million [7] is used as input to generate results for trapezoidal wings without washout and with 2° washout. The planform of the tested trapezoidal wing is shown in Fig. 2.

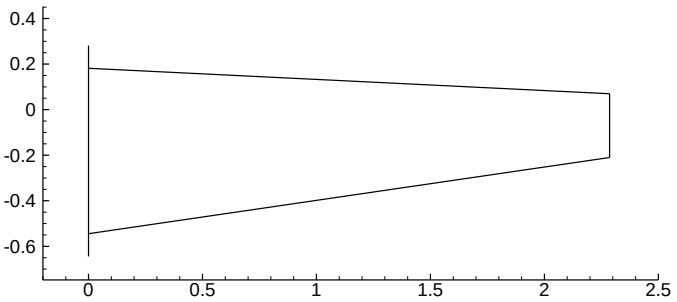

Figure 2 – Two-dimensional plot of the trapezoidal wing used in the aerodynamic solver validation tests.

Results from the iterative decambering approach are then compared with experimental $C_L - \alpha$ and $C_D - C_L$ curves for the corresponding wings from the experimental data of Sivells [8].

Figure 3a shows the two dimensional $C_l - \alpha$ curve, three-dimensional $C_L - \alpha$ curve calculated with 3D VLM and also the experimental $C_L - \alpha$ curve, for the wing without washout. Comparing the calculated and experimental lift-curve slopes, it is possible to observe a very good agreement between the referred curves. In fact, $C_{L,max}$ is predicted within 3% error and the lift-curve slope ($dC_L/d\alpha$) is estimated with an error below 1%. The

post-stall prediction with 3D VLM reveals the same tendency as in the experimental data. However, there is not sufficient experimental data to corroborate this statement.

Figure 3b shows the two dimensional $C_d - C_l$ curve, three-dimensional $C_D - C_L$ curve calculated with 3D VLM and also the experimental $C_D - C_L$ curve, for the wing without washout. Again, a very good agreement is seen between experimental data and 3D VLM data. Thus, C_{D0} and $C_{D,min}$ are predicted with accuracy.

Figure 3c shows the equivalent curves as in Fig. 3a, but for the wing with 2° washout. Again, a very good agreement between the referred curves is observed. In fact, $C_{L,max}$ is predicted with an even tighter margin, being the error inferior to 2%. The $dC_L/d\alpha$ is also estimated with accuracy. On the other hand, the post-stall prediction with 3D VLM reveals a smooth lift coefficient decrease that contradicts the abrupt stall shown in the experimental curve. However, the lack of sufficient post-stall measurements invalidates a conclusion to be taken on its accuracy.

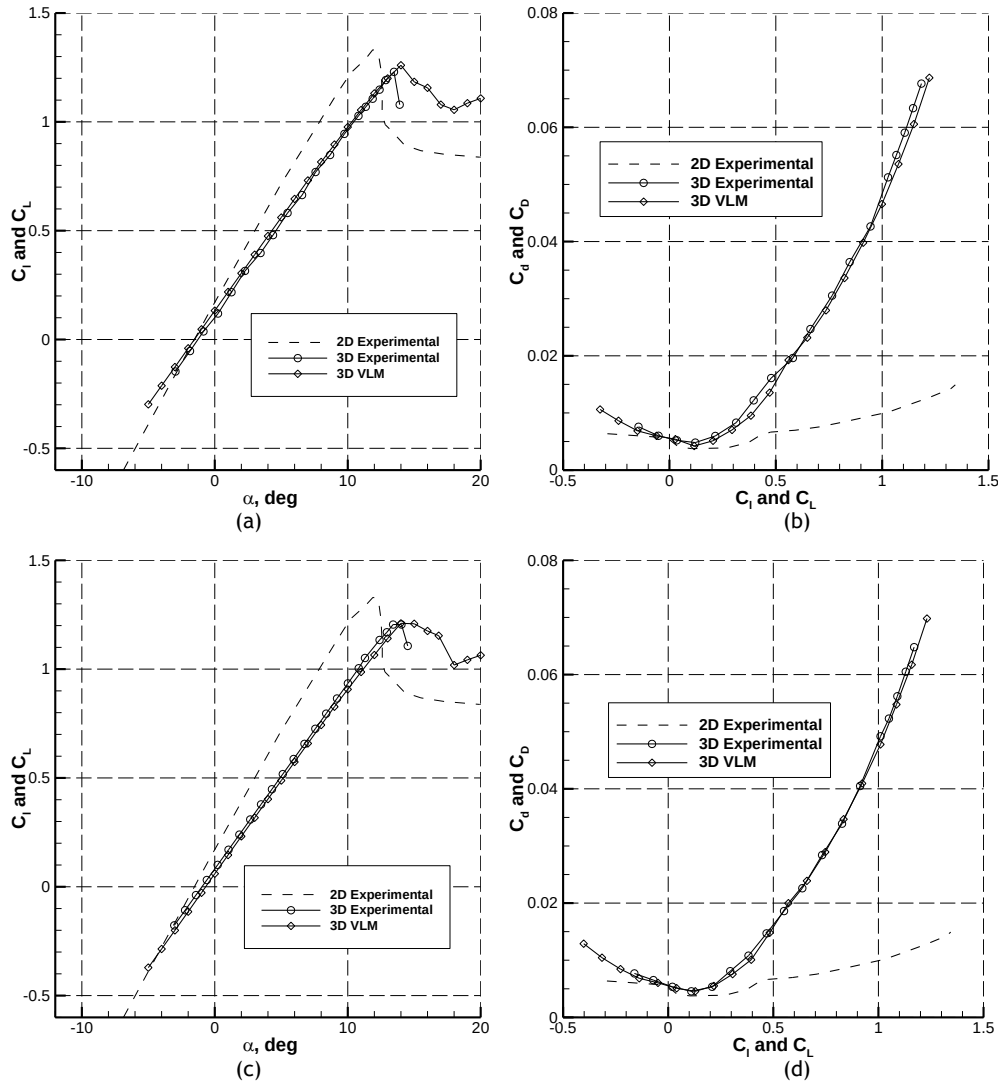

Figure 3 - $C_L - \alpha$ and $C_D - C_L$ curves predicted using 3D VLM: a) $C_L - \alpha$ and b) $C_D - C_L$ curves for a wing without washout and c) $C_L - \alpha$ and d) $C_D - C_L$ curves for a wing with 2° washout.

Figure 3d shows the equivalent curves as in Fig. 3b, but for the wing with 2° washout. Observing the calculated and experimental $C_D - C_L$, it is possible to verify a good compliance. In fact, these curves almost coincide with each other, being the predictions of C_{D0} and $C_{D,min}$ very close to the experimental results.

The validation procedure carried out showed that the aerodynamic tool is capable of predicting both linear and non-linear wing characteristics, with high accuracy. This an important step in order to achieve an aero-structural solver that is capable of analyzing wings effectively.

III. Structural Solver

General Formulation

The implementation described is mainly based on the work of Kapania and Liu [4].

There are two main assumptions to this formulation: a straight line normal to the non-deformed mid-surface remains straight after deformation, and the transverse normal stress may be neglected in the constitutive equations.

The strain energy of the wing structure is:

$$U = \frac{1}{2}\int\int\int_V \{\sigma\}^T\{\varepsilon\}dV = \frac{1}{2}\int\int\int_V \{\varepsilon\}^T[D]\{\varepsilon\}dV \tag{9}$$

where the constitutive relations for the material (Hooke's Law, establishing the relation between the stress state $\{\sigma\}$ and the strains $\{\varepsilon\}$) were applied in the form of the tensor $[D]$ (taken as symmetrical).

The kinetic energy of the equivalent plate is defined in integral form as:

$$T = \frac{1}{2}\int\int\int_V \rho\mathbf{v}.\mathbf{v}dV \tag{10}$$

$\mathbf{v}$ being the velocity vector.

More details on the displacement field and the strains can be found in references [4,9].

In order to perform the calculations, the general wing geometry needs to be transformed into the square domain defined by ξ, η:

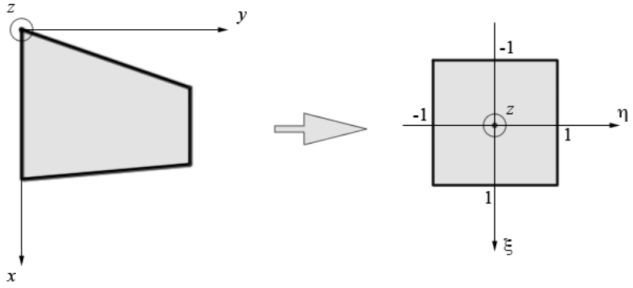

Figure 4 – Domain transformation used in Kapania and Liu formulation [4].

The application of such transformation, and subsequent discretization of Eq. (9) and Eq. (10), leads to a complex and long derivation which goes beyond the scope of the current paper. References [4,9] provide a detailed insight of the derivation. In order to evaluate the integrals in the aforementioned equations, Gaussian quadrature is used. The integrands and limits of integration are defined by the wing geometry and the properties of its structural elements.

Validation

In order to assess the accuracy of the current implementation of the equivalent plate method and also its performance, a set of tests were carried out for a general trapezoidal wing composed of skins, spars, and ribs. The results obtained with the present method were compared against a commercial finite element model.

The geometric and material parameters of the trapezoidal plate are given in Table 1.

Notice that the plate is clamped at the root.

There are 4 spars and 11 ribs distributed uniformly along the wing chord. All the wing components (spars, ribs and skin) are made of aluminum. In particular the wing components dimensions are the following: skin thickness t_0 = 3mm, spar cap height h_1 = 5mm, spar cap width l_1 = 9.47mm, spar web thickness t_1 = 1.47mm. Notice that the ribs have the same cap dimensions and web thickness as the spars. The root and tip airfoils thickness-chord ratio is varied from 0.15 to 0.06, respectively. Notice that both root and tip airfoils were obtained through a Karman-Treftz conformal transformation [10].

A general CAD model of the trapezoidal wing used in the equivalent plate validation tests is seen in Fig. 5.

Table 1 - Geometric and material properties of the test wing.

Geometric properties		Material Properties (Aluminum)	
Semi-span, $b/2$	4.88 m	mass density, ρ	2.7 × 10^3 kg/m^3
LE Sweep, Λ_{LE}	30°	Young's modulus, E	70.7 GPa
Tip twist	0°	Poisson's ratio, ν	0.3
Dihedral, ϕ	0°		
Root chord, c_r	1.83 m		
Tip chord, c_t	0.91 m		

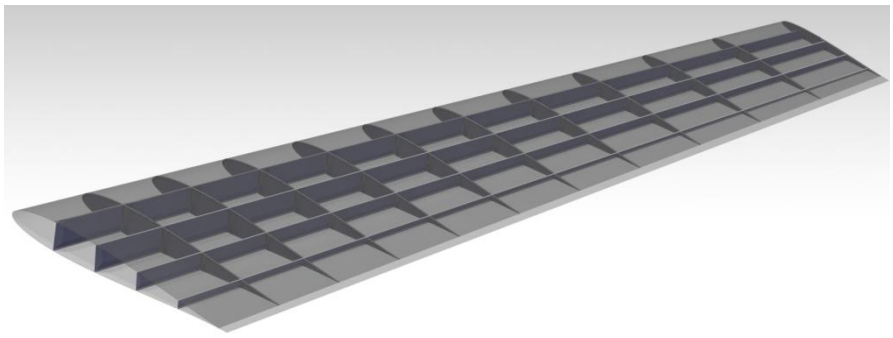

Figure 5 – CAD model of the trapezoidal wing used in the equivalent plate validation tests. Note that the skins are transparent, revealing the spars and ribs inside the wing.

A. Modal Analysis

The modal analysis is carried out using the present equivalent plate model. These results are then compared to the corresponding finite element model.

Table 2 compares the modal frequencies between the equivalent plate method and the finite element model from reference [9]. Observing the results, one can conclude that the present equivalent plate model is capable of approximating the modal frequencies very closely. Nevertheless, in order to improve the numerical results, a high number of integration points is necessary. Despite of this, the 5^{th} modal frequency shows a relatively high error, being overestimated by about 8.4 %.

In order to perform the analysis under static loads, a pair of loads, equal in magnitude (4448 N) and opposite in direction is applied at the wing tip (at the locations of the first and last spars).

Table 2 - Comparison of natural vibration frequencies computed with EPM and FEM.

Mode	Eq. Plate [rad.s^{-1}]	FEM [rad.s^{-1}]	$\lvert e_r \rvert$ [%]
1st	46.451	46.639	0.403
2nd	203.408	200.068	1.669
3rd	280.541	284.249	1.304
4th	371.215	358.933	3.422
5th	496.568	458.022	8.416
6th	744.267	726.96	2.381

B. Static Load Analysis

The deformation along the leading edge and the wing tip is considered and compared with the corresponding finite element model from reference [9]. Figure 6a shows the displacement results along the wing leading edge and Fig. 6b the deformation at the wing tip.

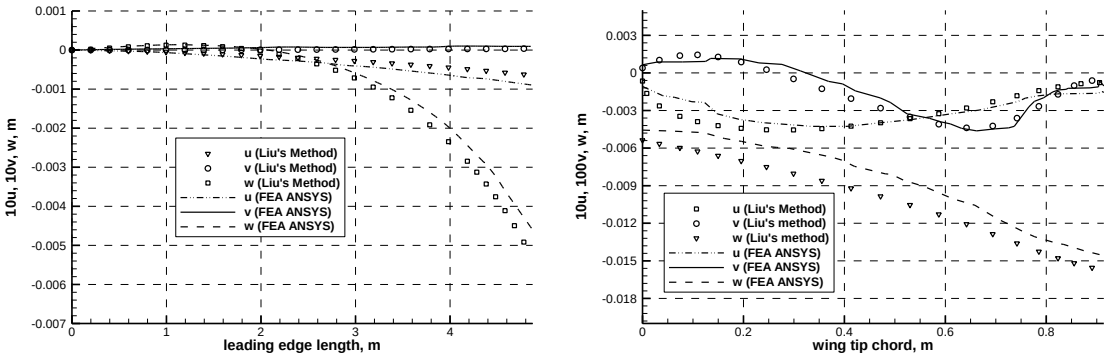

(a) (b)

Figure 6 – Displacement of the test wing, due to a torque application: a) wing leading edge deflection and b) wing tip deflection.

Comparatively to the leading edge displacement, EPM gives an overestimated w deformation and an underestimated u deformation but nonetheless a very close approximation for both deformations. The v deformation nearly coincides with the finite element calculation results, being approximated with the highest accuracy among the three displacements.

Along the wing tip, Liu's method captures the shape of the displacement field very accurately. On one hand, u and v deformations are approximated very precisely, almost coinciding with the finite element model. On the other hand, w deflection is slightly overestimated.

Based on the current validation, it becomes apparent that the equivalent plate method approach shows good results for complex structures, given its simplicity and low computational cost.

IV. Aero-structural Solver

After describing the aerodynamic and structural disciplines, the aero-structural solver could be formulated and implemented.

One of the essential aspects in the aero-structural formulation is the transfer of the coupling variables between the aerodynamic and structural analysis [11]. There are mainly two aspects involved that need to be addressed during the information transfer. The first one is the level of fidelity in the coupling of the aerodynamic and structural model, which has to guarantee that the accuracy of the individual analysis is not compromised. The second concern is that the discretization in each model must preserve geometric consistency during the analysis process.

The aerodynamic and structural solvers coupling in the context of the aero-structural analysis is shown in Fig. 7.

The aerodynamic point loads vector computed with the VLM tool are transferred to the structural tool along with the coordinates of the application point. Since in the structural tool there is not an associated mesh, the loads are applied without any pre-processing.

Transferring the displacements given from the structural analysis to the aerodynamic module is achieved by generating the deflected aerodynamic mesh. This procedure is straightforward to implement, since the equivalent plate model deflections are computed using Legendre Polynomials, which could be evaluated at any point inside the wing planform.

In the current implementation, the deflections are computed at each point of the aerodynamic mesh, and summed to the undeformed mesh.

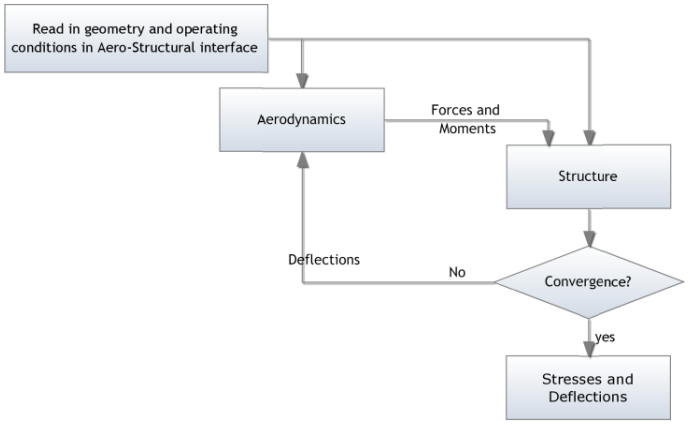

Figure 7 – Aerodynamic and structural solvers coupling methodology.

The first time the aerodynamic solver is called, the displacement field of the structure is equal to zero. After the aerodynamic solver completes, aerodynamic forces are transferred and the structural solver is called. The new displacement field is then translated to a movement of the aerodynamic mesh and the aerodynamic solver is called again. This process continues until the state of aerodynamic and structure converged as determined by the norm of the structural displacement residuals. In the current work, the total number of iterations is typically between 5 to 10 iterations.

Analysis Example

In order to evaluate the results computed with the current implementation of the aero-structural methodology and also its performance, an analysis test is carried out for a rectangular wing composed of skins, spars, and ribs.

The geometric and material parameters of the rectangular wing are given in Table 3. Note that the wing is assumed to be clamped at the root.

Table 3 - Geometric and material properties of the rectangular wing used in aero-structural analysis.

Geometric properties		Skin and Spar Material (Aluminum 6061-T6) [12]		Ribs material (Airex C70.75) [13]	
Semispan, $b/2$	0.6 m	density, ρ	2.7×10^3 kg/m^3	density, ρ	80 kg/m^3
Tip twist	0°	Young's modulus, E	68.9 GPa	Young's modulus, E	66 MPa
Dihedral, ϕ	0°	Shear Modulus, G	26 GPa	Shear Modulus, G	30 MPa
chord, c	0.15 m	Poisson's ratio, ν	0.33	Poisson's ratio, ν	0.1

The wing considered has 2 spars, located at 30 % and 50 % of the chord, and 5 ribs distributed uniformly along the wing span. Both skin and spars are made of aluminum. In particular, these components have the following dimensions: skin thickness t_0 = 0.4 mm, spar cap height h_1 = 0.4 mm, spar cap width l_1 = 5 mm, spar web thickness t_1 = 0.4 mm. The ribs are made of PVC foam Airex® C70.75 with 6.2 mm of thickness.

The airfoil chosen for the wing is a modified version of the SG6042. More details about the airfoil are found in reference [14].

A general CAD model of the rectangular wing used in the aero-structural analysis test is seen in Fig. 6.

The presented wing is analyzed at an angle of attack of $7.5°$ and a velocity of $30\,m/s$. For the present calculation sea level conditions were considered. The EPM is used with a 12th Legendre polynomial.

Figures 7a, 7b and 7c show the distribution of wing deflections u, v and w. As expected, the w deflection has the higher magnitude, when compared with u and v. It is possible to see an increasing vertical deformation as the distance from the wing root

increases. This was expected since the wing is considered to be clamped at the root.

In Fig. 7d the distribution of u, v and w along the wing tip are shown. One can observe that wing tip u and w displacements are almost constant and that v deflection has a maximum near the wing leading edge.

The aero-structural analysis performed took about 43 seconds to complete on an Intel® Core i7 740QM CPU, requiring a total of 5 iterations until convergence was achieved.

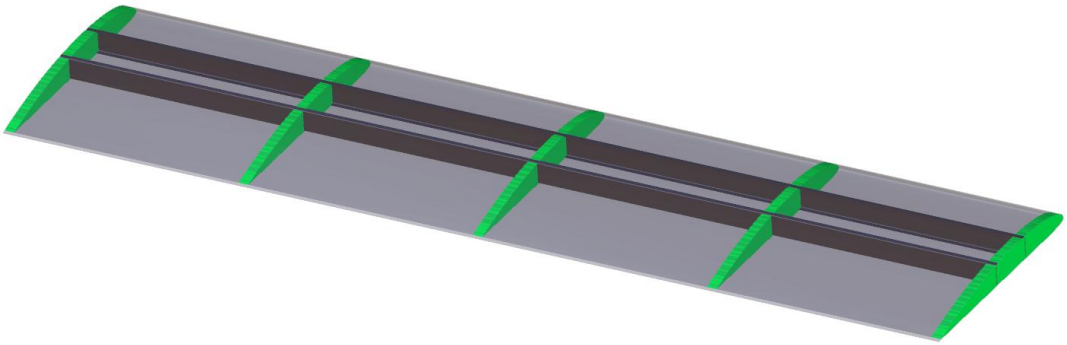

Figure 6 – CAD model of the aero-structural test wing. Note that the skins are transparent, revealing the spars and ribs inside the wing.

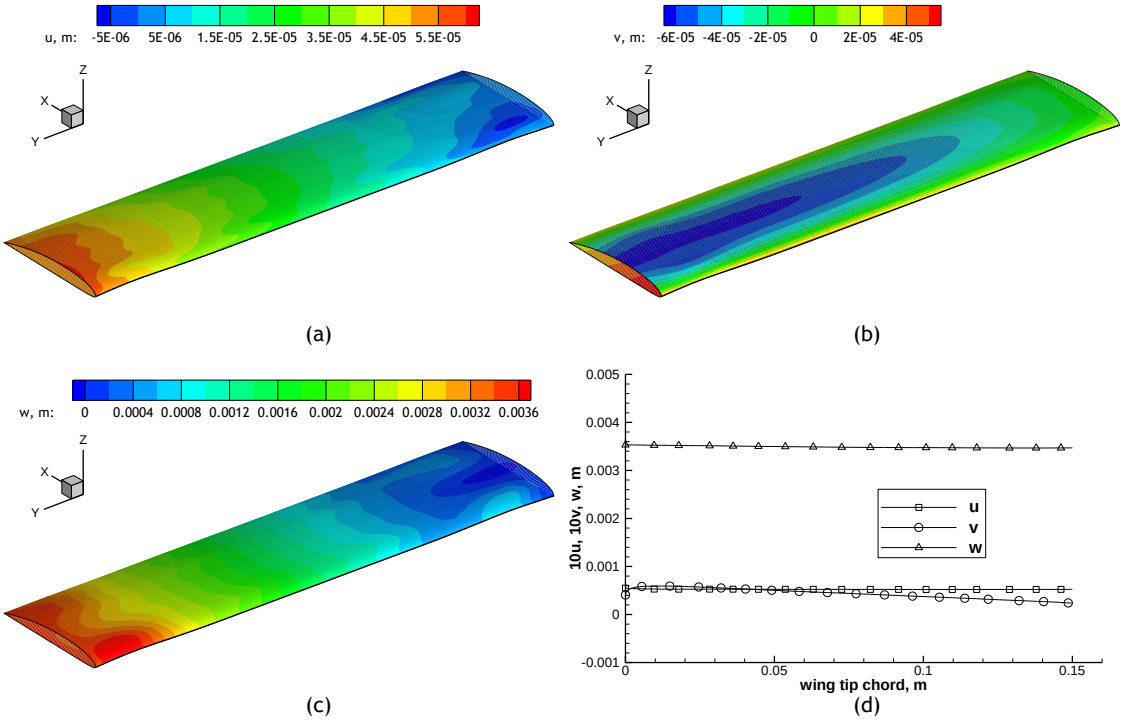

Figure 7 – Displacements of the test wing, due to aerodynamic loading at $\alpha = 7.5°$, $V = 30\ m/s$ at sea level: a) u, b) v, c) w deflection distribution along the wing and d) wing tip deflections.

V. Concluding Remarks

A tool for aero-structural analysis of wings was developed and implemented. This tool was successfully applied to the aero-structural analysis of a rectangular wing composed of skins, spars and ribs.

The two disciplines that constitute the aero-structural model were implemented and validated. In the present study, the aerodynamic model chosen was a non-linear VLM. It was concluded that it does not require large computing resources and significant time to predict the non-linear aerodynamic characteristics of three-dimensional wings. In fact, the present

method uses known non-linear aerodynamic data of airfoil. This aerodynamic discipline was validated against experimental data in the linear and non-linear regime. The present results agree well with experiments, both in lift and drag coefficients.

The structural method chosen was an equivalent plate model (EPM), which arises as a compromise to simulate complex structures for the purpose of obtaining solutions in the early design stages. The implemented EPM was validated against numerical data from finite element analysis. The comparison shows good agreement with FEM data, in both static load analysis and modal analysis.

In the last section, the aero-structural solver methodology was formulated. The coupling between the aerodynamic and structural disciplines was presented and described, highlighting the important aspects. A rectangular wing was analyzed with the proposed aero-structural tool, effectively showing its capabilities. The tool exhibited a rapid convergence and low computational needs.

Despite the strong points exposed by the aero-structural analysis tool and its disciplines, some future work is still necessary in order to assess the accuracy of the current implementation, mainly the validation through experimental data. In order to achieve this, in the next few months, wing tunnel tests will be made. The experimental data collected from the tunnel test experiment will then be compared against the numerical data computed using the current implementation.

References

[1] J.R.R.A. Martins, "A Coupled-Adjoint Method for High-Fidelity Aero-Structural Optimization," Master's thesis, Stanford University, October 2002.

[2] R. Mukherjee and A. Gopalarathnam, "An Iterative Decambering Approach for Post-Stall Prediction of Wing Characteristics using known Section Data," 41st AIAA Aerospace Sciences Meeting, Reno, Nevada, January 2003.

[3] R. Mukherjee, "Post-Stall Prediction of Multiple-Lifting-Surface Configurations using a Decambering Approach," Master's thesis, North Carolina State University, Raleigh, NC, December 2004.

[4] R.K. Kapania and Y. Liu, "Static and Vibration Analyses of General Wing Structures using Equivalent-Plate Models," AIAA Journal, vol. 38, pp. 1269–1277, July 2000.

[5] J. Katz and A. Plotkin, Low-Speed Aerodynamics. Cambridge University Press. 2nd ed., 2001.

[6] W.H. Press, S.A. Teukolsky, W.T. Vetterling and B.P. Flannery, Numerical Recipes in Fortran — The Art of Scientific Computing, 2nd ed., Cambridge University Press, New York, 1992.

[7] I.H. Abbott, A.E. Yondoenhoff, and J. Louis S. Stiyers, "Summary of Airfoil Data," tech. rep., Langley Memorial Aeronautical Laboratory, 1945.

[8] J.C. Sivells, "Experimental and Calculated Characteristics of Three Wings of NACA 64-210 and 65-210 Airfoil Sections with and without 2° Washout," tech. rep., Langley Memorial Aeronautical Laboratory, December 1947.

[9] R. Gabriel, "Development of Equivalent Plate Models for Aircraft Wing Structures," Master's thesis, Universidade Técnica de Lisboa, October 2007.

[10] K. Karamcheti, Principles of Ideal Fluid Aerodynamics, Krieger, Malabar, FL, 1980, pp. 488–490.

[11] P.W. Jansen, "Aero-structural Optimization of Non-Planar Lifting Surfaces," Master's thesis, University of Toronto, 2009.

[12] "Metals Handbook, Vol.2 - Properties and Selection: Nonferrous Alloys and Special-Purpose Materials", ASM International 10th Ed. 1990.

[13] "AIREX® C70 Universal Structural Foam" Datasheet.

[14] J. Mestrinho, P. Gamboa and P. Santos, "Design Optimization of a Variable-Span Morphing Wing for a Small UAV", 52nd AIAA/ASME/ASCE/AHS/ASC Structures, Structural Dynamics and Materials Conference, 4-7 April 2011, Denver, Colorado.